
This item was submitted to [Loughborough's Research Repository](#) by the author.
Items in Figshare are protected by copyright, with all rights reserved, unless otherwise indicated.

Oscillations and waves in single- and multi-cellular systems with free calcium

PLEASE CITE THE PUBLISHED VERSION

PUBLISHER

© Yulia Timofeeva

PUBLISHER STATEMENT

This work is made available according to the conditions of the Creative Commons Attribution-NonCommercial-NoDerivatives 4.0 International (CC BY-NC-ND 4.0) licence. Full details of this licence are available at:
<https://creativecommons.org/licenses/by-nc-nd/4.0/>

LICENCE

CC BY-NC-ND 4.0

REPOSITORY RECORD

Timofeeva, Yulia. 2019. "Oscillations and Waves in Single- and Multi-cellular Systems with Free Calcium".
figshare. <https://hdl.handle.net/2134/33829>.

University Library



Author/Filing Title ... TIMOFEEVA

Class Mark T

Please note that fines are charged on ALL
overdue items.

| | | |
|--|--|--|
| | | |
|--|--|--|

0402940067



OSCILLATIONS AND WAVES IN SINGLE AND MULTI-CELLULAR SYSTEMS WITH FREE CALCIUM



Yulia Timofeeva

Ph.D. in Mathematics

Mathematical Biology Group

Department of Mathematical Sciences

Loughborough University - 2003

Oscillations and Waves in Single and Multi-cellular Systems with Free Calcium

by

Yulia Timofeeva


A Doctoral Thesis

Submitted in partial fulfillment of the requirements
for the award of

Ph D in Mathematics of Loughborough University

October 2003

©by Yulia Timofeeva 2003

| | |
|--|------------|
|  Loughborough University Physical Library | |
| Date | Sept 04 |
| Class | |
| Acc No. | 040298 006 |

Keywords:

Calcium

Puffs/sparks

Fire-Diffuse-Fire model

Noise

Stochastic propagation

Intracellular and intercellular waves

Non-equilibrium phase-transition

Abbreviations:

ATP - ribonucleoside 5'-triphosphate

CICR - Ca^{2+} -induced Ca^{2+} release

DAD - delayed after-depolarising

DP - directed percolation

DYK - De Young Keizer

ER - endoplasmic reticulum

FDF - Fire-Diffuse-Fire

HB - Hopf bifurcation

HC - homoclinic bifurcation

IP_3 - inositol 1,4,5-trisphosphate

IP_3R - IP_3 receptor

JMK - Jung-Mayer Kress

LP - limit point

PLC - phospholipase C

PD - period doubling

RyR - ryanodine receptor

SERCA - sarco- and endoplasmic reticulum calcium ATPase

SR - sarcoplasmic reticulum

VOCC - voltage-operated calcium channel

Abstract

Calcium ions are an important second messenger in living cells. Indeed calcium signals in the form of waves have been the subject of much recent experimental interest. A fundamental approach for studying cellular signalling is the combination of state of the art experimental techniques, in particular high resolution fluorescence imaging, with spatio-temporal mathematical models of intracellular calcium regulation. Experimental findings can be incorporated into mathematical models and, vice versa, model predictions can be directly tested in experiments. This approach provides a powerful tool to clarify the very complex mechanisms involved in cellular Ca^{2+} signalling.

The aim of this thesis is to provide insight into oscillations and waves of cytosolic Ca^{2+} in both single and multi-cellular systems from a mathematical perspective. We focus on two models of Ca^{2+} release for a systematic mathematical and numerical analysis of Ca^{2+} dynamics. One of them is a biophysically detailed model which we study using tools from bifurcation theory, numerical continuation and numerical simulation. The other is a much simpler minimal model of Ca^{2+} dynamics that emphasises the fundamental space and time scales of cellular Ca^{2+} dynamics and allows for exact mathematical analysis. For the detailed biophysical model we calculate the speed and stability of travelling waves as a function of physiologically significant parameters. The minimal model of Ca^{2+} dynamics is obtained via a systematic reduction of the biophysical model and its analytically obtained behaviour is shown to be in excellent agreement with the original biophysical model. This minimal model is then used to gain insight into the effects of spatial heterogeneity and biologically realistic sources of noise on intra- and inter-cellular cell signalling. In particular we pursue issues of wave propagation, wave propagation failure and the role of noise in generating coherent whole cell rhythms.

Acknowledgements

I would like to express my gratitude to the following people for their support and assistance during my work on this thesis

Steve Coombes, who provided me with excellent and enthusiastic supervision together with continuing motivation and encouragement. I could not have imagined having a better advisor and mentor for my PhD. Thank you for all of the inspiration and the guidance you gave me during this work.

Martin Bootman of the Babraham Institute, for the useful discussions on the experimental aspects.

The Mathematical Biology Group of Loughborough University, for their help and advice.

All the rest of the academic and support staff of the Mathematical Sciences Department at Loughborough University for their kind assistance in many different ways.

All my friends, wherever they are, for their continued moral support.

Loughborough University, in particular the Mathematical Sciences Department, for financial support.

My parents and sister Irina, for their understanding, endless patience and encouragement when it was most required.

Contents

| | | |
|----------|--|-----------|
| 1 | Introduction | 1 |
| 1 1 | Experimental observations on Ca^{2+} oscillations | 3 |
| 1 2 | Spatial Ca^{2+} propagation | 4 |
| 1 3 | Overview of the thesis | 8 |
| 2 | Models of calcium oscillations | 13 |
| 2 1 | Calcium dynamics | 15 |
| 2 2 | Theoretical models of Ca^{2+} oscillations | 19 |
| 3 | The De Young Keizer model | 36 |
| 3 1 | Reduction of the De Young Keizer model of Ca^{2+} release | 37 |
| 3 2 | Travelling waves in the model | 42 |

| | | |
|----------|--|------------|
| 3 2 1 | Bifurcation analysis | 46 |
| 3 2 2 | Stability | 54 |
| 3 2 3 | A kinematic theory of spike trains | 55 |
| 3 2 4 | Period doubling bifurcations | 59 |
| 4 | The continuum Fire-Diffuse-Fire model | 65 |
| 4 1 | The Fire-Diffuse-Fire model | 66 |
| 4 2 | Solitary travelling pulse | 69 |
| 4 3 | Periodic travelling wave | 71 |
| 5 | Discrete Fire-Diffuse-Fire model | 78 |
| 5 1 | Spatially discrete FDF model | 80 |
| 5 1.1 | Periodic travelling wave | 81 |
| 5.1 2 | Solitary travelling pulse | 87 |
| 5 2 | Discrete-time FDF model | 88 |
| 5 2.1 | One-dimensional model | 88 |
| 5 2 2 | Two-dimensional model | 96 |
| 6 | Stochastic FDF model | 107 |
| 6 1 | One-dimensional stochastic model | 109 |

| | | |
|----------|--|------------|
| 6 1 1 | Directed percolation | 112 |
| 6 2 | Two-dimensional stochastic model | 119 |
| 7 | Intercellular calcium waves | 127 |
| 7 1 | Mechanisms of intercellular calcium wave propagation | 128 |
| 7 2 | Intercellular Ca^{2+} waves in the Fire-Diffuse-Fire model | 130 |
| 7 2.1 | Model equations | 131 |
| 7 2.2 | Analysis of the model | 132 |
| 7 3 | Intercellular Ca^{2+} waves in the presence of mobile IP_3 | 140 |
| 7 3.1 | Intercellular Ca^{2+} waves using the DYK single cell model | 142 |
| 7 3.2 | Intercellular Ca^{2+} waves using the FDF single cell model | 145 |
| 8 | Conclusions and further work | 150 |
| 8 1 | Conclusions | 150 |
| 8 2 | Further work | 152 |
| A | Numerical Issues | 156 |
| A 1 | XPPAUT | 156 |
| A 2 | MATLAB | 163 |
| A 3 | Fourier spectral methods | 163 |

| | |
|--|-----|
| A 4 Intercellular waves in the FDF model | 164 |
|--|-----|

Chapter 1

Introduction

Many processes in living systems are oscillatory. Biological rhythms occur at all levels of biological organisation, from unicellular to multi-cellular organisms, with periods ranging from fractions of a second to years. Besides quite obvious examples of biological oscillations such as the beating of the heart, lung respiration, the sleep-wake cycle, central pattern generation and locomotion in animals, there are many instances of biological oscillations at the cellular level. These rhythms find their roots in the many regulatory mechanisms that control the dynamics of living cells. For example, neural and cardiac rhythms at the single cell level are associated with the regulation of voltage-dependent ion channels, metabolic oscillations originating from the regulation of enzyme activity, pulsatile intercellular signals and intracellular calcium oscillations associated with receptor activity, while regulation of gene expression in hypothalamic neurons underlies circadian rhythms. Although different cell types express markedly different rhythms a common set of components assembled in a cell-specific manner can give rise to different spatial and temporal dynamics. Thus, the spatially extended nature of the cell and the way in which these components are organised into interacting complexes is vitally important for generating physiologically significant cellular rhythms. In view of the large number of variables involved, the spatially extended

nature of the cell, and the complexity of nonlinear feedback processes, mathematical models are vital for a better understanding of how molecular and cellular mechanisms give rise to oscillations. Importantly a mathematical approach opens up the way to explore the role of space, heterogeneity and noise in shaping cellular rhythms. Models are also useful to understand the transition from simple to complex oscillatory behaviour and for delineating the conditions under which they arise. The strength of a theoretical approach is that it clarifies the molecular and dynamical mechanisms for cellular rhythm generation.

One of the most significant findings in the field of intracellular signalling within the last two decades is the discovery of Ca^{2+} oscillations. This has radically affected the way biochemical oscillations are viewed. Ca^{2+} oscillations are of interest for a variety of reasons. First, they occur in a large number of cell types, either spontaneously or as a result of stimulation by an external signal such as a hormone or a neurotransmitter. Second, it is now clear that, besides the rhythms encountered in electrically excitable cells, they represent the most widespread oscillatory phenomenon at the cellular level. Third, Ca^{2+} oscillations are often associated with the propagation of Ca^{2+} waves within the cytosol, and sometimes between adjacent cells. This phenomenon has become one of the most important examples of spatio-temporal organisation at the cellular level. Ca^{2+} is a highly versatile intra- and inter-cellular signal that operates over a wide temporal range that is now known to regulate many different cellular processes, from cell division and differentiation to cell death [11]. Many of the Ca^{2+} -signalling components are organised into macromolecular complexes in which Ca^{2+} -signalling functions are carried out within highly localised environments. These complexes can operate as autonomous units that can be multiplied or mixed and matched to create larger, more diverse signalling systems, as illustrated by cardiac Ca^{2+} signalling. Rapid highly localised Ca^{2+} spikes regulate fast responses, whereas repetitive global transients or intracellular Ca^{2+} waves control slower responses. Cells respond to such oscillations using sophisticated mechanisms including an ability to

interpret changes in frequency. Such frequency-modulated signalling can regulate specific responses such as exocytosis and differential gene transcription

In this thesis we shall explore oscillations and waves of cytosolic Ca^{2+} in both single and multi-cellular systems from a mathematical perspective. More precisely, we focus on two models of Ca^{2+} release for a systematic mathematical and numerical analysis of Ca^{2+} dynamics. One of them is a biophysically detailed model which we study using tools from bifurcation theory, numerical continuation and numerical simulation. The other is a much simpler minimal model of Ca^{2+} dynamics that emphasises the fundamental space and time scales of cellular Ca^{2+} dynamics and allows for exact mathematical analysis. For the detailed biophysical model we calculate the speed and stability of travelling waves as a function of physiologically significant parameters. The minimal model of Ca^{2+} dynamics is obtained via a systematic reduction of the biophysical model and its analytically obtained behaviour is shown to be in excellent agreement with the original biophysical model. This minimal model is then used to gain insight into the effects of spatial heterogeneity and biologically realistic sources of noise on intra- and inter-cellular cell signalling. In particular we pursue issues of wave propagation, wave propagation failure and the role of noise in generating coherent whole cell rhythms.

1.1 Experimental observations on Ca^{2+} oscillations

It has been known for a long time that calcium oscillations operate in periodically contracting muscle cells (*e.g.* heart cells) and neurons [115]. However, they were only first discovered in non-excitable cells in the mid-1980s, notably in oocytes upon fertilisation by Cuthbertson and Cobbold [40] and in hepatocytes subject to hormone stimulation by Woods *et al* [172, 173]. These direct observations of Ca^{2+} oscillations followed earlier theoretical predictions [89, 129] and indirect measurements [130]. Later, Ca^{2+} oscillations were also found in many other animal cells [10, 16, 62, 82,

142, 157] as well as in plant cells [111]. The progress of the experimental results on Ca^{2+} oscillations and the associated propagation of intracellular Ca^{2+} waves arising in recent years has been examined in a series of reviews [7, 8, 12, 14, 33, 39, 55, 76, 112, 128, 131, 167, 168]. We briefly recall the main properties of Ca^{2+} oscillations as determined from a large number of experimental studies. Cytosolic Ca^{2+} oscillations arise either spontaneously [72, 106] or in response to stimulation by extracellular signals, with period ranging from nearly one second to tens of minutes, depending on the cell type. Among the most studied cells, with regard to Ca^{2+} oscillations, are cardiac cells, oocytes, hepatocytes, endothelial cells, fibroblasts, pancreatic acinar cells and pituitary cells. The shape of the oscillations is highly variable (see Figure 1.1). In some cases the oscillations are quasi-sinusoidal, while in others they take the form of abrupt spikes, which are often preceded by a gradual increase reminiscent of the pacemaker depolarising potential seen in oscillatory neurons or cardiac cells [45]. It has been repeatedly observed that oscillations occur only in a certain range of stimulation and that the frequency of Ca^{2+} spikes increases with the intensity of the stimulus. Besides the induction of oscillations by external signals, it is often possible to elicit a train of Ca^{2+} spikes by increasing the level of extracellular or intracellular Ca^{2+} , or the level of inositol 1,4,5-trisphosphate (IP_3) [121]. The latter messenger is synthesised in response to external signals and is known to raise the level of cytosolic Ca^{2+} through mobilisation from intracellular stores [9, 15].

1.2 Spatial Ca^{2+} propagation

The spatial propagation of Ca^{2+} waves mediated by diffusive transport of calcium ions has long been observed in a variety of egg types after fertilisation [24, 60, 77, 78, 79]. In these cells, waves of Ca^{2+} propagate over the cortex, from the site of fertilisation. The wave-like propagation of Ca^{2+} signals has now also been observed in other cells in which Ca^{2+} oscillations were previously characterised (see for example [1, 13] for some

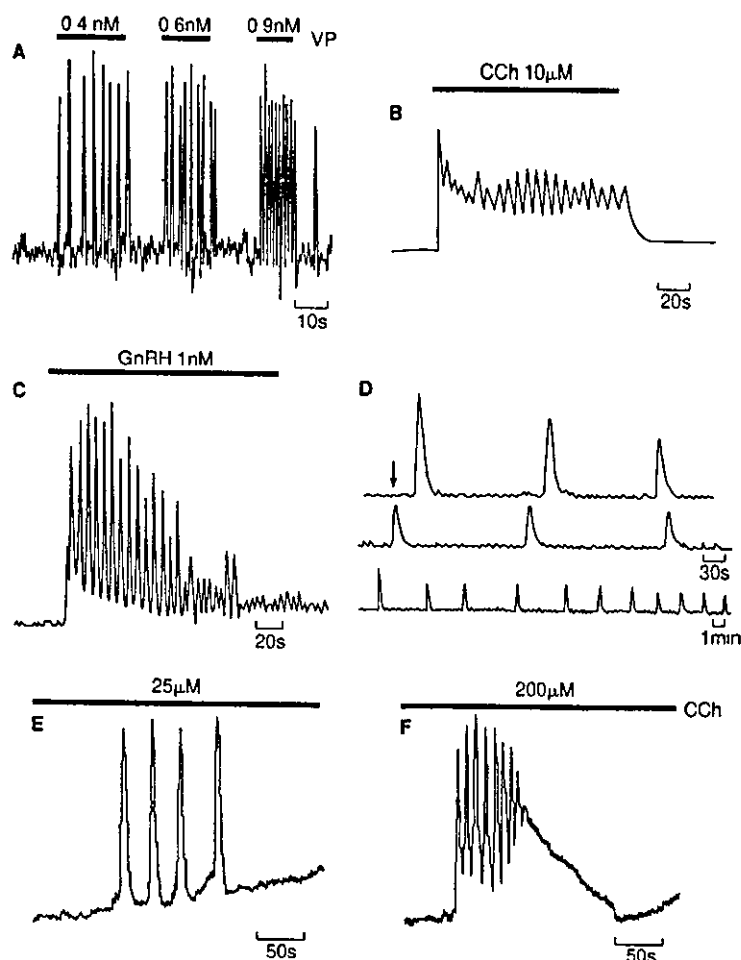


Figure 1.1 Typical calcium oscillations from a variety of cell types. A Hepatocytes stimulated with vasopressin (VP) B Rat parotid gland stimulated with carbachol (CCh) C Gonadotropes stimulated with gonadotropin-releasing hormone (GnRH) D Hamster eggs after fertilisation. The time of fertilisation is denoted by the arrow. E and F Insulinoma cells stimulated with two different concentrations of carbachol (From [14])

reviews). Thus, Ca^{2+} oscillations and waves appear to be closely related phenomena [15]. The velocity of Ca^{2+} waves varies in different cells; the wave propagates at a rate of the order of $10 \mu\text{m/s}$ on the surface of oocytes [77, 79], $30 \mu\text{m/s}$ in hepatocytes [162], and at a rate close to $100 \mu\text{m/s}$ in the cytoplasm of cardiac cells [160]. The most complex wave patterns, exhibiting hot spots, spherical, spiral and planar waves were demonstrated in *Xenopus* oocytes [94]. As an example, the image of a Ca^{2+} spiral wave is given in Figure 1.2. A single mammalian cell of size $10\text{-}20 \mu\text{m}$ is

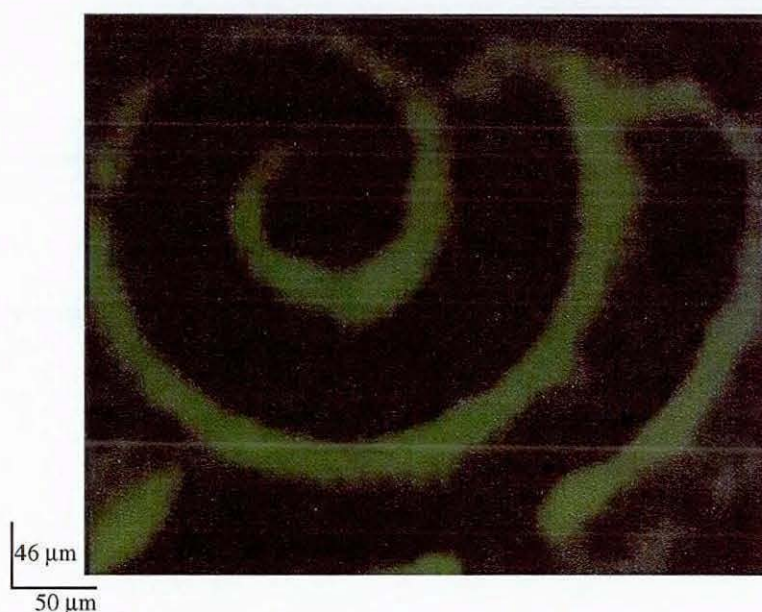


Figure 1.2: *Confocal image of regenerative spiral waves of free Ca^{2+} observed in *Xenopus laevis* oocytes (From [94]).*

not large enough for such complex patterns, although similar patterns have been observed in larger cardiac cells and in networks of astrocytes and glia [98]. Also other experiments indicate that in some cell types (for example epithelia [141] and glia [26, 27]) Ca^{2+} triggered by mechanical stimulation may propagate from cell to cell. This intercellular propagation appears to be mediated by the passage of Ca^{2+} or IP_3 through gap junctions [19], although extracellular messengers such as ATP may be involved.

Moreover, high-resolution imaging of Ca^{2+} in a variety of cell types shows that travelling waves can vary in their appearance. For example, the calcium wave that occurs during fertilisation in mature *Xenopus* eggs appears to be continuous [57, 120], whereas the calcium wave in immature *Xenopus* oocytes propagates as a sequence of bursts [25, 122, 124, 174]. It is commonly believed that information is encoded in the time course of the Ca^{2+} signal. Thus, the distinction between these two modes of propagation is likely to be of physiological significance. Another interesting aspect of intracellular Ca^{2+} regulation is the generation of global events build up from elemental local events called *puffs*. These elementary events in many electrically non-excitable cells have amplitudes typically ranging from $\sim 50 - 600$ nM, a spatial spread of ~ 6 μm and a total duration of ~ 1 second. Apart from *Xenopus* oocytes, such events have subsequently been observed in HeLa cells, neurites and endothelial cells (reviewed in [22]). In heart and skeletal muscle, where Ca^{2+} release channels are spatially organised in clusters, localised Ca^{2+} release events have also been seen [31]. These events called *sparks* are analogous to the Ca^{2+} puffs, although they are usually faster in onset and decline, and have a more restricted spread ($\sim 1 - 3$ μm). Ca^{2+} sparks and puffs are simple examples of the stochastic nature of intracellular Ca^{2+} dynamics. The timescale on which stochasticity is observed when puffs/sparks are triggered is of the order of many seconds. However, the origin of the stochastic nature of Ca^{2+} release events lies in the individual gating of Ca^{2+} channels, which occur on the millisecond timescale.

As regards the physiological significance of Ca^{2+} oscillations and waves, it is conceivable that the rapid spatial propagation of Ca^{2+} signals provides a useful communication mechanism between distinct parts of the cell or between different adjacent cells in a tissue (see [27, 141]). Calcium signals regulate a large number of cellular processes including contraction of muscle fibers, release of hormones and neurotransmitters, synaptic plasticity, sensory perception and adaptation in photoreceptors, exocytosis, gene expression, gap junction regulation and others.

1.3 Overview of the thesis

In **Chapter 2**, we define the main components of the cell and describe important aspects of Ca^{2+} dynamics involved in the regulatory mechanisms of Ca^{2+} signalling in living cells. We then discuss the basic approaches used in the modelling of Ca^{2+} oscillations, including the continuous deterministic models of Ca^{2+} oscillations based on a description of essential Ca^{2+} fluxes throughout the cell. Bifurcation analysis of various biophysical models demonstrates that oscillations are typically associated with an instability of a fixed point in favour of a stable limit cycle over a range of parameter values. Moreover, the bifurcation structure for many of the commonly used biophysical models of Ca^{2+} oscillations can be surprisingly rich. Three of the basic models of Ca^{2+} oscillations in the presence of IP_3 (two-pool model of Goldbeter *et al* [63] and one-pool models of De Young Keizer *et al* [175] and Atri *et al* [2]) are reviewed in more detail. Interestingly for the DYK model we uncover an interesting global bifurcation structure (at least for a given set of parameter values). Because of the success of the DYK model in reproducing experimentally observed behaviour (such as the open probability of release) we use this as the basis for building a whole cell model, described in **Chapter 3**. **Chapter 2** also gives a brief overview of some models exhibiting more complex forms of Ca^{2+} oscillations, such as periodic bursting and chaotic behaviour. However, detailed aspects of these types of oscillations will not be studied in this thesis.

In **Chapter 3** we simplify the detailed biophysical DYK model of **Chapter 2** using a mathematical reduction process based on some biologically realistic assumptions regarding the time scale of binding and unbinding to receptor sites. Travelling wave behaviour in a whole cell model is then studied in this reduced model. We present a detailed numerical bifurcation analysis together with a linear stability analysis of Ca^{2+} wave propagation. We demonstrate that the model supports an interesting form of bifurcation structure including global and period doubling bifurcations. A variety

of propagating patterns are sustained by this model including travelling pulses and periodic travelling waves, $2n$ -periodic orbits and $2n$ -homoclinic orbits. Moreover, a kinematic theory of irregular wave propagation is used to predict the existence of a non-periodic travelling wave (that connects two periodic wave trains)

In the DYK model, as well as in other biophysical models of Ca^{2+} release, insight into behaviour is typically only possible with numerical analysis. One of the main ambitions of this thesis is to introduce a minimal model of Ca^{2+} release consistent with more detailed biophysical models, yet is analytically tractable. Importantly we shall introduce a mathematical framework to address issues of Ca^{2+} release and oscillation. This framework is based upon the deterministic Fire-Diffuse-Fire (FDF) model of Keizer *et al* [88] which uses a threshold process to mimic the nonlinear properties of Ca^{2+} channels. The main advantages of studying FDF type models are the possibility to analyse them exactly with both continuous and discrete distributions of Ca^{2+} release sites. In Chapters 4 and 5 we consider continuum and discrete distribution of release sites respectively.

In **Chapter 4**, we introduce the generalised version of the FDF model. The distribution of Ca^{2+} release sites is continuous in this chapter. The generalisation, firstly, incorporates a time dependent threshold to mimic refractoriness of release sites and, secondly, the notion of IP_3 sensitivity motivated by a reduction of the DYK model. Mathematical analysis is used to highlight the ability of the generalised FDF model to describe realistic Ca^{2+} waves and in particular solitary and periodic waves. The parameters of the FDF model are constrained using numerical data from the biophysical DYK model. This allows a direct comparison between these models.

In **Chapter 5**, we study the FDF model with a more biologically realistic distribution of release sites. In the first part of the chapter, we investigate how a regular array of release sites influences the propagation of saltatory travelling waves (with non-constant profile). By considering calcium stores as idealised point sources we are

able to explicitly construct solutions of the FDF model that correspond to saltatory solitary and periodic travelling waves. Moreover, the simplicity of the underlying deterministic FDF model can lead to further computational improvements. When considering a discrete set of release sites and calcium puffs or sparks that have a simple on/off temporal structure the calcium profile can be solved for in closed form. In the second part of the chapter, by assuming that release times occur on some regular lattice, we simplify the FDF model even further. The dynamics for release events is calculated via a thresholding of the calcium profile at a release site. By direct numerical simulation we illustrate that this computationally cheap version of the FDF model provides an accurate representation of the original model. We shall also demonstrate that it is both natural and straightforward to generalise our one-dimensional FDF model to two dimensions. Simulations for both one and two dimensions are presented with regular and disordered distribution of Ca^{2+} release sites. Varying system parameters reveals that the model supports many patterns of wave propagation behaviour including regular and irregular lurching travelling pulses, colliding and periodic waves, travelling fronts and spiral waves as well as abortive waves. These calcium wave formations have been widely observed experimentally in a variety of living cells.

Although theoretical work on Ca^{2+} dynamics has increased in recent years (reviewed in [149]), the spatially extended nature of the cell combined with the stochastic nature of localised calcium release and the heterogeneous distribution of Ca^{2+} stores has received far less attention.

In **Chapter 6** we introduce a model of calcium release based upon a stochastic generalisation of the FDF threshold model. The stochastic nature of release is incorporated via the introduction of a simple probabilistic rule for the release of calcium from internal stores. We illustrate that this is a natural way to investigate puff/spark to wave transitions within a spatially extended cell model with a discrete distribution of re-

lease sites. By avoiding a Markov process description of channel gating we side-step the need for computationally expensive Monte Carlo type simulations. Functional forms for the distribution of the incorporated threshold noise can be inferred from the recent observation of Izu *et al* [75] that the probability of release per unit time has a sigmoidal functional form. Numerical simulations are presented for both one- and two-dimensional cell models and demonstrate a variety of noise-sustained patterns of wave propagation. In the parameter regime where deterministic waves exist, it is possible to identify a critical level of noise defining a non-equilibrium phase-transition between propagating and abortive structures. A statistical analysis shows that this transition is the same as for models in the directed percolation universality class [70]. A study of a two-dimensional cell model illustrates that not only does the model support noisy circular and spiral waves as expected but that it can also exhibit a form of array enhanced coherence resonance [69, 73, 178]. We find that coherent motion, in the form of simultaneous and periodic release of calcium from all stores, can be induced purely by noise.

The Ca^{2+} oscillations and waves considered in the previous chapters have been characterised in single, and often isolated, cells. However, because many organisms are multi-cellular, there is a need for the intercellular communication of regulatory signals. One such form of cellular communication is an intercellular Ca^{2+} wave that spreads through multiple adjacent cells. These intercellular Ca^{2+} waves were first observed in epithelial and glial cell cultures in response to mechanical stimulation and neurotransmitters and have been observed later in many other cell types [140].

In Chapter 7, we investigate the issue of wave propagation failure through a cell culture. Once again we focus on two different models (DYK and FDF). The analysis (analytical and numerical) of intercellular waves in these two models will be divided into two parts. In the first part the intercellular Ca^{2+} wave is mediated by a passive diffusion of Ca^{2+} through gap junctions and the level of IP_3 concentration is constant.

throughout the tissue. In the second part, passive diffusion of IP_3 from the stimulated cell will be taken into account as well as Ca^{2+} propagation through the gap junction. We compare both models of intercellular Ca^{2+} waves in respect of wave propagation dependence on gap-junction permeability.

Finally in **Chapter 8** we present a summary of major achievements and natural extensions of this thesis.

Some important results of this thesis were published in [37, 164, 165] and are to appear in [36].

Chapter 2

Models of calcium oscillations

Cellular Ca^{2+} dynamics involves the exchange of Ca^{2+} ions between intracellular stores and the cytosol, the interior and exterior of a cell or between cells, as well as transport by diffusion and buffering due to the binding of Ca^{2+} to proteins, *e.g.* calmodulin and calbindin. Intracellular stores are typically located within the mitochondria, endoplasmic reticulum (ER) or sarcoplasmic reticulum (SR). The ER is an extensive membrane network of tubes and cisternae (sac-like structures) in many eukaryotic cells, important in the synthesis of proteins and lipids. The SR is the specific analogue of the ER in the cardiac, smooth and skeletal muscle. The ER/SR is the principle location of Ca^{2+} storage within the cell. The area between the plasma (outside) cell membrane and the ER/SR is called the cytosol, where most of the cellular metabolism occurs. Mitochondria are membrane-enclosed organelles distributed through the cytosol. They can transiently accumulate calcium during cell stimulation and provide the energy, for example, for cell movement, division and contraction. A schematic diagram of a cell with components relevant to Ca^{2+} dynamics is shown in Figure 2.1. The active elements of the ionic exchange processes through cell membranes are channels and pumps. Typically channels have an open and closed state as well as a host of intermediate states, and allow for flux of Ca^{2+} down its electro-

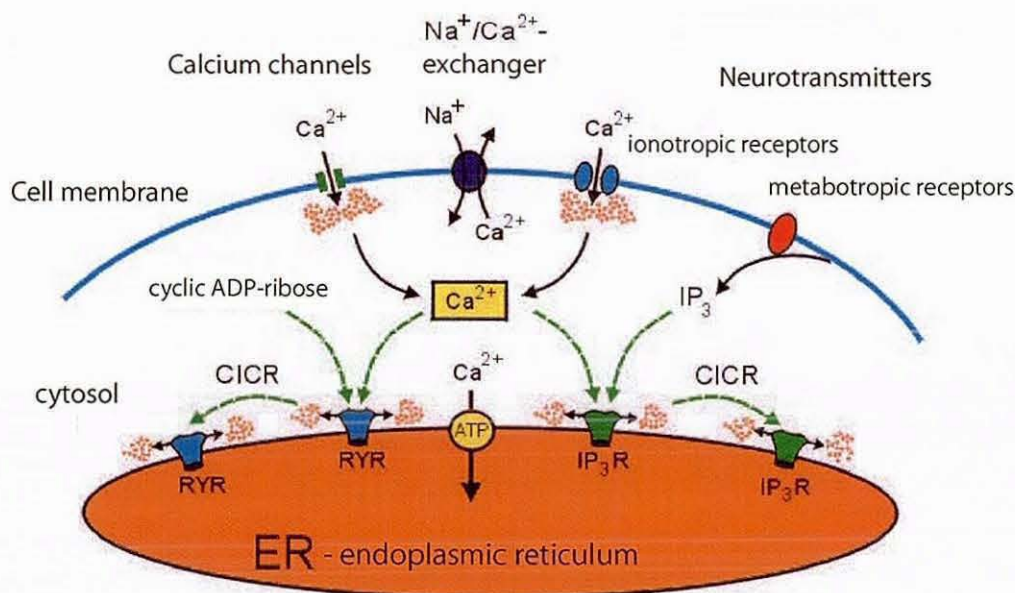


Figure 2.1: *Schematic diagram of the pathways involved in the control of cytosolic Ca^{2+} oscillations.*

chemical gradient when they are open. Pumps, on the other hand, transport Ca^{2+} against its electro-chemical gradient requiring a source of energy. The local dynamics of Ca^{2+} release and uptake can lead to oscillations in the free cytosolic calcium concentration. Such oscillations are believed to arise via nonlinear interactions between various cell components, including intracellular stores, pumps and channels and are often modelled using coupled ordinary differential equation descriptions of these sub-systems. The complexity of this modelling approach is greatly increased when spatial aspects, such as spatial separation of receptors, SR/ER microstructure, and functional distinction between cell periphery and cell bulk, are brought into play. For theorists, one of the most interesting aspects of Ca^{2+} dynamics is that local oscillations can be spread by ionic transport to form complex spatio-temporal patterns such as oscillatory waves, spiral waves, and waves that travel from cell to cell. Not only are these structures physiologically important (see Chapter 1), they are also mathematically interesting and challenging to understand in their own right. The

strength of mathematical models and analysis is twofold 1) mathematical models help to quantify experimentally obtained data and 11) models yield qualitative insight into processes which are not experimentally accessible

The deterministic modelling of Ca^{2+} signalling has historically been based on a well-established deterministic apparatus to describe self-sustained oscillations in chemistry and physics using nonlinear differential equation systems Local dynamics in these systems is typically excitable, oscillatory or bistable For sufficiently large perturbations, excitable dynamical systems respond to small perturbations of a linearly stable stationary state with a large amplitude excursion, that ultimately returns the system to rest Oscillatory dynamical systems are different in that they exhibit sustained oscillations, typically around an unstable fixed point Finally, bistability refers to systems with two stable stationary states, perhaps separated by an unstable state In the present chapter, we focus on the temporal organisation of intracellular Ca^{2+} signals and review some basic approaches in the mathematical modelling of Ca^{2+} oscillations Spatio-temporal aspects such as calcium waves are not included in the mathematical treatments of Ca^{2+} signalling in this chapter and will be considered later Before discussing theoretical models of Ca^{2+} oscillations, we first overview the regulatory mechanisms involved in the control of Ca^{2+} concentration within a cell This leads us to a more detailed discussion of the types of channel regulating Ca^{2+} influx and efflux, the energetic mechanisms underlying refilling of intracellular stores and the chemical pathways that ultimately lead to calcium release in response to an external agonist

2.1 Calcium dynamics

The mechanism of Ca^{2+} oscillations relies on feedback processes that regulate Ca^{2+} levels within the cell Whilst extracellular Ca^{2+} concentration varies between 1 and 2 mM, Ca^{2+} concentration in the cytosol is maintained at a resting level between 50-100

nM. Following cellular stimulation, cytosolic Ca^{2+} can transiently rise to between 1 and 10 μM [17]. Although increases in cytosolic Ca^{2+} are necessary for many cellular processes, sustained elevations in cytosolic Ca^{2+} are cytotoxic and may lead to cell death. Thus, it is necessary for the cell to strictly regulate cytosolic Ca^{2+} levels within defined limits. In order to achieve this the cell has developed a repertoire of Ca^{2+} channels, binding proteins, pumps and exchangers [17].

Two classes of oscillations are readily distinguished: those that depend primarily on the influx of Ca^{2+} through channels from the extracellular space, and those that depend primarily on Ca^{2+} release from internal stores. In this latter class, distinctions can be made on the basis of whether the release of Ca^{2+} is dominated by the ryanodine receptor (RyR), the inositol (1,4,5)-trisphosphate receptor (IP_3R) or a combination of both. IP_3Rs are the predominant Ca^{2+} release channels in non-electrically excitable (nonmuscle) cells, whereas RyRs are predominant in excitable (muscle) tissues [74]. In response to signals at the cell membrane, Ca^{2+} is released from the ER/SR into the cytosol in the form of global or spatially localised elementary events [21, 22]. The surface cell membrane consists of several different types of Ca^{2+} channels: voltage-operated calcium channels (VOCCs), that open in response to depolarisation of the cell membrane; receptor-operated channels, that open in response to the binding of an external ligand; second-messenger-operated channels, that open in response to the binding of a cellular second messenger; and mechanically operated channels, that open in response to mechanical stimulation. The mechanism of transduction of the signal at the cell membrane to the ER is dependent on the nature of the initial stimulus. In all cell types external ligand binding to its receptor channel initiates a cascade of signals which ultimately results in release of Ca^{2+} from the ER. The best characterised of these signals uses the diffusible second messenger IP_3 . The binding of an extracellular agonist such as a hormone or a neurotransmitter to a receptor in the surface cell membrane can cause, via a G-protein link to phospholipase C (PLC), the cleavage of phosphatidylinositol (4,5)-bisphosphate into diacylglycerol and IP_3 . IP_3

subsequently diffuses into the cell and binds to an IP_3R on the ER resulting in Ca^{2+} release [9]. However, in excitable cells, *i.e.* neurons and muscle, an action potential or activation of receptor operated channels results in influx of Ca^{2+} across the cell membrane which subsequently acts as the messenger to stimulate the RYRs, and also IP_3Rs , to release Ca^{2+} through an autocatalytic process referred to as calcium-induced calcium release (CICR) [47, 94]. Both the RYR and IP_3R are subject to several levels of regulation on the cytosolic face where Ca^{2+} can both promote and inhibit its release from either channel. At low concentrations Ca^{2+} stimulates Ca^{2+} release through the receptor, whereas at high Ca^{2+} concentration release is inhibited. Furthermore, at increasing Ca^{2+} concentration the IP_3R becomes more sensitive to ligand and less sensitive to Ca^{2+} dependent inhibition [134]. Thus, Ca^{2+} potentiates its own release and can stimulate release from neighbouring receptors. This mechanism of CICR for generating oscillations in the concentration of cytosolic free Ca^{2+} is believed to underlie the waves that propagate via Ca^{2+} diffusion in a variety of cell types [20].

Of equal importance to the regulation of Ca^{2+} release from the ER/SR are the mechanisms of Ca^{2+} clearance from the cytosol. This function is performed by a number of transporters located in the cell membrane and the ER/SR. One such transporter is the sarco- and endoplasmic reticulum calcium ATPase (SERCA) which is a Ca^{2+} pump located in the membrane of the SR and ER whose function is to accumulate Ca^{2+} into the internal stores using ATP as an energy source [102]. ATP is a ribonucleoside 5'-triphosphate functioning as a phosphate group donor in the cell energy cycle and carries chemical energy between pathways. SERCA functions are regulated by both cytosolic and ER/SR conditions. Under resting conditions SERCA is relatively inactive but following an increase in cytosolic Ca^{2+} the activity of the pump is increased, resulting in re-sequestration of Ca^{2+} into the ER [99]. From the other side, the Ca^{2+} pumping activity of SERCA is regulated by the Ca^{2+} content of the ER. SERCA activity is maximal when the store is depleted and decreases as the store approaches its maximal capacity [114]. There is also a $\text{Na}^+/\text{Ca}^{2+}$ -exchanger in the

cell membrane that uses the energy of the Na^+ electrochemical gradient to remove Ca^{2+} from the cell at the expense of Na^+ entry.

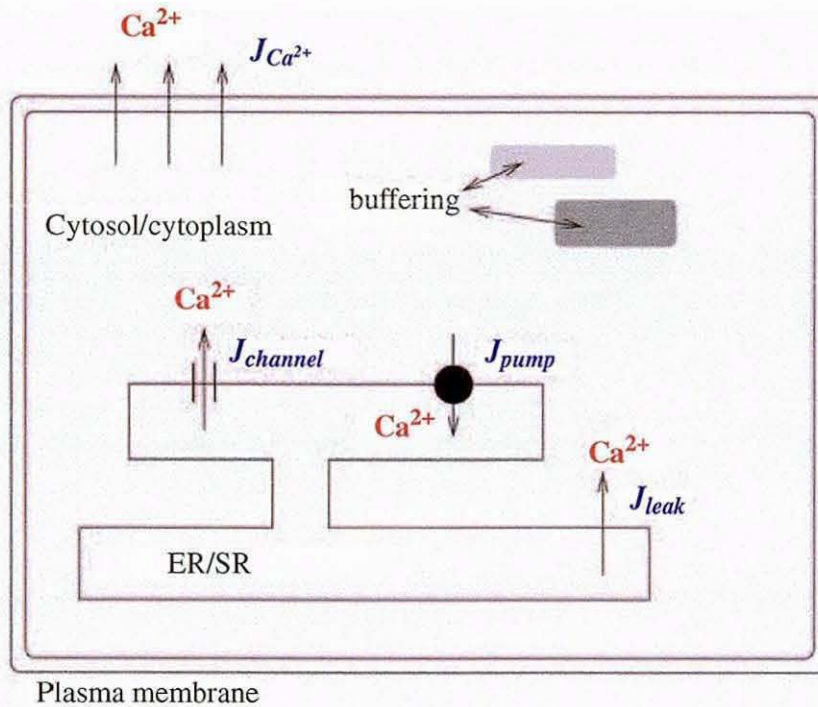


Figure 2.2: General scheme of the main processes involved in intracellular Ca^{2+} oscillations.

Many models of Ca^{2+} oscillations are based on the description of essential fluxes (see Figure 2.2). Calcium is removed from the cytosol in two principal ways: it is pumped out of a cell and is sequestered into ER/SR. Calcium influx also occurs via two principal pathways: inflow from the extracellular medium through Ca^{2+} channels in the surface membrane and release from internal stores. The construction of mathematical models is based on the formulation of flux balance equations for the various reactions and transport processes in the particular cell.

2.2 Theoretical models of Ca^{2+} oscillations

Two-pool model

One of the earliest models for IP_3 -dependent Ca^{2+} release assumes the existence of two distinct internal stores, one of which is sensitive to IP_3 , the other is sensitive to Ca^{2+} [62, 63, 89]. The model assumes the IP_3 produced in response to the agonist stimulation releases Ca^{2+} from the IP_3 -sensitive store through IP_3Rs . The Ca^{2+} that is thereby released stimulates the release of further Ca^{2+} from the Ca^{2+} -sensitive store. A crucial assumption of the model is that the concentration of Ca^{2+} in the IP_3 -sensitive store remains constant, as the store is quickly refilled from the extracellular medium. A schematic diagram of this model is shown in Figure 2.3. The

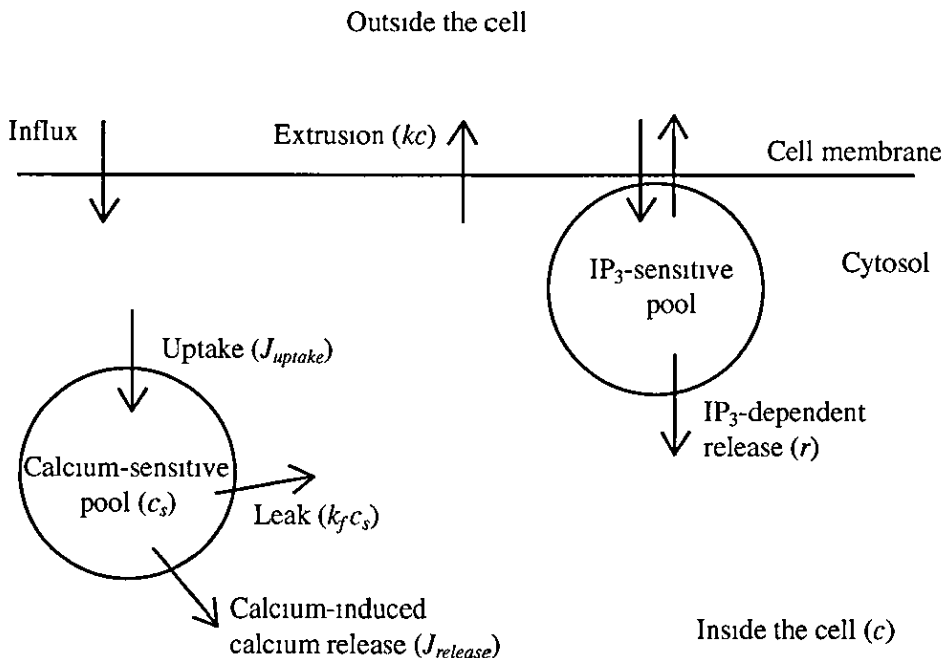


Figure 2.3 Schematic diagram of the calcium fluxes involved in the two-pool model of Ca^{2+} oscillations

concentrations of Ca^{2+} in the cytosol and in the Ca^{2+} -sensitive pool are denoted by c

and c_s respectively. The model assumes that IP_3 causes a steady flux r of Ca^{2+} into the cytosol, and that Ca^{2+} is pumped out of the cell at the rate $-kc$. Then, assuming a homogeneous system, the model equations are

$$\frac{dc}{d\tau} = r - kc - \tilde{f}(c, c_s), \quad (2.1)$$

$$\frac{dc_s}{d\tau} = \tilde{f}(c, c_s), \quad (2.2)$$

where

$$\tilde{f}(c, c_s) = \underbrace{\frac{V_1 c^n}{K_1^n + c^n}}_{J_{\text{uptake}}} - \underbrace{\left(\frac{V_2 c_s^m}{K_2^m + c_s^m} \right) \left(\frac{c^p}{K_3^p + c^p} \right)}_{J_{\text{release}}} - \underbrace{k_f c_s}_{J_{\text{leak}}} \quad (2.3)$$

and τ denotes time. The function \tilde{f} describes the dynamics of Ca^{2+} exchange between the cytosol and the Ca^{2+} -sensitive pool. The first term J_{uptake} is the rate at which Ca^{2+} is pumped from the cytosol into the Ca^{2+} -sensitive pool by an active process, the second term J_{release} is the rate at which Ca^{2+} is released from the Ca^{2+} -sensitive pool, and the third term is the rate at which Ca^{2+} leaks from the Ca^{2+} -sensitive pool into the cytosol. J_{release} demonstrates that Ca^{2+} stimulates its own release through the positive feedback process of CICR [48, 50]. In this model r denotes the constant concentration of IP_3 and is treated as a control parameter.

It is simple to nondimensionalise the model equations to get

$$\epsilon \frac{du}{dt} = \epsilon(\mu - u) - \gamma f(u, v), \quad (2.4)$$

$$\epsilon \frac{dv}{dt} = f(u, v), \quad (2.5)$$

$$f(u, v) = \beta \left(\frac{u^n}{u^n + 1} \right) - \left(\frac{v^m}{v^m + 1} \right) \left(\frac{u^p}{\alpha^p + u^p} \right) - \delta v, \quad (2.6)$$

where u and v are the nondimensional concentrations of Ca^{2+} in the cytosol and in the Ca^{2+} -sensitive pool respectively, and μ denotes the nondimensionalised IP_3 .

concentration (for more detailed discussion see [85]) By letting $w = u + \gamma v$ the two-pool model can be put into the form of a generalised FitzHugh-Nagumo model for describing excitable membrane [56, 116]

$$\frac{dw}{dt} = \mu - (w - \gamma v), \quad (2.7)$$

$$\epsilon \frac{dv}{dt} = f(w - \gamma v, v) \quad (2.8)$$

The characteristic of FitzHugh-Nagumo type models common to many biological mechanisms at the cellular level is a linear nullcline for the slow variable and a cubic nullcline that has either "N" shape or inverted "N" shape for the fast variable. The nullclines ($dw/dt = 0$, $dv/dt = 0$) of the two-pool model in Figure 2.4 demonstrate this well-known structure of excitable system which is sufficient to produce oscillatory behaviour.

The stability of the steady state (u_0, v_0) given by

$$u_0 = \mu, \quad (2.9)$$

$$f(\mu, v_0) = 0 \quad (2.10)$$

is determined by the roots of the characteristic equation

$$\lambda^2 + H\lambda - \frac{f_v}{\epsilon} = 0, \quad H = \frac{1}{\epsilon} (\gamma f_u(u_0, v_0) - f_v(u_0, v_0) + \epsilon) \quad (2.11)$$

Since $f_v < 0$, the roots of the characteristic equation (2.11) have negative real part (and the steady state is stable) if $H > 0$, and they have positive real part if $H < 0$. At $H = 0$ the steady state changes stability through a Hopf bifurcation (HB), and at these points a branch of periodic orbits appears. Oscillatory behaviour in dynamical systems is most easily summarised by a bifurcation diagram. For their numerical construction we use the software package AUTO [46], as implemented in XPPAUT (see Appendix A.1). The bifurcation diagram for the two-pool model as a function of

the main parameter μ is shown in Figure 2.5. As μ is increased, oscillations appear at a supercritical HB and disappear in the same manner. The two bifurcation points are connected by a branch of stable periodic orbits. Oscillations occur for a constant value of μ . This shows that CICR mechanism is sufficient to produce oscillations in the absence of IP_3 oscillations. The function of IP_3 here is to produce a steady influx of Ca^{2+} into the cytosol from the IP_3 -sensitive pool, and this steady influx drives Ca^{2+} oscillations. A typical example of oscillations given in Figure 2.6 shows pronounced spike-like behaviour, in agreement with many experiments.

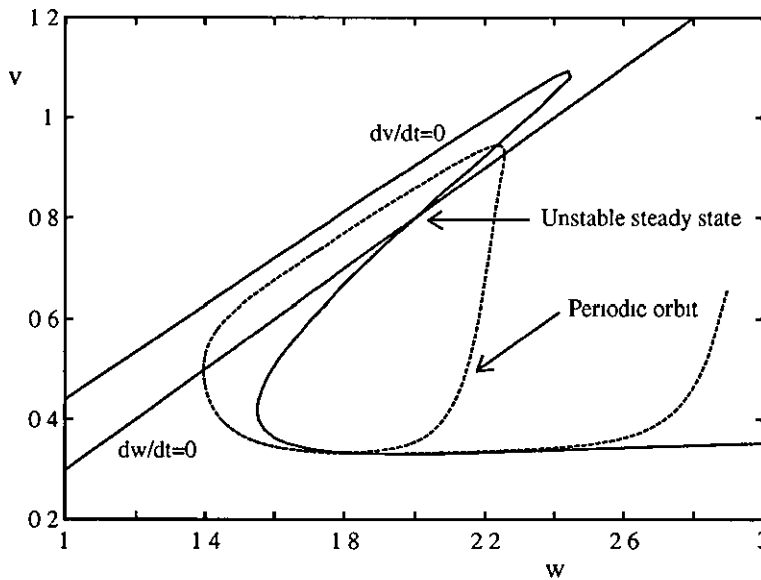


Figure 2.4: *Nullclines (solid curves) and sample limit cycle of periodic orbit (dashed curve) of the two-pool model in the form given by equations (2.7) and (2.8) for the following parameters $\mu = 0.4$, $\gamma = 2$, $\epsilon = 0.04$, $\beta = 0.13$, $\alpha = 0.9$, $\delta = 0.004$, $n = 2$, $m = 2$, $p = 4$. Intersection of the nullclines corresponds to the steady state value*

In the two-pool model Ca^{2+} stimulates its own release, while the flow of Ca^{2+} from the internal store is terminated when the concentration of Ca^{2+} in the internal store becomes too low. However, more recent experimental evidence indicates that not only does Ca^{2+} stimulate its own release, it also inhibits it, but on a slower time

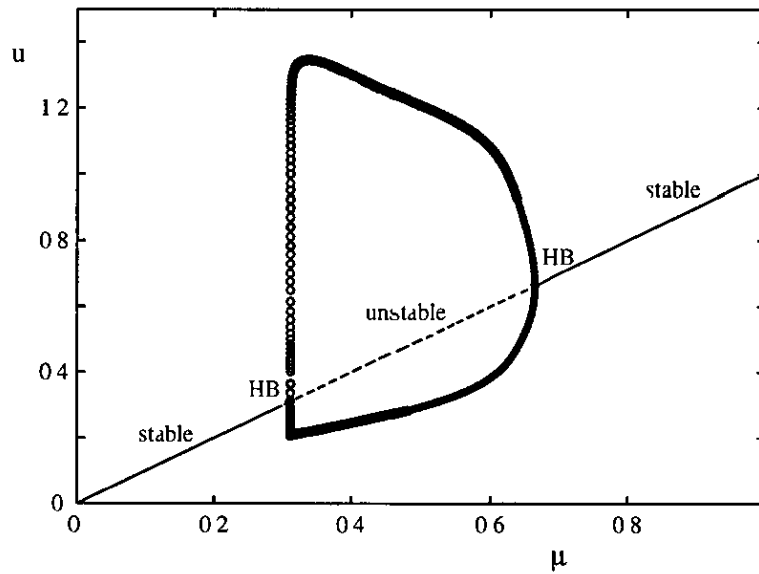


Figure 2.5 Bifurcation diagram of the two-pool model for the following parameters $\gamma = 2$, $\epsilon = 0.04$, $\beta = 0.13$, $\alpha = 0.9$, $\delta = 0.004$, $n = 2$, $m = 2$, $p = 4$. Circles denote amplitude of periodic orbit. HB Hopf bifurcation.

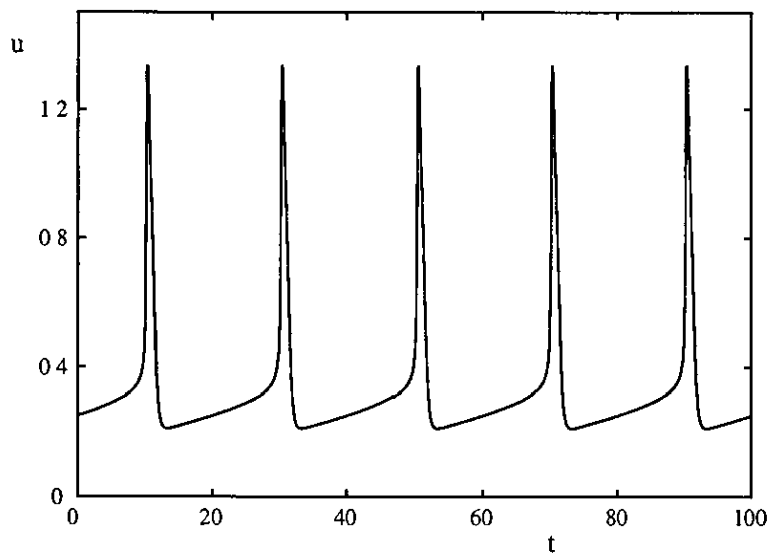


Figure 2.6 An example of periodic oscillations in the two-pool model for $\mu = 0.32$.

scale [123]. It is believed that this sequential activation and inactivation of the IP_3R by Ca^{2+} is the fundamental mechanism underlying IP_3 -dependent Ca^{2+} oscillations and waves. A number of models which incorporate this hypothesis have appeared and been reviewed, for example, in [153] and [161]. Two basic modelling approaches have been developed. One of them, developed by De Young and Keizer [175], mimics the molecular subunit configuration of the IP_3R to reflect the activation/inactivation sequence of the channel that results from the binding of Ca^{2+} and IP_3 to the IP_3R . An alternative approach, explored by Atri *et al* [2] is the construction of a model based on the kinetic data of Ca^{2+} release through the IP_3R of the same form as FitzHugh-Nagumo type models [56, 116]. We now consider these two approaches in more detail.

The De Young Keizer model

The biophysical DYK model [175] assumes that the IP_3R is composed of three independent and identical subunits. Each of the subunits includes a binding site for activating IP_3 , activating Ca^{2+} and inactivating Ca^{2+} . Only binding of IP_3 on the activating IP_3 site and binding of Ca^{2+} on the Ca^{2+} activating site leads to a Ca^{2+} flux through the receptor. Each state of the subunit is given by x_{ijk} , $i, j, k \in \{0, 1\}$, where the first index refers to the IP_3 binding site, the second to the Ca^{2+} activation site, and the third to the Ca^{2+} inactivation site. If any of the indices i , j or k are equal to 1, the binding site is occupied, otherwise the binding site is unoccupied. The model generates eight possible receptor states with correlated transitions between them (see Figure 2.7) where p and c denote IP_3 and Ca^{2+} concentrations respectively. The differential equations for the receptor states are based on mass-action kinetics. For example,

$$\frac{dx_{000}}{dt} = -(v_1 + v_2 + v_3), \quad (2.12)$$

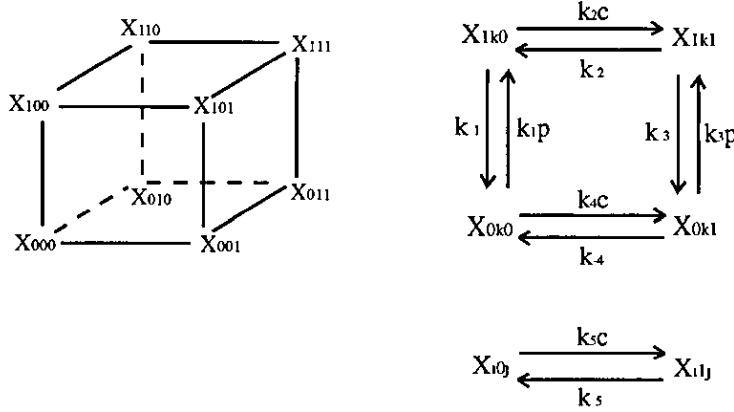


Figure 2.7 Schematic binding diagram for the IP_3 receptor model of De Young and Keizer

where

$$v_1 = k_1 p x_{000} - k_{-1} x_{100} \quad (2.13)$$

$$v_2 = k_4 c x_{000} - k_{-4} x_{001} \quad (2.14)$$

$$v_3 = k_5 c x_{000} - k_{-5} x_{010} \quad (2.15)$$

Since experimental data indicates that the receptor subunits act in a cooperative fashion, the model assumes that the IP_3R passes Ca^{2+} current only when three subunits are in the state x_{110} , and thus the open probability of the receptor is x_{110}^3 . The full DYK model consists of seven differential equations for the receptor states (with the constraint $\sum_{i,j,k} x_{ijk} = 1$, expressing conservation of probability) and with the following differential equation for Ca^{2+} dynamics

$$\frac{dc}{dt} = \underbrace{(r_1 x_{110}^3 + r_2)}_{J_{\text{receptor flux}}} (c_{\text{er}} - c) - \underbrace{\frac{r_3 c^2}{c^2 + k_p^2}}_{J_{\text{pumping}}} \quad (2.16)$$

where c_{er} denotes the concentration of Ca^{2+} in the ER. The first term in this equation is the Ca^{2+} flux through the IP_3R , and it is proportional to the concentration difference between the ER and the cytosol. A constant r_2 characterises an IP_3 -independent

| | | | | | |
|-------|-------------------------|----------|-----------------|----------|-------------------------|
| k_1 | $400 \mu M^{-1} s^{-1}$ | k_{-1} | $52 s^{-1}$ | r_1 | $20 s^{-1}$ |
| k_2 | $0.2 \mu M^{-1} s^{-1}$ | k_{-2} | $0.21 s^{-1}$ | r_2 | $0.004 s^{-1}$ |
| k_3 | $400 \mu M^{-1} s^{-1}$ | k_{-3} | $377.36 s^{-1}$ | r_3 | $1.2 \mu M^{-1} s^{-1}$ |
| k_4 | $0.2 \mu M^{-1} s^{-1}$ | k_{-4} | $0.029 s^{-1}$ | k_p | $0.1 \mu M$ |
| k_5 | $20 \mu M^{-1} s^{-1}$ | k_{-5} | $1.65 s^{-1}$ | c_{er} | $1 \mu M$ |

Table 2.1 Parameters of the DYK model

leak from the ER into the cytosol. The second term describes the action of Ca^{2+} ATPases that pump Ca^{2+} from the cytosol into the ER. Experimental data shows that the Ca^{2+} ATPase is cooperative, with a Hill coefficient of 2. One of the key properties used in formulating models of the IP_3R is the experimental analysis of the open channel probability as a function of $[Ca^{2+}]$. Bezprozvanny *et al* [18] showed that this open probability is a bell-shaped function of cytosolic Ca^{2+} . Thus, at low $[Ca^{2+}]$, an increase in $[Ca^{2+}]$ increases the open probability of the receptor, while at high $[Ca^{2+}]$ an increase in $[Ca^{2+}]$ decreases the open probability. Parameters in the model are usually chosen to obtain agreement with this steady-state data. Figure 2.8 shows the calculated equilibrium open probability of the IP_3R as a function of cytosolic Ca^{2+} concentration for the parameters given in Table 2.1. This plot demonstrates this bell-shaped function of open probability that realistically decreases for lower levels of $[IP_3]$. The kinetic property of the IP_3R that the receptor is activated quickly by Ca^{2+} , but inactivated by Ca^{2+} on a slower time scale, is incorporated in the magnitude of the rate constants.

The bifurcation diagram of the DYK model as a function of the main bifurcation parameter p is shown in Figure 2.9. This diagram demonstrates that the curve of steady states folds up, forming two limit points (LPs). Between these LPs three solutions exist for a small window of p values. For low and high IP_3 concentration there is only one stable fixed point. For the parameter values of p where the system has an unstable steady state periodic oscillations occur. The branch of stable periodic orbit

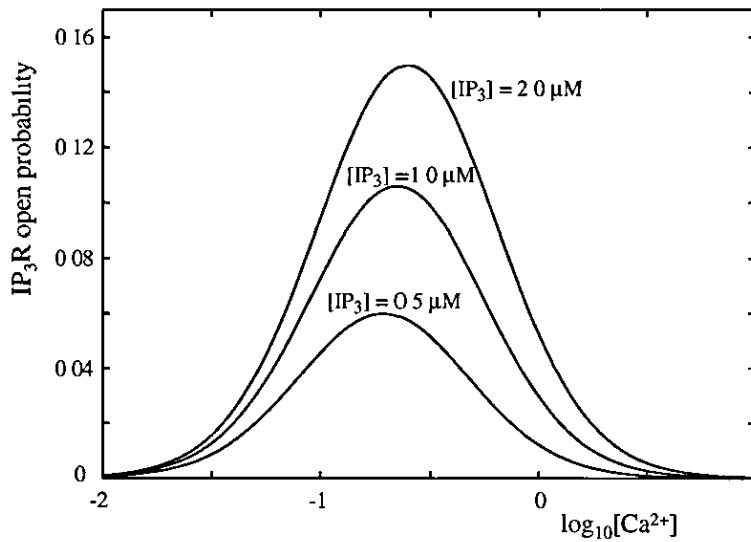


Figure 2.8 The steady-state open probability of the IP_3R , as a function of cytosolic $[Ca^{2+}]$ from the DYK receptor model at three different IP_3 concentrations

is broken into two different branches, both of which arise in a homoclinic bifurcation (HC) and end in a supercritical HB. A typical example of periodic oscillations in the DYK model is shown in Figure 2.10. Though for our choice of the parameters the DYK model demonstrates a complicated form of bifurcation structure, this is not always the case. For some parameters in the physiological range, the model shows a bifurcation structure similar to that seen in the two-pool model. This is illustrated in Figure 2.11 where with an increase in IP_3 periodic orbits appear via a supercritical HB and disappear in the same manner. These HB points are connected by a stable branch of periodic orbits.

The Atri model

One of the other approaches to modelling Ca^{2+} release, suggested by Atri *et al.* [2], assumes that Ca^{2+} inactivates the IP_3 receptor in a cooperative manner. In this model the IP_3R consists of three binding domains, the first of which binds IP_3 , the other two binding Ca^{2+} , and it is assumed that the receptor passes Ca^{2+} current only

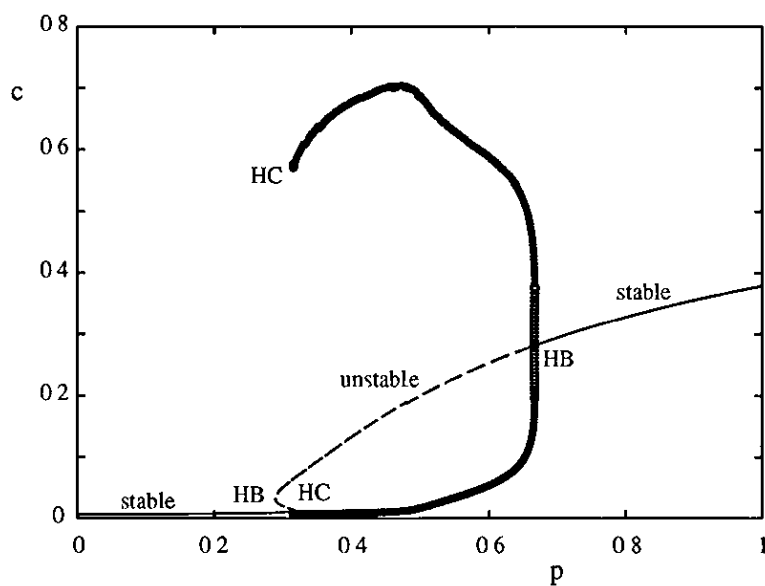


Figure 2.9 Bifurcation diagram of the DYK model. Circles denote amplitude of periodic orbit. HB Hopf bifurcation, HC homoclinic bifurcation.

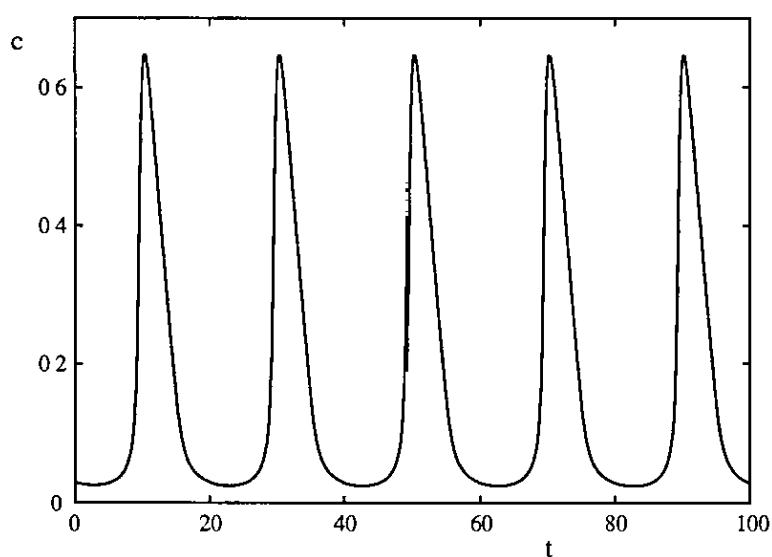


Figure 2.10 An example of periodic orbit in the DYK model for $p = 0.35$.

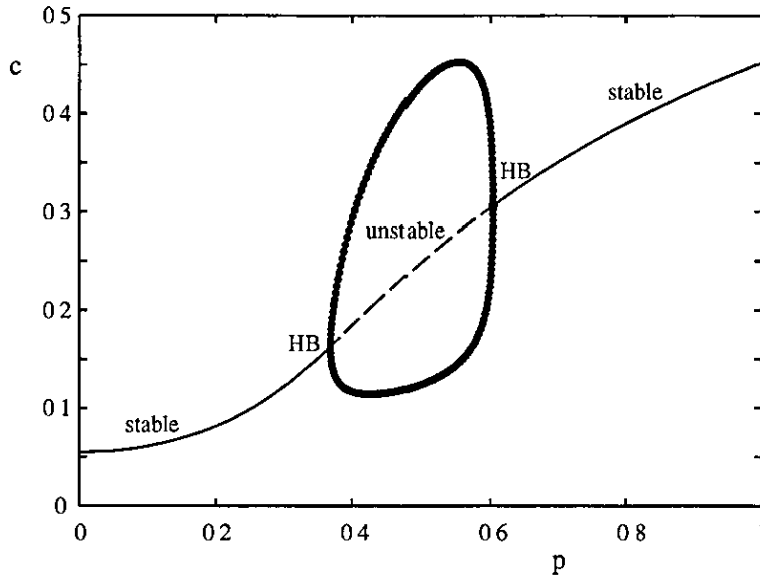


Figure 2.11 Bifurcation diagram of the DYK model for the following parameters $r_1 = 6$, $r_2 = 0.108$, $r_3 = 0.76$, $c_{er} = 1.69$. Other parameters are as in Table 2.1

when IP_3 is bound to domain 1, Ca^{2+} is bound to domain 2 and is not bound to domain 3. Each binding domain which is independent of the other domains consists of a number of binding sites. If p_1 is the probability that IP_3 is bound to domain 1, p_2 is the probability that Ca^{2+} is bound to domain 2, and $1 - p_3$ is the probability that Ca^{2+} is bound to domain 3, then the steady-state Ca^{2+} flux through the IP_3R is given by

$$J = k_f p_1 p_2 p_3 \quad (2.17)$$

for some constant k_f . The probabilities p_i , $i = 1, 2, 3$, have been chosen such that J agrees with the steady-state experimental data. Moreover, to complete the model it is assumed that p_1 and p_2 are instantaneous functions of $[\text{Ca}^{2+}]$ and $[\text{IP}_3]$, but that p_3 acts on a slower time scale, so that

$$J = k_f p_1 p_2 h, \quad (2.18)$$

where h is a time-dependent inactivation variable. Thus, the model satisfies the

| | | | |
|----------|---------------------|------------|--------------------|
| b | 0.11 | k_1 | 0.7 μM |
| β | 0.02 $\mu M s^{-1}$ | k_2 | 0.7 μM |
| γ | 2 $\mu M s^{-1}$ | k_γ | 0.1 μM |
| τ_h | 2 s | k_f | 8.1 $\mu M s^{-1}$ |

Table 2.2 Parameters of the Atri model

following equations

$$\frac{dc}{dt} = k_f \mu h \left(b + \frac{(1-b)c}{k_1 + c} \right) - \frac{\gamma c}{k_\gamma + c} + \beta \quad (2.19)$$

$$\tau_h \frac{dh}{dt} = \frac{k_2^2}{k_2^2 + c^2} - h, \quad (2.20)$$

where c denotes Ca^{2+} concentration, and $b, k_1, k_2, \gamma, k_\gamma$ and τ_h are constants. The first term in equation (2.19) is the Ca^{2+} flux through the IP_3 receptor. In a fashion similar to the DYK model, the second term represents pumping of Ca^{2+} out of the cytosol into the ER, and β represents a constant leak into the cytosol. μ is an increasing function of IP_3 concentration and is treated as the main bifurcation parameter. The values of other parameters are given in Table 2.2.

In Figure 2.12 we show the nullclines ($dc/dt = 0, dh/dt = 0$) of the Atri model for a fixed value of μ and the phase trajectory that corresponds to a periodic solution. Similar to the DYK model, the steady-state open probability of the IP_3R in the Atri model is a bell-shaped curve demonstrating a decrease in open probability for low and high cytosolic Ca^{2+} and increase for some intermediate Ca^{2+} level (see Figure 2.13). As expected the probability decreases with a decrease in IP_3 concentration. The bifurcation diagram of this model is shown in Figure 2.14 and a typical example of a stable periodic oscillation is shown in Figure 2.15. Note that the Atri model exhibits oscillations in a manner similar to the DYK model (with two HB points and two branches of periodic orbits both of which arise in a HC bifurcation), though

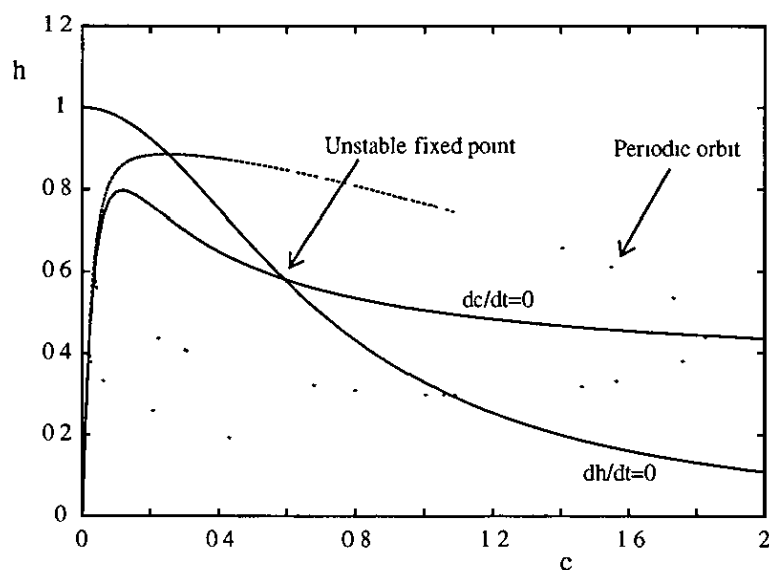


Figure 2.12 Nullclines (solid curves) and sample limit cycle of periodic orbit (dashed curve) of the Atri model for $\mu = 0.7$. Intersection of the nullclines corresponds to the steady state value

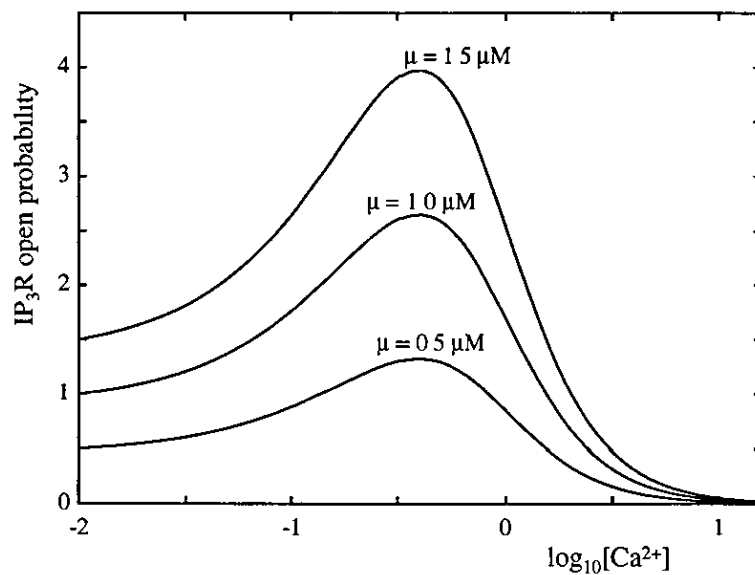


Figure 2.13. The steady-state open probability of the IP_3R , as a function of cytosolic $[Ca^{2+}]$ from the Atri receptor model at three different values of μ

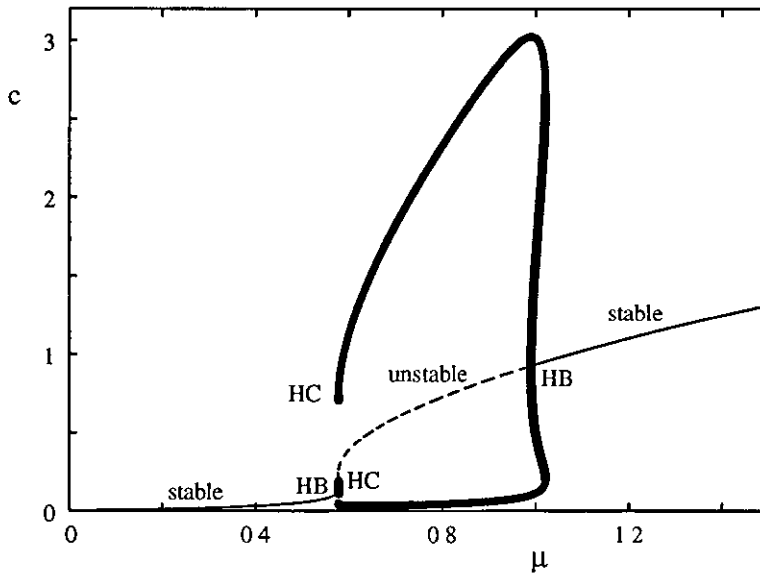


Figure 2.14 Bifurcation diagram of the Atri model. Circles denote amplitude of periodic orbit. HB Hopf bifurcation, HC homoclinic bifurcation

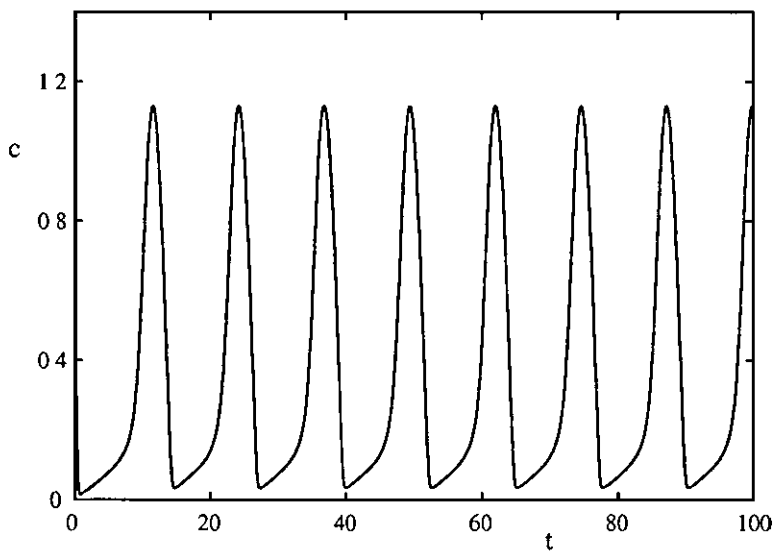


Figure 2.15 An example of periodic oscillations in the Atri model for $\mu = 0.6$

there are some differences between these two models. First, the Atri model does not include the factor $(c_{\text{er}} - c)$ in the term describing the IP_3 -sensitive Ca^{2+} current. Thus, it assumes that the concentration of Ca^{2+} in the ER is so high, that depletion of the ER has only a negligible effect on intracellular Ca^{2+} dynamics for most of the physiological regime. Also the form of the pumping term is different from that in the detailed DYK model, which uses a Hill equation with coefficient 2. There is experimental evidence that the form used in the DYK model is a more accurate description of the Ca^{2+} ATPase found in a variety of cell types [99]. Despite these differences, the similarities between the bifurcation structures of these two models suggest strongly that fast activation and slow inactivation of the IP_3R by Ca^{2+} is a significant mechanism underlying Ca^{2+} oscillations.

Bursting and chaos

As mentioned in the previous chapter, experimental results may show more complex forms of Ca^{2+} dynamics, for example, periodic or chaotic bursting. Such patterns of complex oscillations have been studied intensely in the case of transmembrane potential oscillations in electrically excitable cells [28, 29, 62, 85] and similar patterns are seen in Ca^{2+} bursting. One minor difference is that while often in electric bursting, each active phase comprises several consecutive, large spikes with nearly the same amplitude, in Ca^{2+} bursting single large spikes are followed by smaller 'secondary' oscillations.

These complex Ca^{2+} oscillations are typically believed to arise by the interplay between two oscillatory mechanisms. Shen and Larter [144], for example, have demonstrated regular bursting and a transition to chaos in a model involving differential equations for cytosolic Ca^{2+} , endoplasmic Ca^{2+} and IP_3 . Another model giving rise to bursting is based on the previously discussed two-pool model [63] with the Ca^{2+} level in the IP_3 -insensitive pool treated as a dynamical variable [23].

More recently another explanation of complex intracellular Ca^{2+} oscillations has been proposed [65, 108] where Ca^{2+} sequestration by mitochondria and the Ca^{2+} binding to cytosolic proteins is taken into account. These studies extend earlier work on modelling the possible mitochondrial modulation of Ca^{2+} signals [109]. Numerical simulations of these models demonstrate simple Ca^{2+} oscillations, periodic and aperiodic bursting and chaos under variation of parameter values. A model proposed by Kummer *et al* [90] uses variables for cytosolic Ca^{2+} , endoplasmic Ca^{2+} and the concentrations of active subunits of a G-protein and active PLC. This model shows particularly good agreement with experimental observations in two respects. First, each oscillation period starts with a large, steep spike followed by a number of pulses of decreasing amplitude around an elevated mean value. Second, varying the model parameters, one finds that the difference in stimulation nature can induce (periodic or aperiodic) bursting or regular oscillations (see Figure 2.16 for an example of typical chaotic bursting)

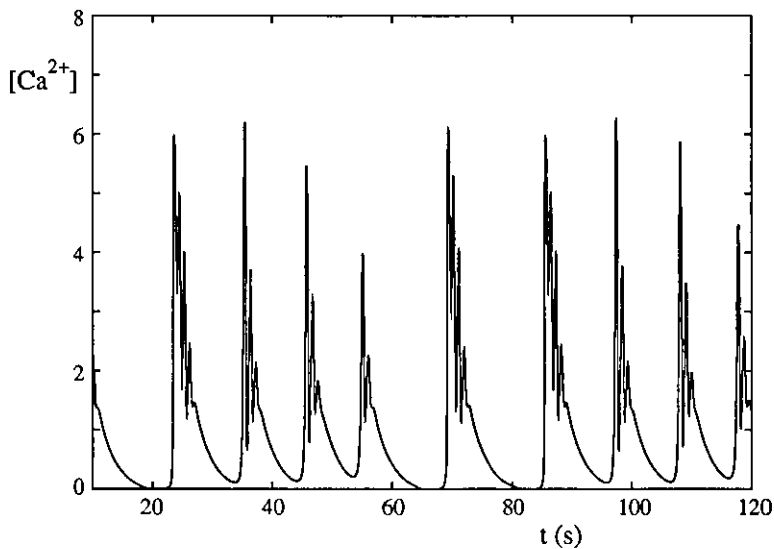


Figure 2.16 *An example of chaotic bursting in the Kummer model [90]*

Summary

In this chapter we have described the main components in a single cell such as the ER/SR, cytosol, calcium receptor channels and pumps that are involved in the regulatory mechanisms of cellular Ca^{2+} dynamics. We have also discussed some of the main theoretical models proposed for intracellular Ca^{2+} oscillations (for further reviews see [54, 85, 143]) A numerical bifurcation analysis of these models shows that the generation of Ca^{2+} oscillations occurs in a similar fashion under parameter variation, even though the model equations differ in their particular forms. We conclude that the major mechanism for generating oscillations in system with IP_3R is fast activation of IP_3R by IP_3 and slow inactivation by Ca^{2+} The extension of these basic models may lead to the formation of more complex patterns of Ca^{2+} oscillations such as bursting and chaos observed experimentally However, we do not consider these types of Ca^{2+} signals in this thesis

Chapter 3

The De Young Keizer model

In the preceding chapter, some of the standard models underlying Ca^{2+} oscillations and a review of their properties were introduced. One of the more popular of these is the DYK model [175] based around a detailed description of the dynamics for IP_3Rs . Firstly, this model makes it plausible that the experimental activation and inactivation by cytosolic Ca^{2+} of the IP_3 receptor/channel is sufficient to produce oscillations in calcium concentration. Secondly, the complete mechanism involves only a single internal pool of Ca^{2+} , the ER/SR. It is believed to be the first model that explains oscillations on the basis of only the IP_3 receptor/channel and a single Ca^{2+} pool.

The present chapter is dedicated to a study of travelling wave behaviour in this model using a systematic numerical bifurcation analysis. For the most recent set of experimentally determined parameter values the model supports an interesting form of bifurcation structure including global bifurcations. We also present a linear stability analysis of solutions and a kinematic theory of wave propagation based around dispersion curves for periodic waves. This allows us to predict the existence of travelling waves which connect periodic orbits. The prediction is subsequently confirmed with

direct numerical simulations

3.1 Reduction of the De Young Keizer model of Ca^{2+} release

The model developed by De Young and Keizer [175] describes IP_3 dependent Ca^{2+} oscillations between the ER and the cytosol. As the model has been explained in detail in the previous chapter, we give only a brief description here. The IP_3R model has eight possible receptor states. Transitions between these states are shown in Figure 2.7, where p and c denote IP_3 and Ca^{2+} concentrations respectively. Seven differential equations based on mass-action kinetics together with the constraint $\sum_{i,j,k} x_{ijk} = 1$ (conservation of probability) form a mathematical model of the IP_3R . The model assumes that IP_3R releases Ca^{2+} only when three subunits are in the state x_{110} , i.e. with one IP_3 and one activating Ca^{2+} bound. Thus the open probability of the receptor is x_{110}^3 . The set of differential equations for the receptor states are combined with the differential equation (2.16) for Ca^{2+} dynamics describing fluxes from the ER to the cytosol (Ca^{2+} release from IP_3Rs and constant leakage) and back (the action of SERCA pumps).

The complexity of such a detailed receptor model provides motivation to simplify the model with the retention of its essential properties. One simplification of the DYK model [175] was suggested by Li and Rinzel [96] who have shown that the original full model can be approximated by an excitable system of Hodgkin-Huxley form [71]. The Hodgkin-Huxley equations are the first quantitative model of the propagation of an electrical signal along a squid giant axon. The model of Hodgkin and Huxley was originally used to explain the action potential in the long giant axon of a squid nerve cell, but the ideas have since been extended and applied to a wide variety of excitable cells (see [85] for an excellent review). The experimental observation that

IP_3 and Ca^{2+} bind quickly to the activating site gives rise to the assumption that the receptor is in a quasi-steady state with respect to IP_3 binding and Ca^{2+} activation [86, 96, 161]. This is implied by the parameter values for the detailed receptor model shown in Table 2.1, where k_i and k_{-i} , $i = 1, 3, 5$, are significantly larger than k_i and k_{-i} , $i = 2, 4$. Thus, the receptor states can be arranged into two groups: those without Ca^{2+} bound to the inactivating site (x_{000} , x_{010} , x_{100} and x_{110}) called group I states, and those with Ca^{2+} bound to the inactivating site (x_{001} , x_{011} , x_{101} and x_{111}) called group II states. Because the binding of IP_3 and the binding of Ca^{2+} to the activating site are assumed to be fast processes, within each group the binding states are at quasi-steady state with respect to transitions within the group. The differential equations governing the states in group I are

$$\frac{dx_{000}}{dt} = -x_{000}(k_5c + k_1p + k_4c) + k_{-1}x_{100} + k_{-4}x_{001} + k_{-5}x_{010}, \quad (3.1)$$

$$\frac{dx_{100}}{dt} = -x_{100}(k_5c + k_{-1} + k_2c) + k_1px_{000} + k_{-2}x_{101} + k_{-5}x_{110}, \quad (3.2)$$

$$\frac{dx_{010}}{dt} = -x_{010}(k_{-5} + k_1p + k_4c) + k_{-1}x_{110} + k_{-4}x_{011} + k_5cx_{000}, \quad (3.3)$$

together with the equation for the inactivation variable called h

$$h = \sum_{i,j} x_{ij0} \quad (3.4)$$

Assuming that the group I binding sites are all in quasi-steady state, the quasi-steady-state equations are obtained by setting $dx_{000}/dt = dx_{100}/dt = dx_{010}/dt = 0$ and neglecting slow terms. Thus,

$$x_{000}(k_5c + k_1p) = k_{-1}x_{100} + k_{-5}x_{010}, \quad (3.5)$$

$$x_{100}(k_5c + k_{-1}) = k_1px_{000} + k_{-5}x_{110}, \quad (3.6)$$

$$x_{010}(k_{-5} + k_1p) = k_{-1}x_{110} + k_5cx_{000} \quad (3.7)$$

These equations may be solved together with the constraint (3.4) to give the group I

state probabilities which are found as

$$x_{000} = \frac{K_1 K_5 h}{(p + K_1)(c + K_5)}, \quad x_{100} = \frac{K_5 p h}{(p + K_1)(c + K_5)}, \quad (3.8)$$

$$x_{010} = \frac{K_1 c h}{(p + K_1)(c + K_5)}, \quad x_{110} = \frac{p c h}{(p + K_1)(c + K_5)}, \quad (3.9)$$

where $K_i = k_{-i}/k_i$. An identical procedure applied to the group II receptor states gives the quasi-steady-state equations for that group

$$x_{001} = \frac{K_3 K_5 (1 - h)}{(p + K_3)(c + K_5)}, \quad x_{101} = \frac{K_5 p (1 - h)}{(p + K_3)(c + K_5)}, \quad (3.10)$$

$$x_{011} = \frac{K_3 c (1 - h)}{(p + K_3)(c + K_5)}, \quad x_{111} = \frac{p c (1 - h)}{(p + K_3)(c + K_5)} \quad (3.11)$$

To derive a differential equation for h , we add the differential equations for the group I states with the inclusion of transitions between the group I and group II states and substitute all the quasi-steady-state expressions to get

$$\frac{dh}{dt} = \left[\frac{k_{-2}p + k_{-4}K_3}{p + K_3} \right] (1 - h) - \left[\frac{(k_{-4}K_1K_2 + k_{-2}K_4p)c}{K_2K_4(p + K_1)} \right] h \quad (3.12)$$

Thus, by regarding the receptor as being in a quasi-steady state with respect to IP_3 binding and Ca^{2+} activation the seven differential equations describing the kinetics of IP_3 receptor in the full DYK model is reduced to just one. Therefore, the reduced model is given by the two differential equations, one of which is the Ca^{2+} dynamics equation (2.16) with

$$x_{110} = \frac{p c h}{(p + K_1)(c + K_5)} \quad (3.13)$$

and another is the differential equation (3.12) for h . The dynamics of the inactivation variable h is reminiscent of that of the gating variables in the Hodgkin-Huxley model of nerve membrane [71] and can be written in the form

$$\tau(c) \frac{dh}{dt} = h_\infty(c) - h, \quad (3.14)$$

where

$$h_{\infty}(c) = \frac{\beta}{\alpha(c) + \beta}, \quad \tau(c) = \frac{1}{\alpha(c) + \beta}, \quad (3.15)$$

with

$$\alpha(c) = \frac{(k_{-4}K_1K_2 + k_{-2}K_4p)c}{K_2K_4(p + K_1)}, \quad \beta = \frac{k_{-2}p + k_{-4}K_3}{p + K_3} \quad (3.16)$$

In a certain range of the parameter p , the system has an excitable steady state, i.e. small (subthreshold) perturbations of the steady state decay exponentially, but larger (superthreshold) perturbations result in a large transient before the return to steady state. In Figure 3.1 we show the nullclines ($dc/dt = 0$, $dh/dt = 0$) of the reduced DYK model for the fixed value of p and the phase trajectory that corresponds to the periodic solution. The intersection of two nullclines corresponds to the steady state value. The typical periodic behaviour is represented in Figure 3.2 showing that the oscillations are very spike-like.

Oscillatory behaviour in the model is most easily summarised with a bifurcation diagram, using p as the main bifurcation parameter. A numerically constructed bifurcation diagram of the reduced model is shown in Figure 3.3. The curve of steady states is folded, so that for a small window of p values there are three solutions. For high and low p there is only stable fixed point. For the parameter values of p where the system has an unstable steady state periodic oscillations occur and the figure shows the maximum and minimum of the periodic orbit. In fact there are two disconnected branches of stable periodic orbits, both of which arise in a HC bifurcation and end in a supercritical HB. Oscillations of Ca^{2+} first occur with a large period and a very spiky profile. As p increases the period of oscillations rapidly decreases, as illustrated in Figure 3.4. Note that the bifurcation diagram of the reduced DYK model is in good qualitative agreement with that of the full model shown in Figure 2.9. The main difference is in the amplitude of the limit cycle oscillation close to the second HB. In the full DYK model the amplitude is slightly smaller than in the

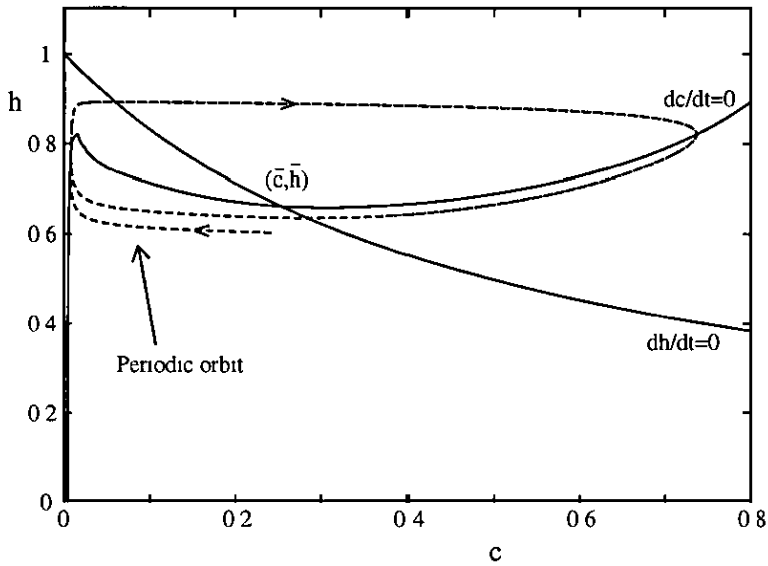


Figure 3.1 Nullclines (solid curves) and the phase trajectory (dashed curve) corresponding to the periodic solution of the model obtained for the parameter value $p = 0.6$. Intersection of the nullclines corresponds to the steady state (\bar{c}, \bar{h}) .

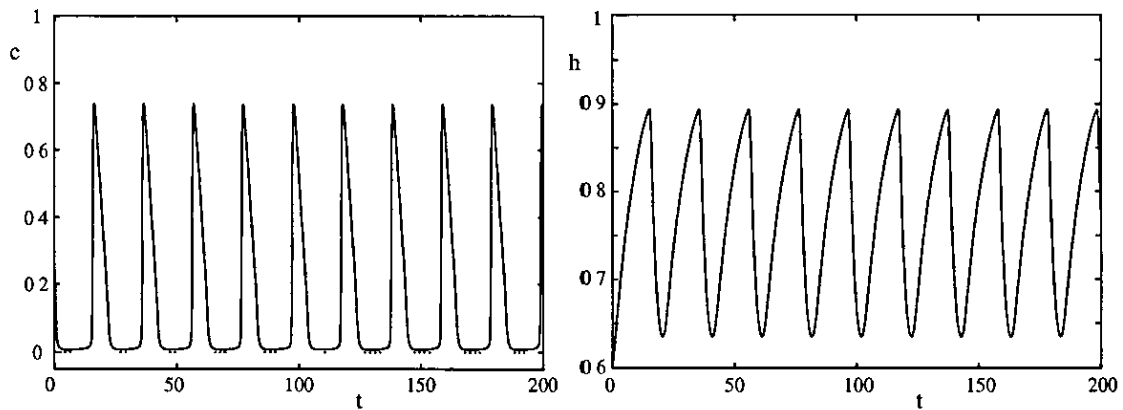


Figure 3.2 An example of a typical periodic orbit of the receptor model for $p = 0.6$ and the initial values $(c, h) = (0.24, 0.61)$.

reduced model. Importantly, the reduced model captures the essential features of the full model, namely a window of oscillations between two HBs, with three fixed points near the first of these. This suggests that the assumptions used in the mathematical reduction process are both realistic and effective for simplification of the DYK model.

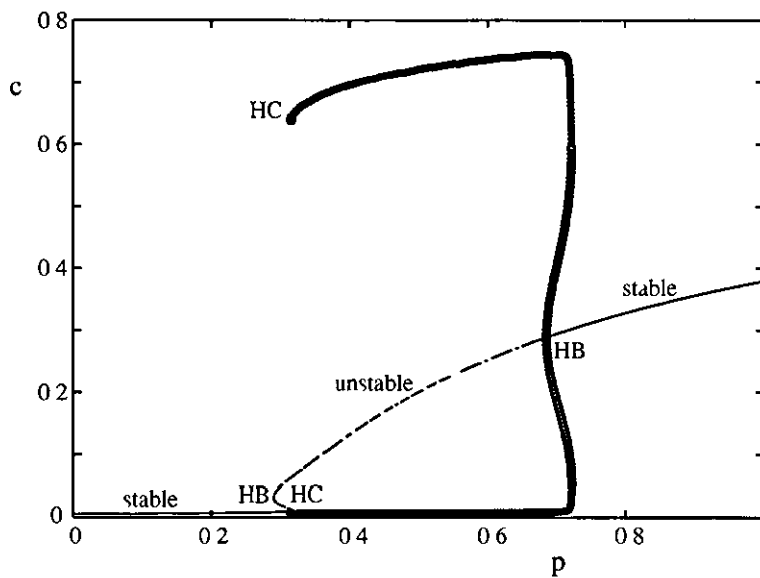


Figure 3.3 Bifurcation diagram of the reduced DYK model. Circles denote amplitude of periodic orbit. HB: Hopf bifurcation; HC: homoclinic bifurcation.

3.2 Travelling waves in the model

As we discussed earlier in Chapters 1 and 2, oscillations of intracellular calcium do not often occur uniformly throughout the cell, but are organised into repetitive intracellular waves [1, 9, 79, 136]. In large cells such as *Xenopus* oocytes, the intracellular waves develop a high degree of spatial organisation, forming concentric circles, plane waves, and multiple spirals [92, 93, 94].

The observed Ca^{2+} waves in many types of cells are believed to be the result of Ca^{2+}

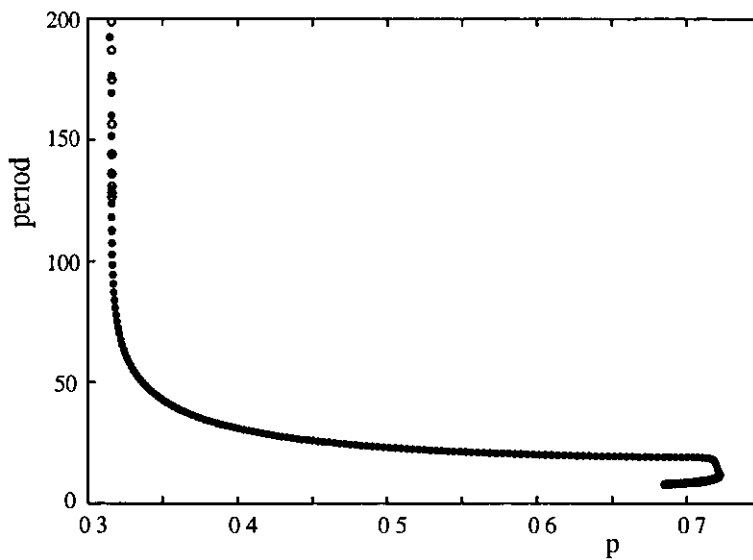


Figure 3.4 The period of the periodic orbit in the DYK model as a function of p

diffusion between Ca^{2+} release sites. Although travelling waves cannot be explained by diffusion in all types of cells, it is a reasonable assumption for modelling intracellular Ca^{2+} waves. According to this hypothesis, the cell cytosol forms either an excitable or an oscillatory system. In either of these cases the linking of release sites by diffusion can lead to coordinated waves of high Ca^{2+} concentration.

In actual physiological systems, cytosolic calcium is strongly buffered in the cell. Free Ca^{2+} ions typically constitute only 1% of the total calcium in the cytosol and measurements in cells indicate that buffer-bound calcium is at least an order of magnitude less mobile than free Ca^{2+} [91]. Generally speaking, these buffers are poorly mobile, and they reduce both the amount of free calcium and its ability to diffuse. Detailed models of calcium buffering have been studied by some researchers [80, 117, 119, 138]. Nowycky and Pinter [119], in particular, did a highly detailed study of the effects of various types of calcium buffers.

The chemical reaction for calcium buffering can be represented by the reaction



where P is the buffering protein and B is buffered calcium. If we let b and c denote the concentration of buffer with Ca^{2+} bound and the concentration of free Ca^{2+} respectively, then a simple model of calcium buffering is given by the following system of equations

$$\frac{\partial c}{\partial t} = D_c \nabla^2 c + f(c) + k_- b - k_+ c(b_t - b), \quad (3.18)$$

$$\frac{\partial b}{\partial t} = D_b \nabla^2 b - k_- b + k_+ c(b_t - b), \quad (3.19)$$

where k_- and k_+ are the rates of Ca^{2+} release from the buffer and uptake by the buffer respectively; b_t is the total buffer concentration, and $f(c)$ denotes all the other reactions involving free Ca^{2+} (for example, channel characteristics, Ca^{2+} pumps, Ca^{2+} leak etc). D_c and D_b define the diffusion coefficients of Ca^{2+} and buffer accordingly. If the buffer has fast kinetics, its effect on the intracellular Ca^{2+} dynamics can be simply analysed. Assuming that k_- and k_+ are large compared to the time constant of calcium reaction, we take b to be in the quasi-steady state $k_- b - k_+ c(b_t - b) = 0$, and so

$$b = \frac{b_t c}{K + c}, \quad K = k_-/k_+ \quad (3.20)$$

It follows that

$$\frac{\partial c}{\partial t} + \frac{\partial b}{\partial t} = (1 + V) \frac{\partial c}{\partial t}, \quad V = \frac{b_t K}{(K + c)^2} \quad (3.21)$$

Combining this equation with (3.18) and (3.19), we obtain

$$\begin{aligned} \frac{\partial c}{\partial t} &= \frac{1}{1 + V} \left(\nabla^2 \left(D_c c + D_b b_t \frac{c}{K + c} \right) + f(c) \right) \\ &= \frac{1}{1 + V} \left((D_c + D_b V) \nabla^2 c - \frac{2D_b V}{K + c} |\nabla c|^2 + f(c) \right) \end{aligned} \quad (3.22)$$

We see that nonlinear buffering changes the model and that Ca^{2+} obeys a nonlinear diffusion-advection equation, where the advection is the result of Ca^{2+} transport by a mobile buffer [169]. The *effective* diffusion coefficient is a linear combination of the two diffusion coefficients D_c and D_b and lies somewhere between the two. If the buffer is not mobile, i.e. $D_b = 0$, then (3.22) reverts to a reaction-diffusion equation, with a reduced diffusion coefficient.

Models with fast, immobile and unsaturated buffers have been considered by a number of authors [85, 91, 152, 156, 169]. There has been relatively little work done on Ca^{2+} transport by mobile buffers. However, it is known that inclusion of mobile buffers does not tend to eliminate an existing wave [152], although it can cause the appearance of two stable waves in some cases [148]. Little else is known about their effects on qualitative wave properties. In this thesis we ignore the complicating effects of Ca^{2+} buffers assuming that calcium buffering is included implicitly in the model (in both the cytosol and the ER) by treating all fluxes as effective fluxes, and using a small diffusion coefficient for Ca^{2+} . This is a realistic assumption in light of recent work that indicates buffer mobility has only a limited effect on wave properties [155]. Thus it is likely that inclusion of mobile buffers would have no qualitative effects on our results.

For the generation of Ca^{2+} waves in the model we add a term $D\nabla^2 c$ to the right hand side of equation (2.16), where D is an *effective* diffusion coefficient. We shall restrict our attention to one spatial dimension for a detailed understanding of wave propagation using a mixture of analysis and numerics. We also ignore any effects of heterogeneity within a single cell. Though this assumption cannot be justified on physiological grounds, the effects of discreteness on wave propagation are unlikely to be understood until wave propagation in a homogeneous medium is understood. Later, in Chapter 5, we relax the assumption of homogeneity.

For travelling waves with fixed velocity s it is convenient to rewrite the DYK model

in the comoving reference frame where $\xi = x - st$. A transformation into this frame yields

$$\partial_t c = D \partial_\xi^2 c + s \partial_\xi c + f_1(c, h) \quad (3.23)$$

$$\partial_t h = s \partial_\xi h + f_2(c, h), \quad (3.24)$$

where

$$f_1(c, h) = (r_1 x_{110}^3 + r_2)(c_{\text{er}} - c) - \frac{r_3 c^2}{c^2 + k_p^2}, \quad (3.25)$$

$$f_2(c, h) = \frac{h_\infty(c) - h}{\tau(c)} \quad (3.26)$$

In the comoving frame, travelling waves with speed s correspond to stationary solutions defined by $\partial_t c = \partial_t h = 0$. Hence, they can be found by studying solutions to the travelling wave ODEs

$$\frac{dc}{d\xi} = w, \quad D \frac{dw}{d\xi} = -sw - f_1(c, h), \quad s \frac{dh}{d\xi} = -f_2(c, h) \quad (3.27)$$

Travelling pulses correspond to a homoclinic orbit in these equations, whilst periodic wave-trains correspond to limit cycle oscillations. Fixed points of the travelling wave ODEs correspond to homogeneous states of the spatially extended model.

We present a numerical analysis of the travelling wave ODEs for the DYK model given by (3.27), treating $p = [\text{IP}_3]$ as the physiologically significant bifurcation parameter. Homoclinic orbits are expected to arise as the limit of periodic orbits as the period tends to infinity. All numerically computed homoclinic orbits presented here are just periodic orbits with large period, which for practical purposes we take as 10^4 .

3.2.1 Bifurcation analysis

For any fixed value of s we can construct the bifurcation diagram similar to that in Figure 3.3 and find the values of p at which Hopf bifurcations occur. These bifurcation points can be continued in the (p, s) parameter plane. In Figure 3.5 we trace the locus

of Hopf bifurcations labeled HB, as well as three branches of homoclinic orbits labeled HC defining solitary travelling pulses. The Hopf bifurcations curve forms a distinct loop since the curve of steady states of Ca^{2+} oscillations has the S-shape as shown in Figure 3.3. The behaviour of the system as $s \rightarrow \infty$ is exactly that of the model in the absence of diffusion, as expected from the general theory [103]. Thus, for large values of s there are two Hopf bifurcations and only two homoclinic bifurcations (labelled (B) and (C)). The branch of periodic orbits that originates on the right most Hopf bifurcation ends in a homoclinic bifurcation on branch B, while the branch of periodic orbits arising from the left most Hopf bifurcation ends in a homoclinic bifurcation on branch C.

For intermediate values of s only one of the three homoclinic branches (labelled (A)) occupies a significant window of p values. This homoclinic branch arises from the branch of periodic orbits that originates on the right most Hopf bifurcation and solitary waves on this branch fail to propagate if p is too small. We now discuss some aspects of this bifurcation diagram which are interesting from a dynamical systems perspective.

First of all, we take a closer look at the upper part of homoclinic orbit branch A and show a magnified view of Figure 3.5 in Figure 3.6. The homoclinic branch A is found to end at a T-point [61]. This is a point where a heteroclinic cycle exists between a saddle and a saddle focus. Note that global bifurcations in this model can be directly linked to windows of parameter space where there are three fixed points. Previous work by Glendinning and Sparrow [61] predicts the existence of a winding homoclinic branch near a T-point. This phenomenon is clearly seen in Figure 3.6, where the homoclinic branch B connects to homoclinic branch A in a spiral. Figure 3.7 (A and B) shows the heteroclinic cycle between two fixed points at the T-point: a whole cycle and magnified view of the cycle in the neighbourhood of the saddle focus and the saddle point. The spiral of homoclinic orbit occurs when the homoclinic orbit

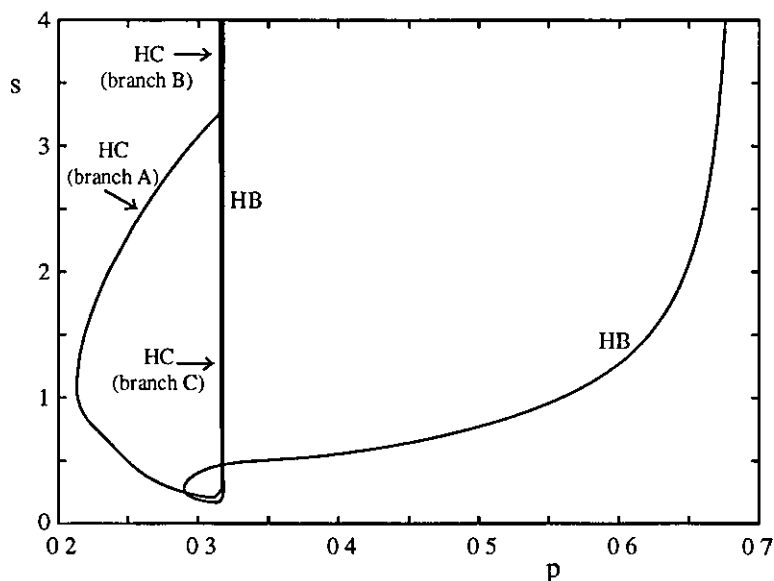


Figure 3.5 Two-parameter bifurcation diagram of the travelling wave equations HB the curve of Hopf bifurcation points, HC branches of homoclinic orbits

begins and ends at the saddle point. The spiral path of the branch of homoclinic orbit is a result of the spiral nature of the trajectory in the neighbourhood of the saddle focus.

Next we examine the lower part of homoclinic orbit branch C using the magnified view presented in Figure 3.8. As the speed of travelling wave decreases, folds in the homoclinic branch C occur before the branch intersects a curve of Hopf bifurcation points. Balmforth *et al* [5] have shown that the resulting oscillations in the branch of homoclinic orbits correspond to homoclinic orbits that make multiple loops around one of the other steady states before returning to the starting point. Just such an orbit is presented in Figure 3.9, which is taken from branch C at a point near where the branch intersects the locus of Hopf points. For comparison Figure 3.10 shows a homoclinic orbit from branch C before the branch starts to fold. This orbit goes once around another steady state before returning to the rest.

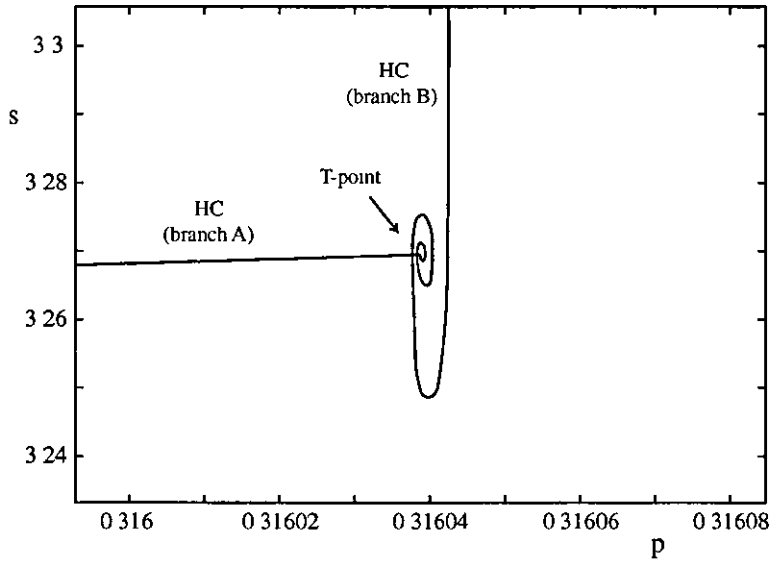


Figure 3.6 Magnified view of the upper part of Figure 3.5 where homoclinic branch A connects to homoclinic branch B at a T-point

This form of bifurcation structure has also been observed by Sneyd *et al* [154] in a numerical analysis of travelling waves in a model of pancreatic acinar cells. We briefly present the main physiology of their model. The model of Sneyd *et al* assumes that there are two different shut states, S and \tilde{S} , and Ca^{2+} regulates the interconversion of the receptor between these two states. Similarly, there are two open, O and \tilde{O} , and two inactivated states, I_1 and \tilde{I}_1 . Their model of an IP_3R is based on the binding diagram shown in Figure 3.11, where p and c denote IP_3 and Ca^{2+} concentrations respectively. Since IP_3 can bind to either shut state, and convert it to an open state, the concentration of Ca^{2+} will determine the rate at which receptors are opened by IP_3 . In a similar fashion, $[\text{Ca}^{2+}]$ controls the rate of receptor inactivation, and the rate of recovery from inactivation. By using a standard assumption that opening of the receptor by IP_3 binding is a fast process compared to receptor inactivation and recovery from inactivation, the model of Sneyd *et al* reduces to two equations. Similar to the Li-Rinzel reduced DYK model, one equation expresses conservation of calcium in the cytoplasm, and the other describes the gating dynamics of the

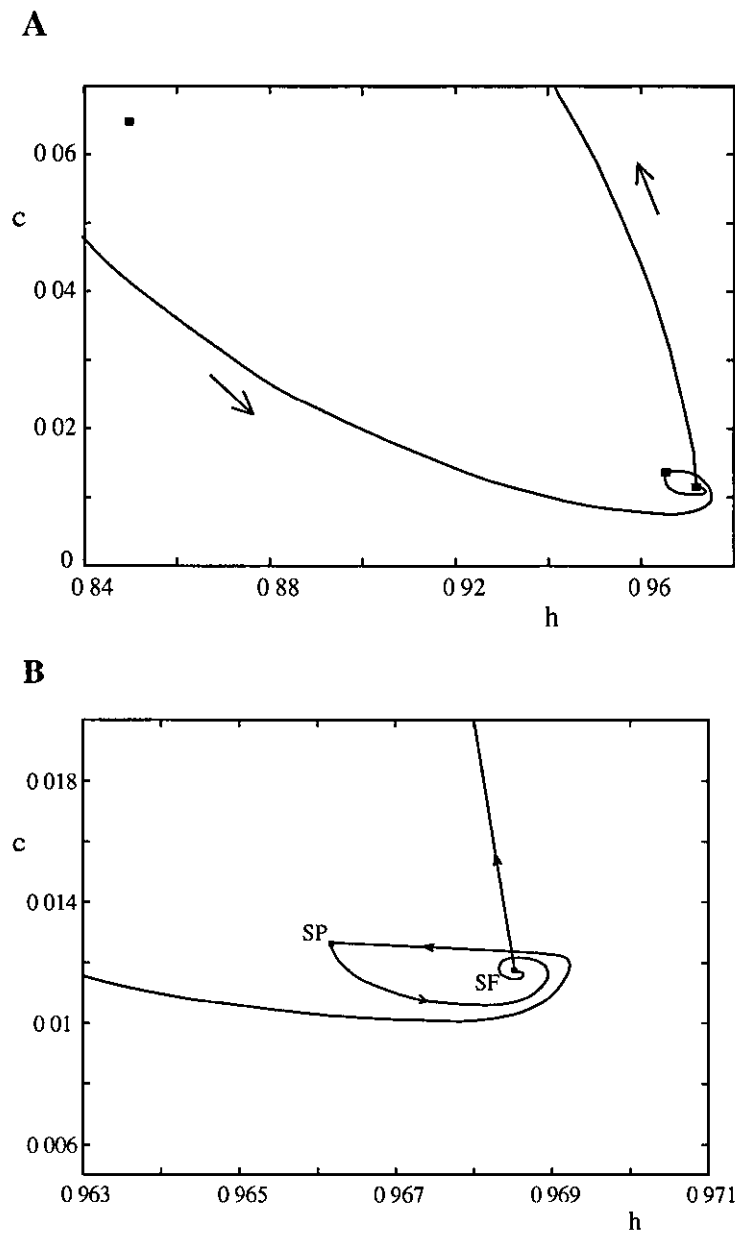


Figure 3.7 The heteroclinic cycle at the T-point (A) the whole cycle, (B) magnified view of the cycle SP. saddle point, SF saddle focus

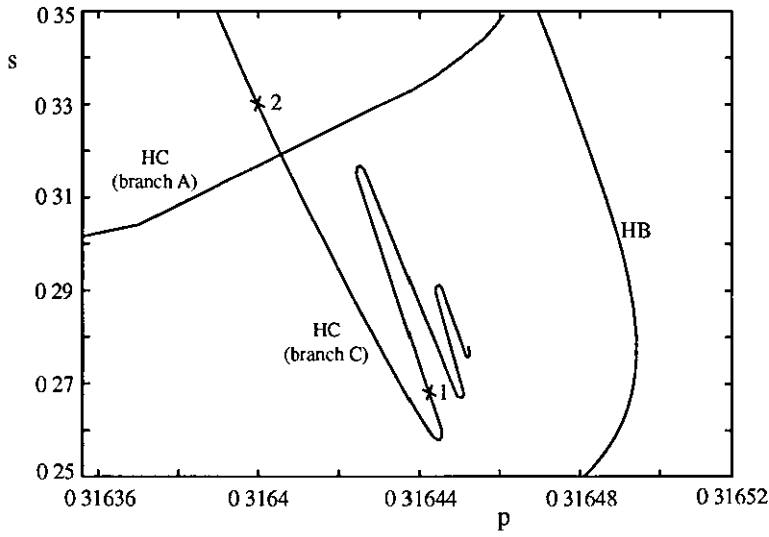


Figure 3.8 Magnified view of the lower part of homoclinic branch C, showing the folding of the branch as it approaches a locus of Hopf bifurcation points

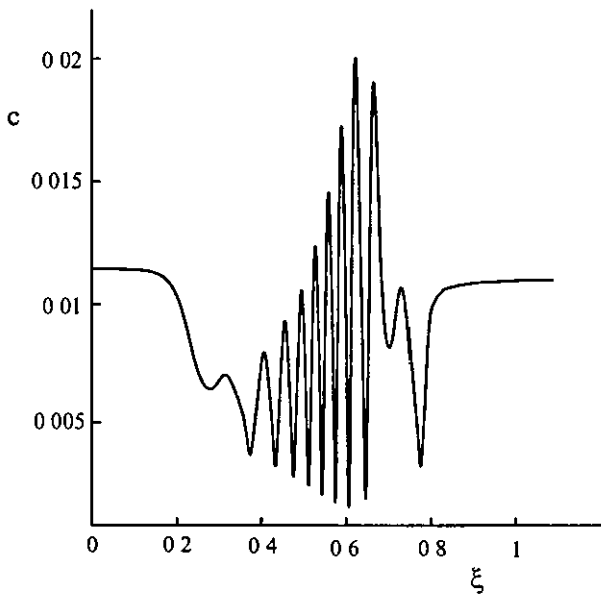


Figure 3.9 A homoclinic orbit from the marked point 1 in Figure 3.8

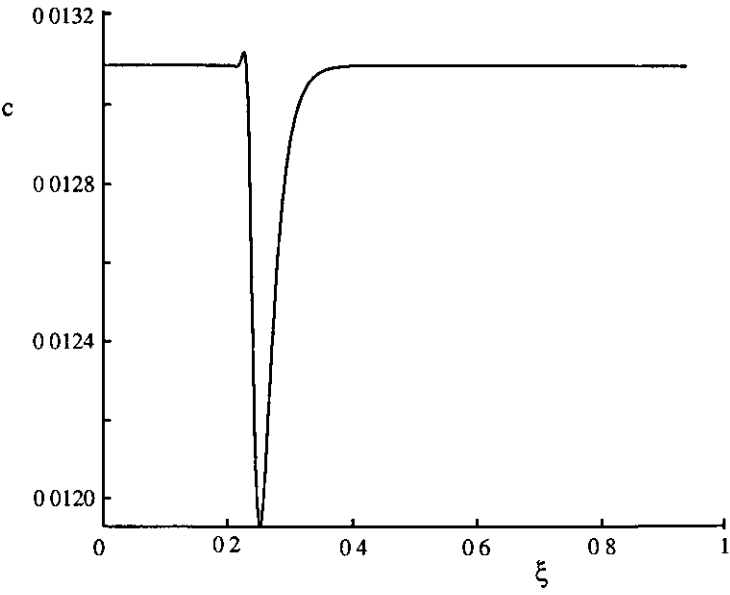


Figure 3 10 A homoclinic orbit from the marked point 2 in Figure 3 8

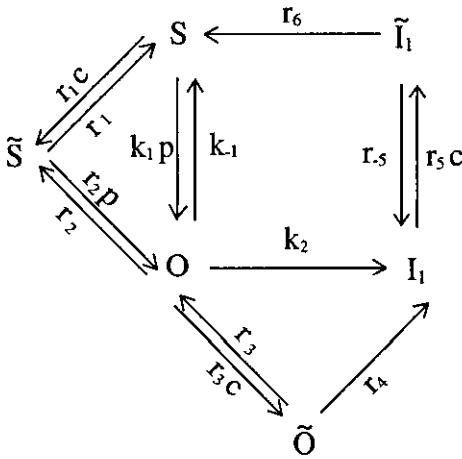


Figure 3 11: A schematic diagram of the full receptor model of Sneyd et al [154]

IP₃R The concentration of Ca²⁺ is affected by diffusion, IP₃Rs, calcium pumps, and leakage, i.e.

$$\partial_t c = D \partial_x^2 c + J_r(c, h, p) - J_p(c) + J_l, \quad (3.28)$$

with the diffusion coefficient D ; $J_r(c, h, p)$ denotes the influx through IP₃Rs, $J_p(c)$ the ATPase-driven Ca²⁺ flow from the cytoplasm to the ER (SERCA pumps) as in the DYK model (see equation (2.16)), and J_l indicates the constant calcium leaking into the cell. The variable $h = h(x, t)$ in the model of Sneyd *et al* represents the fraction of the IP₃Rs that are active. The portion of active IP₃Rs varies according to

$$\partial_t h = \phi_3(c)(1 - h) - \frac{\phi_1(c)\phi_2(c)p}{\phi_1(c)p + \phi_{-1}(c)}, \quad (3.29)$$

where

$$\phi_1(c) = \frac{r_2 c}{R_1 + c}, \quad \phi_{-1}(c) = \frac{k_{-1} R_3}{R_3 + c}, \quad (3.30)$$

$$\phi_2(c) = \frac{k_2 R_3 + r_4 c}{R_3 + c}, \quad \phi_3(c) = \frac{k_3 R_5}{R_5 + c} \quad (3.31)$$

and $R_i = r_{-i}/r_i$ for $i = 1, 3, 5$. Their model assumes that the IP₃R is made up of four independent, identical subunits and can only release calcium when all four of its subunits are open. Thus the influx of calcium is proportional to the probability that each of four subunits are open

$$J_r(c, h, p) = k_f \left(\frac{ph\phi_1(c)}{\phi_1(c)p + \phi_{-1}(c)} \right)^4 \quad (3.32)$$

Although the structure of IP₃R differs to the one in the DYK model, the Sneyd *et al* model possesses a qualitatively similar bifurcation structure. Sneyd *et al* have discussed the bifurcation diagram in some detail, although without an explicit determination of wave stability. We further develop their arguments and determine the stability of numerically constructed solution branches in the DYK model using linear stability analysis. Our results are consistent with the recent paper of Romeo and

Jones [135], who investigate the stability of travelling pulse solutions in the Sneyd *et al* model of pancreatic acinar cells [154] Note that our stability analysis in [165] pre-dates that of Romeo and Jones [135]

3.2.2 Stability

Linearisation of (3.23) and (3.24) around a stationary (travelling wave) solution $(c_0(\xi), h_0(\xi))$ and considering small perturbations of type $(r(\xi, t), s(\xi, t)) \propto (r(\xi), s(\xi)) \exp(\lambda t)$ yields an eigenvalue problem given by

$$\mathcal{M} \begin{bmatrix} r(\xi) \\ s(\xi) \end{bmatrix} = \lambda \begin{bmatrix} r(\xi) \\ s(\xi) \end{bmatrix}, \quad \mathcal{M} = \begin{bmatrix} D\partial_\xi^2 + s\partial_\xi + A_1(\xi) & A_2(\xi) \\ B_1(\xi) & s\partial_\xi + B_2(\xi) \end{bmatrix}, \quad (3.33)$$

where

$$\begin{aligned} A_1(\xi) &= \partial_c f_1(c_0(\xi), h_0(\xi)), & A_2(\xi) &= \partial_h f_1(c_0(\xi), h_0(\xi)), \\ B_1(\xi) &= \partial_c f_2(c_0(\xi), h_0(\xi)), & B_2(\xi) &= \partial_h f_2(c_0(\xi), h_0(\xi)) \end{aligned}$$

The linear stability of a travelling wave is then determined by an examination of the spectrum of the Jacobian \mathcal{M} in (3.33). The eigenvalues associated with perturbations around the homogeneous steady state (giving the essential spectrum) can easily be found by substituting solutions of the form $u(\xi, t) = \exp(\lambda t + ik\xi)u_0$ into the linear equation $u_t = \mathcal{M}u$. Hence, the continuous spectrum of \mathcal{M} is defined by a characteristic polynomial of the form $\det[M(k) - \lambda I] = 0$, where

$$\mathcal{M}(k) = \begin{bmatrix} -Dk^2 + isk + A_1 & A_2 \\ B_1 & isk + B_2 \end{bmatrix} \quad (3.34)$$

Here A_1, A_2, B_1 and B_2 are the forms taken by $A_1(\xi), A_2(\xi), B_1(\xi)$ and $B_2(\xi)$ when $(c_0(\xi), h_0(\xi)) = (\bar{c}, \bar{h})$ is a homogeneous steady state. Assuming that $\text{Re}(\lambda) = \alpha$ and $\text{Im}(\lambda) = \beta$, gives us the following system for the continuous spectrum

$$\begin{aligned} -DB_2k^2 + Dk^2\alpha - s^2k^2 + 2sk\beta + A_1B_2 - (A_1 + B_2)\alpha + \alpha^2 - \beta^2 - A_2B_1 &= 0 \\ -Dsk^3 + Dk^2\beta + sB_2k - 2sk\alpha + sA_1k - (A_1 + B_2)\beta + 2\alpha\beta &= 0, \end{aligned}$$

which may be solved simultaneously to give the pair $(\alpha(k), \beta(k))$. To find the full spectrum of the linearised system it remains to determine the point spectrum of \mathcal{M} . In particular the eigenvalue spectrum of a single pulse in an infinite system contains a continuous part which can be identified with the spectrum of the stable rest state, as well as a discrete part related to eigenfunctions localised near the pulse solution.

Since, in general, solutions $c_0(\xi)$, $h_0(\xi)$ and the eigenfunctions of the Jacobian \mathcal{M} are not available in closed form, the eigenspectrum of \mathcal{M} has to be determined numerically. We have used Fourier spectral methods on a bounded domain with a discretization of $N = 2^8$ points to do precisely this. A brief description of these methods is given in Appendix A.3 and a more detailed discussion may be found in [166] and [170]. The zero eigenvalue, which always exists due to the translational symmetry of the problem, is used as a numerical accuracy check and has been obtained with a precision of 10^{-4} . Figure 3.12 shows the eigenspectrum for travelling pulse solutions on the upper and lower part of homoclinic branch A in Figure 3.5. We see that, in both cases, the continuous spectrum lies completely in the left complex half-plane. The discrete spectrum for the solution on the upper branch remains in the left half-plane. However, the discrete spectrum for the solution on the lower branch crosses the imaginary axis and has an isolated eigenvalue in the right half-plane. Hence, we conclude that of the two possible coexisting solitary pulses it is the faster one that is stable.

3.2.3 A kinematic theory of spike trains

By treating the period of oscillations as a parameter it is also possible to construct dispersion curves showing the speed of a wave as a function of its period. In Figure 3.13 we present a typical dispersion curve, $s = s(\Delta)$, for a periodic orbit. A numerical calculation of the eigenspectrum of \mathcal{M} shows that it is the faster of the two branches that is stable. Knowledge of dispersion curves opens the way for the development of

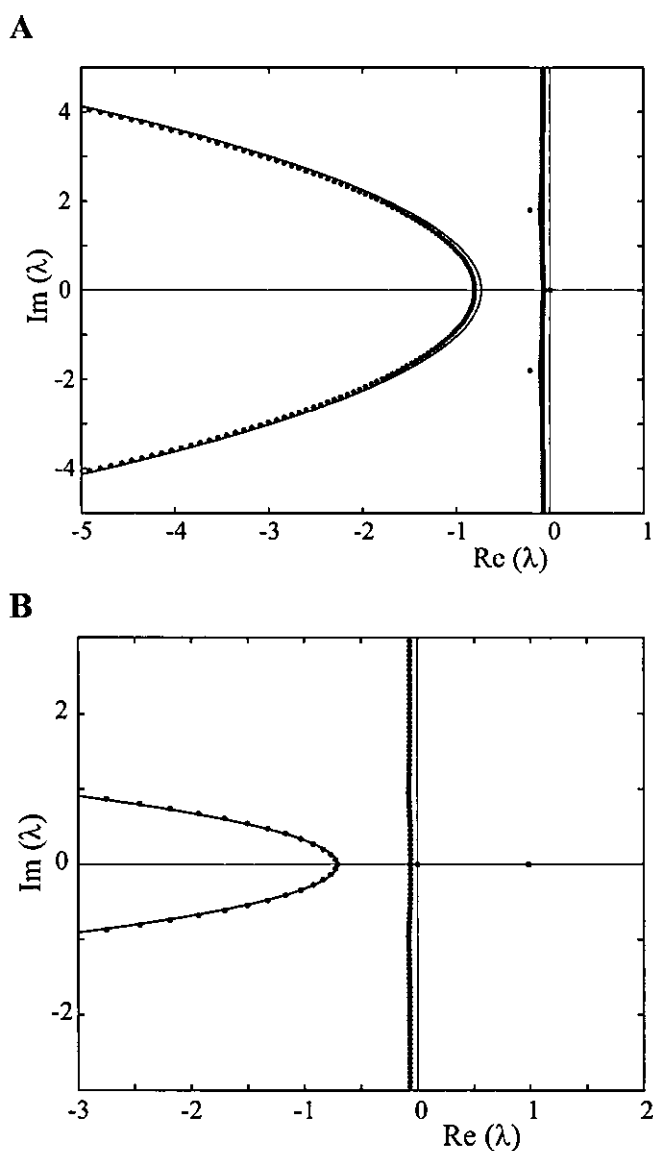


Figure 3.12 (A) Eigenvalues of the linearised system in the complex plane for the pulse solution at $p = 0.2363$ and $s = 2$ (B) Eigenspectrum at $p = 0.2408$ and $s = 0.6$ The solid lines correspond to the analytically obtained continuous spectrum at the same parameter values

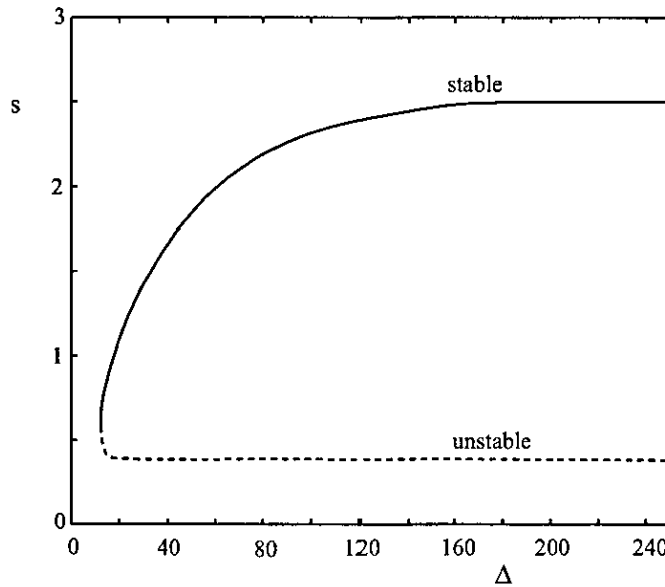


Figure 3.13 The dispersion curve for periodic travelling waves when $p = 0.2622$

a *kinematic* theory of irregular wave propagation that attempts to follow irregularly spaced spikes of activity [132]. Miller and Rinzer [113] considered impulse propagation along the Hodgkin-Huxley cable equations [71] using numerical experiments and deduced that the kinematic approximation provides a reasonable estimate for the variation in interspike intervals and the influence of dispersion during propagation. Using their approach the dynamics of Ca^{2+} spikes are considered to evolve according to

$$\frac{dT^n}{dx} = \frac{1}{s(\Delta^n)}, \quad \Delta^n(x) = T^n(x) - T^{n-1}(x), \quad (3.35)$$

where $s(\cdot)$ is the velocity as a function of interspike interval given by the dispersion relation for periodic wave trains. The time at which the n th spike occurs at position x is defined in terms of a threshold parameter c_{th} as

$$T^n(x) = \inf \left\{ t \mid c(x, t) \geq c_{\text{th}}, \frac{\partial c(x, t)}{\partial t} > 0, t \geq T^{n-1}(x) \right\} \quad (3.36)$$

We shall call $\Delta^n(x)$ the instantaneous interspike interval (ISI), as it measures the time between spikes of activity at position x . When the instantaneous ISI is constant, we

recover a singly periodic wave. Importantly, this framework is ideally suited for the analysis of irregular spike trains.

For linear stability analysis we consider local perturbations of the firing times as $T^n(x) \rightarrow T^n(x) + g^n(x)$. A general propagating wavetrain is stable if under the perturbation the system converges to the unperturbed solution during propagation (i.e., $g^n(x) \rightarrow 0$ as $x \rightarrow \infty$). Inserting the perturbed solution in (3.35) gives

$$\frac{dg^n(x)}{dx} = -\frac{s'(\Delta^n)}{s^2(\Delta^n)}[g^n(x) - g^{n-1}(x)]. \quad (3.37)$$

Thus, a linear stability analysis of the kinematic equations shows that solutions are stable if $s'(\Delta^n) > 0$ for all n . For a periodic orbit with $\Delta^n = \Delta$ for all n the stability predictions of the kinematic theory (solutions are stable if $s'(\Delta) > 0$, i.e. on the upper branch) are in complete agreement with those obtained from the eigenspectrum of \mathcal{M} . Interestingly it has been shown that when the stable branch of the dispersion curve has an exponential shape then there are solutions to the kinematic equations that describe stable connections to periodic orbits [35]. This form of wave may also be regarded as a travelling front in the ISIs such that $\Delta^n(x) = \Delta(\kappa x - \omega n)$ for some κ and ω where $\Delta(\cdot)$ has a sigmoidal shape. To confirm this prediction we perform a direct numerical simulation of the DYK model. Since we are looking for a travelling front in the instantaneous ISIs we choose initial data (at one end of a cell of length L) with a spike train that has a step change in the interspike intervals (changing from $\Delta_{(1)}$ to $\Delta_{(2)}$ after n^* ISIs of $\Delta_{(1)}$) given by

$$I(t) = \sum_0^{n^*} P(t - n\Delta_{(1)}) + \sum_{n=n^*+1}^{\infty} P(t - n^*\Delta_{(1)} - (n - n^*)\Delta_{(2)}) \quad (3.38)$$

with general rectangular stimulus of the form $I(t) = \sum_n P(t - T^n(0))$ with $P(t) = I_0\theta(t)\theta(\tau_d - t)$, where I_0 is the magnitude of an applied pulse, τ_d its duration and $\theta(x)$ is a step function with $\theta(x) = 1$ for $x \geq 0$ and is zero for $x < 0$.

Figure 3.14 gives an illustration of this signal. An example of direct numerical simulation is shown in Figure 3.15. We can see a transition from period $\Delta_{(1)}$ to $\Delta_{(2)}$ as

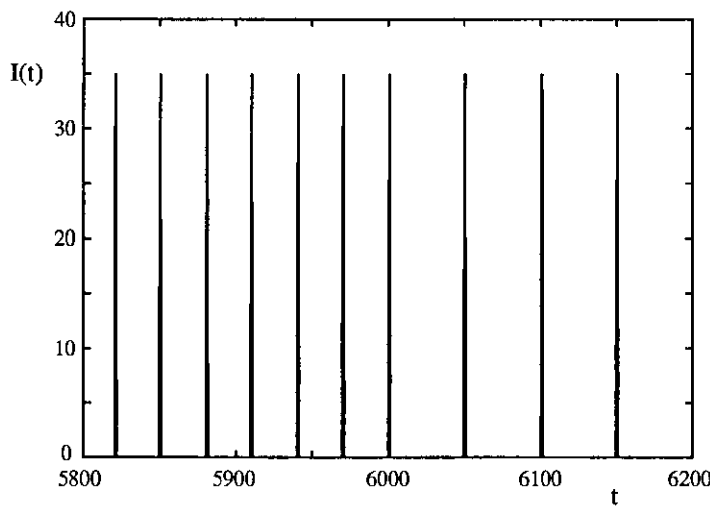


Figure 3.14: A stimulus signal $I(t)$ for a connection between orbits with differing instantaneous ISIs. The following parameters are used: $I_0 = 35$, $\tau_d = 1$, $L = 200$, $\Delta_{(1)} = 30$, $\Delta_{(2)} = 50$, $n^* = 200$.

time increases. Another way to visualise these connections between periodic orbits is to plot the ISIs at various values of x as a function of the number of spiking events at those positions, as shown in Figure 3.16 (where we have used values of $\Delta_{(1)}$ to $\Delta_{(2)}$ that best illustrate the sigmoidal nature of the front). Here, it is clearly seen that the step change can smooth out to form a transition layer of the form predicted by the kinematic theory.

3.2.4 Period doubling bifurcations

Using direct numerical simulations Sneyd *et al* [154] also show that secondary waves and irregular travelling wave behaviour can arise near the point where homoclinic branch A disappears at a T-point. Such waves are also expected in the DYK model. Sneyd *et al* conclude that homoclinic branch A is the one that generates physiologically significant travelling waves. Our stability analysis would also suggest that one may restrict attention to the faster branch. However, when broadening the discussion

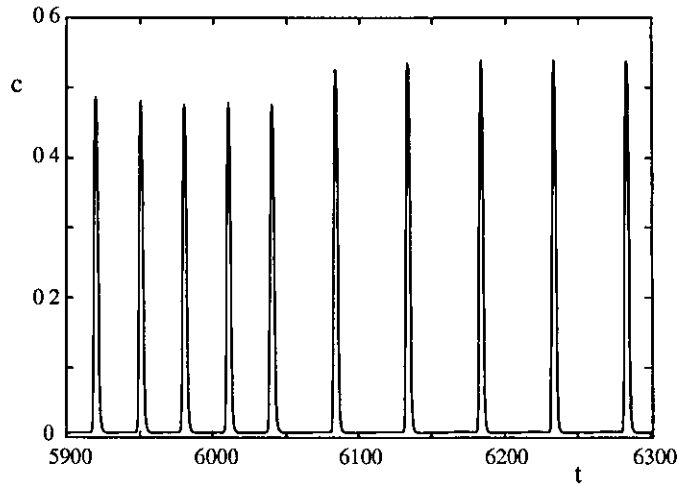


Figure 3.15 Stimulation of a cell of length $L = 200$ and $p = 0.26$ with a spike train input at $x = 0$ with instantaneous ISI changing from $\Delta_{(1)} = 30$ to $\Delta_{(2)} = 50$ after 200 spikes. Dynamics of Ca^{2+} is shown at a position of $3L/4$ from the point of stimulation, showing a connection between periodic orbits with ISI $\Delta_{(1)}$ and $\Delta_{(2)}$.

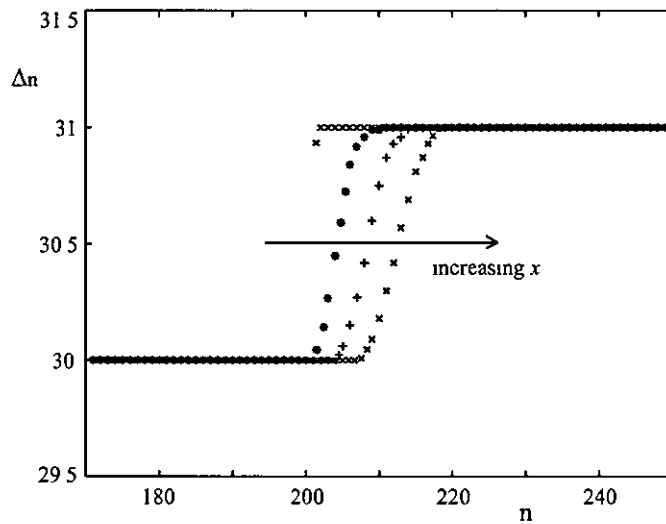


Figure 3.16. Travelling front in the ISIs, showing a connection between periodic orbits. Initial data is in the form of a spike train with a step in the ISIs after 200 spikes from $\Delta_{(1)} = 30$ to $\Delta_{(2)} = 31$. Here, $p = 0.26$ and $c_{th} = 0.3$. Data is represented at the following positions $0, L/4, L/2$ and $3L/4$, with $L = 200$.

of waves to cover periodic travelling waves it is possible that there are other interesting bifurcation structures present. With this in mind we turn our attention to period doubling bifurcations of the orbits arising at Hopf bifurcation points in Figure 3.3

We have found that it is possible for period doubling bifurcations to occur for slow waves arising when branches of periodic orbits connect to each other as in Figure 3.17. In this figure, period doubling points of a primary periodic orbit are labelled PD1, period doublings of secondary orbits as PD2 etc. Orbits of type PD2 and PD4 are destroyed in global homoclinic bifurcations in favour of homoclinic orbits which we denote as HC2 and HC4. Figure 3.18 (A, B and C) demonstrates typical examples of double periodic orbit and double homoclinic orbit as well as 4-periodic solution. It is likely that there exists a family of $2n$ -periodic orbits which arise from n -periodic orbits (through period doublings) and end in $2n$ -homoclinic bifurcations.

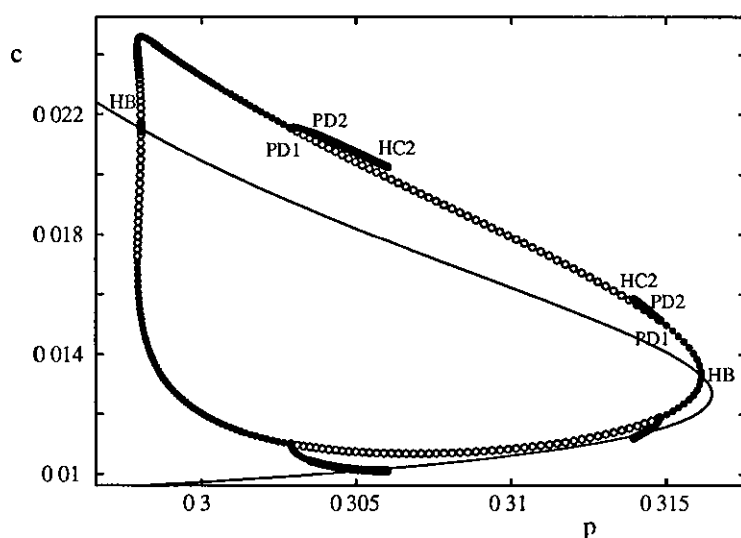


Figure 3.17. *Bifurcation diagram of the reduced DYK model for $s = 0.2$ and $D = 1$ showing period doubling bifurcations. HB Hopf bifurcation, PD n period-doubling of an n -periodic orbits, HC2 homoclinic bifurcation to a doubly periodic orbit*

In Figure 3.19 we show the branches of 2- and 4-homoclinic orbits HC2 and HC4

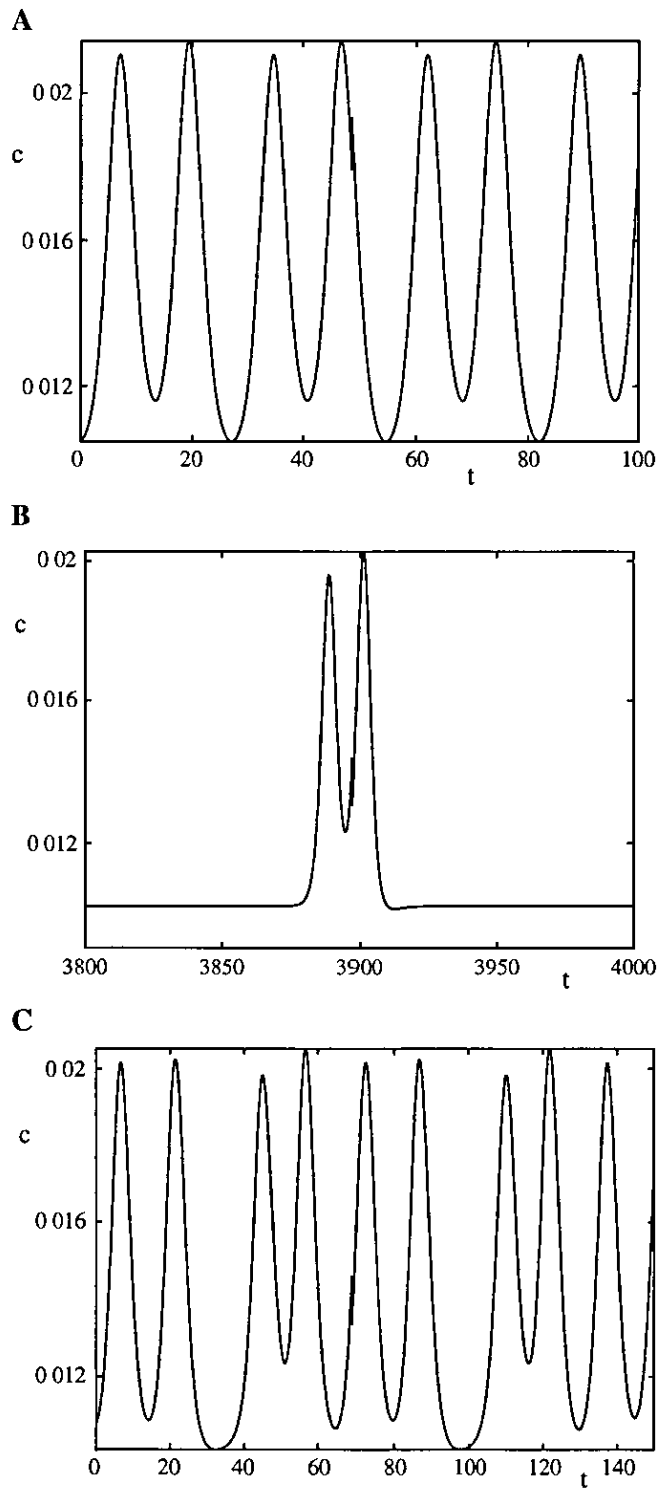


Figure 3.18 Examples of (A) double periodic orbit for $p = 0.3034$, (B) double homoclinic orbit for $p = 0.306$ and (C) 4-periodic orbit for $p = 0.3055$ and $s = 0.2$

together with the lower part of homoclinic branch A. This figure suggests the possibility of a homoclinic-doubling cascade arising from the unstable solitary pulse of branch A. Since, however, these bifurcations are those of an unstable wave they are not expected to be physiologically significant.

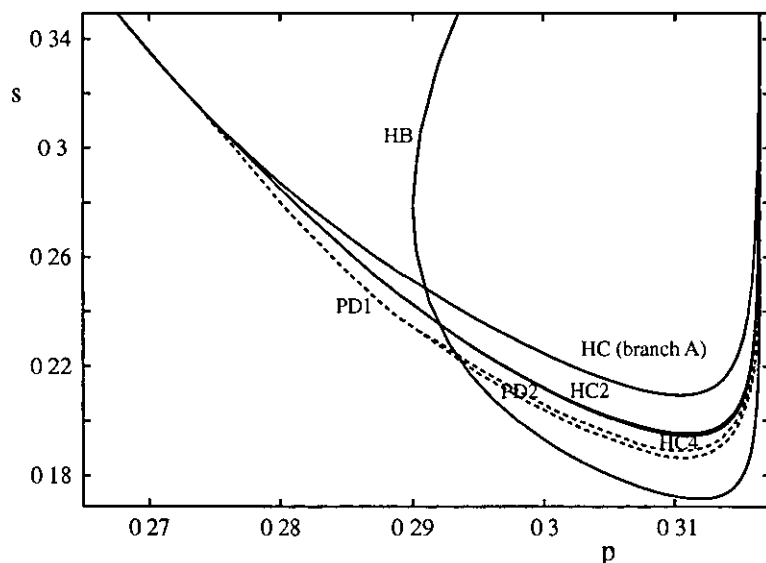


Figure 3.19 Two parameter bifurcation diagram of the travelling wave equations showing homoclinic-doubling cascade. HC_n branches of n -homoclinic orbits; HB Hopf bifurcation, PD_n period-doubling bifurcation curves of n -periodic orbits (dashed curves)

Summary

In this chapter we have presented a detailed numerical bifurcation analysis of travelling waves in the reduced DYK model of calcium release. The linear stability of these waves has been found by numerically solving an appropriate eigenvalue problem. A by-product of this investigation is the observation that this model has qualitatively the same dynamics as the recently introduced two-state model of IP_3 receptor dynamics for pancreatic acinar cells [154]. We have also presented a kinematic theory of wave propagation based around numerically computed dispersion curves for periodic

waves. We have used this to predict the existence of a non-periodic wave that may be regarded as a travelling front that connects two different periodic orbits. Direct numerical simulation of the DYK model has confirmed this prediction.

Chapter 4

The continuum Fire-Diffuse-Fire model

The analysis of travelling waves, even in reduced DYK model presented in the previous chapter, is typically only possible with the use of numerical bifurcation techniques. In this chapter we introduce a much simpler FDF type model which provides an idealised model of Ca^{2+} release within living cells. This model was originally intended as a model of cardiac myocytes in which calcium release occurs via RyR Ca^{2+} channels located in a regular array in the SR [88]. The discreteness of release sites leads to a wave of increased Ca^{2+} concentration that travels with a lurching quality (saltatory propagation). However, one of the major successes of the FDF model is that it can be analysed both in the discrete and continuous limits. This chapter is concerned with the continuum description where waves propagate with a constant profile. Saltatory waves will be considered in Chapter 5.

We generalise the original FDF model to incorporate dependence on IP_3 concentration and also refractoriness of release sites. This allows a direct comparison between numerically obtained properties of the DYK model in Chapter 3 and new exact analytical results for travelling waves in the FDF model. We demonstrate that travelling wave solutions of the continuum FDF model exhibit many qualitative and quanti-

tative features of the waves we have described for the DYK model under parameter variation

4.1 The Fire-Diffuse-Fire model

The propagation of Ca^{2+} waves in cardiac myocytes are often along the longitudinal axis where Ca^{2+} release sites are aligned in regular arrays with a characteristic separation of $\sim 2\mu\text{m}$. This structure of cardiac myocytes is amenable to modelling and leads to an idealised model of spark-mediated Ca^{2+} waves (FDF model), originally introduced by Keizer *et al* [88]. They suggested a simplified model of Ca^{2+} release that mimics the properties of CICR from isolated sites to explore the nature of saltatory wave propagation. In this model a site releases Ca^{2+} instantaneously ("fires") when the value of $[\text{Ca}^{2+}]$ at the site exceeds a threshold value. To mimic a long-lasting *refractory* state, once a site has released Ca^{2+} , it can no longer fire again. The release sites are located with a fixed separation d and Ca^{2+} released at one site diffuses continuously with an *effective* diffusion constant D , due to the presence of myoplasmic buffers. The original FDF model was described by the single-evolution equation

$$\frac{\partial u}{\partial t} = D \frac{\partial^2 u}{\partial x^2} + \frac{\sigma}{\tau_R} \sum_i \delta(x - x_i) \Theta(t - t_i) \Theta(t_i + \tau_R - t), \quad (4.1)$$

where $u(x, t)$ is the average concentration of calcium, δ is the Dirac delta function, $\Theta(\cdot)$ is the Heaviside step function ($\Theta(t) = 0$ for $t < 0$, $\Theta(t) = 1$ for $t \geq 0$), t_i is the first time at which the i th site takes on the threshold value, σ is the source amplitude and τ_R is the "rise time" for the receptor (*i.e.*, the length of time the receptor is open during a release event). In contrast to the kinetic biophysical models, the FDF model leads to analytical expressions for the wave shape and the wave speed. Moreover, this model reproduces the full range of wave propagation, from saltatory to continuous, whereas homogeneous reaction diffusion models predict only continuous propagation. We illustrate this in Figure 4.1 where we show the propagation of continuous and

saltatory Ca^{2+} signals in the original FDF model. In panel A, the time constant for Ca^{2+} release $\tau_R = 1$ s and the propagating signal is a travelling front. Panel B presents a simulation using $\tau_R = 10 \mu\text{s}$ where spark-like Ca^{2+} release leads to a propagating signal that is distinctly saltatory. In this model the speed of the wave front is determined by the time it takes Ca^{2+} released by the site at the front to diffuse to the next active site and raise the value of $[\text{Ca}^{2+}]$ there to the threshold. Note, that the continuous wave travels at $\sim 11.3 \mu\text{m/s}$ while the saltatory wave travels at $\sim 67 \mu\text{m/s}$. The long duration of Ca^{2+} release in the continuous case appears to slow the velocity of the propagating signal. The works of Keizer *et al* [88] and other researchers [44, 126, 127] give a simple criterion for distinguishing saltatory and continuous propagation modes. When $D\tau_R/d^2 \ll 1$, propagation is saltatory and the wave speed is proportional to D . In the saltatory limit, propagation consists of isolated bursts of Ca^{2+} that occur as each consecutive site fires. When $D\tau_R/d^2 \gg 1$, propagation is continuous, the velocity is proportional to \sqrt{D} , and many sites are releasing Ca^{2+} simultaneously. The effect of Ca^{2+} pumps, which re-sequester the ions back into the stores was neglected in these studies (assuming that the pumps operate on a very slow time-scale). The analysis of the FDF model was extended later by Coombes [34] to include linear SERCA pumps.

Here we generalise the FDF model to include multiple Ca^{2+} release events for describing more realistic travelling Ca^{2+} waves. The generalised version of the model sustains both solitary and periodic travelling wave propagation. The Ca^{2+} signal is generated by the mechanism of CICR, *i.e.* the receptor channel is activated at low cytosolic Ca^{2+} levels and inhibited at high cytosolic Ca^{2+} levels. Thus, for low Ca^{2+} levels, an increase in Ca^{2+} stimulates a further increase. At higher levels the receptor inactivates and cannot reopen for some time during which it is in a *refractory* state. Thus, the release of Ca^{2+} by intracellular stores is self-regulating. The release events (Ca^{2+} *puffs* or *sparks*) lead to the propagation of travelling waves via diffusion of Ca^{2+} . The model incorporates descriptions of the two major fluxes between the ER

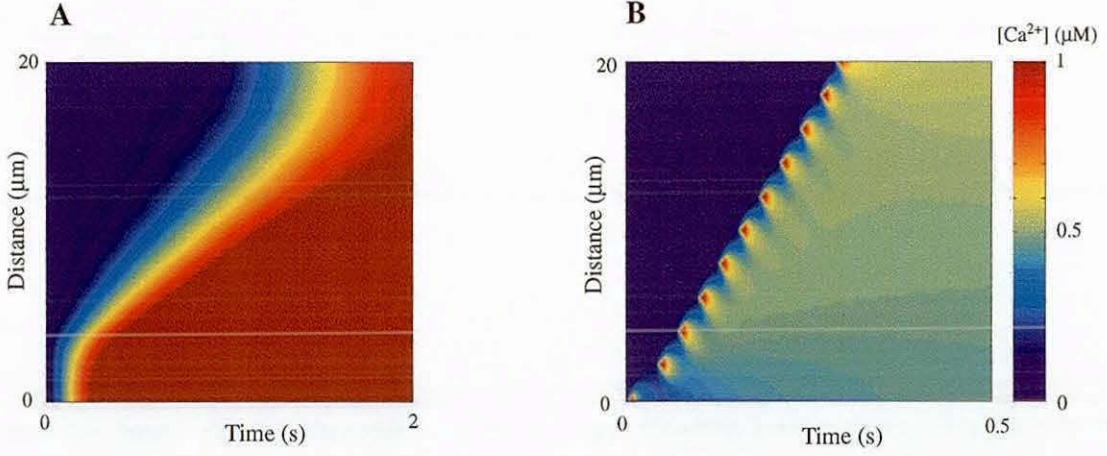


Figure 4.1: *Continuous (A) and saltatory (B) travelling wave propagations for the following parameters: $D = 30 \mu\text{m}^2/\text{s}$, $d = 2 \mu\text{m}$, $\sigma = 5 \mu\text{M} \cdot \mu\text{m}$, $u_{th} = 0.1 \mu\text{M}$ and $\tau_R = 1 \text{ s}$ for panel A and $10 \mu\text{s}$ for panel B.*

and the cytosol. The first is due to a pump which drives the Ca^{2+} up the gradient from the cytosol back into the ER and the second arises when the Ca^{2+} channel opens and causes a large flux from the ER into the cytosol. Denoting the concentration of Ca^{2+} ions by $u(x, t)$, the generalised FDF model is given by the following partial differential equation

$$\frac{\partial u}{\partial t} = -\frac{u}{\tau_d} + D \frac{\partial^2 u}{\partial x^2} + \rho(x) \sum_m \eta(t - T^m(x)), \quad x \in \mathbb{R}, \quad t > 0. \quad (4.2)$$

The decay time τ_d describes the action of the Ca^{2+} pumps that resequence the Ca^{2+} back into the stores. Note that in comparison to the DYK model, the model of a pump is linear and is one of the reasons why the generalised FDF model is mathematically tractable. The other reason is that there is no explicit inclusion of a receptor dynamics. Rather, Ca^{2+} puffs are triggered from the release site at position x at times $T^m(x)$, $m \in \mathbb{Z}$. These release times are defined in terms of a threshold process according to

$$T^m(x) = \inf \left\{ t \mid u(x, t) > h, \frac{\partial u(x, t)}{\partial t} > 0; t \geq T^{m-1}(x) \right\}. \quad (4.3)$$

However, as it stands the FDF model ignores the significantly important process of being in a refractory state and cannot therefore be sensibly used to understand periodic travelling waves. It is of course perfectly satisfactory when studying solitary waves, since single release events are not affected by refractoriness. To remedy this lack of refractoriness we introduce a time dependent threshold. The idea is to mimic refractoriness, whilst retaining analytical tractability, with a threshold which is high just after a release event but gradually decays back to some more normal level. Such a process may be written

$$h = \frac{u_{th} - h}{\tau} + \gamma \sum_m \delta(t - T^m(x)), \quad \text{with initial data } h(0) = u_{th}, \quad (4.4)$$

where τ determines the refractory time-scale and γ is some large positive constant. Using this scheme h decays towards a constant threshold u_{th} at a rate τ^{-1} and $h \rightarrow \gamma h$, whenever a Ca^{2+} puff is triggered. The function $\eta(t)$ describes the shape of the puff and is often considered to be a simple rectangle

$$\eta(t) = \frac{\sigma}{\tau_R} \Theta(t) \Theta(\tau_R - t), \quad (4.5)$$

where $\Theta(\cdot)$ is a step function, σ is the strength of the puff and τ_R its duration. For a simple continuum model we consider the density distribution of the calcium sources $\rho(x) = 1$ (the discrete FDF model is discussed in Chapter 5)

4.2 Solitary travelling pulse

Before discussing periodic travelling waves we first review some properties of solitary wave propagation in the continuum FDF model [34]. Solitary travelling waves may be described in the form $T^0(x) = x/s$, where s denotes the speed of the wave. Assuming $u(x, t) = u(\xi)$, where $\xi = st - x$, gives the following travelling wave ODE

$$Du_{\xi\xi} - su_{\xi} - \frac{u}{\tau_d} = -\frac{\sigma}{\tau_R} \Theta(\xi) \Theta(s\tau_R - \xi), \quad (4.6)$$

where $u_\xi \equiv du/d\xi$. For travelling pulse solutions which satisfy $\lim_{\xi \rightarrow \pm\infty} u(\xi) = 0$ the solution to (4.6) takes the form

$$u(\xi) = \begin{cases} \alpha_1 e^{\lambda_+ \xi} & -\infty < \xi < 0 \\ \alpha_2 e^{\lambda_+ \xi} + \alpha_3 e^{\lambda_- \xi} + \tau_d \sigma / \tau_R & 0 < \xi < s\tau_R \\ \alpha_4 e^{\lambda_- \xi} & \xi > s\tau_R \end{cases} \quad (4.7)$$

with

$$\lambda_{\pm} = \frac{1}{2D} \left[s \pm \sqrt{s^2 + 4D/\tau_d} \right] \quad (4.8)$$

By ensuring the continuity of the solution and its first derivative at $\xi = 0$ and $\xi = s\tau_R$ the unknown coefficients $\alpha_1, \dots, \alpha_4$ may be found as follows

$$\alpha_1 = \alpha_3 \frac{\lambda_-}{\lambda_+} [1 - e^{-\lambda_+ s\tau_R}] \quad (4.9)$$

$$\alpha_2 = -\alpha_3 \frac{\lambda_-}{\lambda_+} e^{-\lambda_+ s\tau_R} \quad (4.10)$$

$$\alpha_3 = \frac{\tau_d \sigma}{\tau_R} \frac{\lambda_+}{\lambda_- - \lambda_+} \quad (4.11)$$

$$\alpha_4 = \alpha_3 [1 - e^{-\lambda_- s\tau_R}] \quad (4.12)$$

The self-consistent speed of the travelling pulse can be found by demanding that $u(x, T(x)) = u_{th}$, i.e. in the travelling frame system $u(0) = u_{th}$. This gives from (4.7) that the speed of a travelling pulse satisfies the implicit equation

$$u_c = \frac{\lambda_-}{\lambda_- - \lambda_+} [1 - e^{-\lambda_+ s\tau_R}], \quad (4.13)$$

where $u_c = u_{th} \tau_R / \sigma \tau_d$. It is straightforward to show from (4.13) that the speed of the wave scales with the square-root of the diffusion coefficient [34]. Figure 4.2 demonstrates the speed of the constant profile travelling pulse as a function of the dimensionless threshold parameter $u_c = u_{th} \tau_R / \sigma \tau_d$. The two waves coalesce at a LP and propagation failure can result for too large a choice of the threshold parameter. Figures 4.3 and 4.4 demonstrate exactly this. When we are in the parameter regime

to the left of the LP, solitary travelling wave in the model propagates through the whole cell (Figure 4.3). To the right of the LP, travelling pulses fail to propagate and we observe an abortive wave (Figure 4.4). Figure 4.5 demonstrates a numerical continuation of the LP in Figure 4.2. This figure specifies the area of parameters in the (u_c, τ_R^{-1}) plane where stable travelling pulse exists.

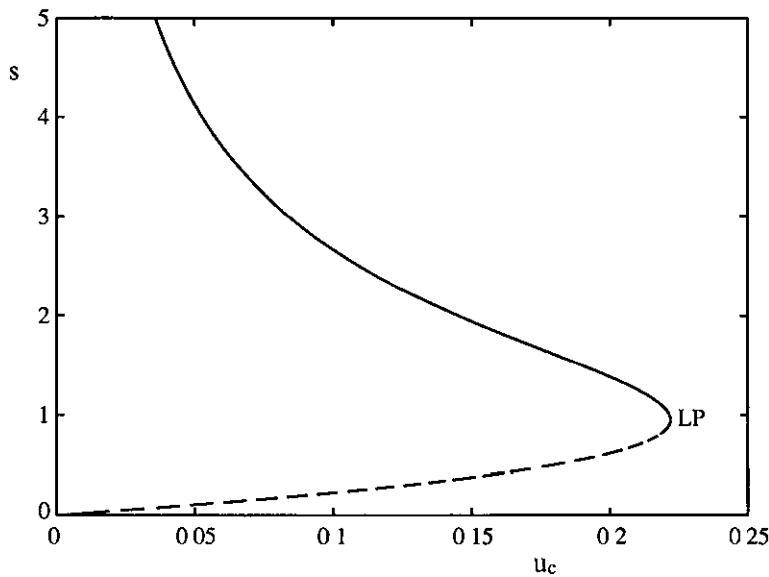


Figure 4.2 Speed s as a function of the dimensionless threshold parameter u_c in the continuum FDF model for the parameters $\tau_d = \tau_R = D = 1$. A linear stability analysis shows that the fast branch is stable [34].

4.3 Periodic travelling wave

In this section we consider periodic travelling waves in the generalised FDF model. We construct periodic travelling waves by writing release times in the form $T^m(x) = (m + kx)\Delta$, where k is the wavenumber and $s = 1/(k\Delta)$ the wave velocity. The travelling wave ODE in the travelling frame co-ordinate system ($\xi = st - x$) is given by equation (4.6). The periodic travelling wave solution to (4.6) takes the form

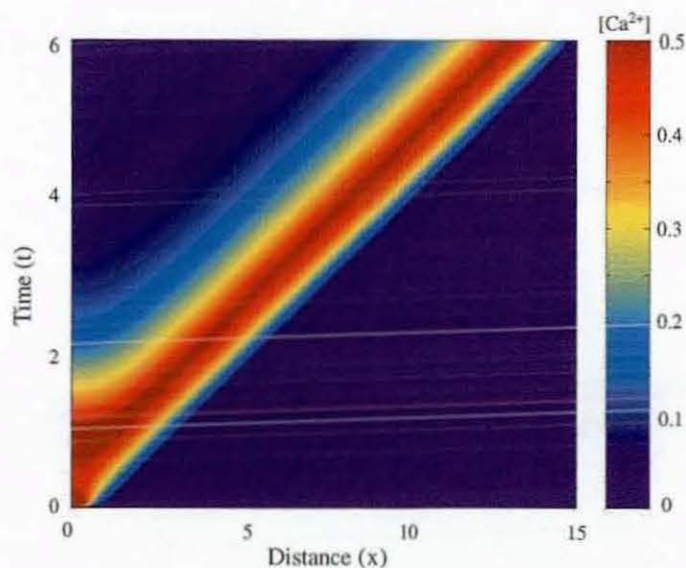


Figure 4.3: Space-time plot of the calcium concentration showing the solitary travelling wave propagation in the continuum FDF model with the parameters from Figure 4.2 and $u_c = 0.1$.

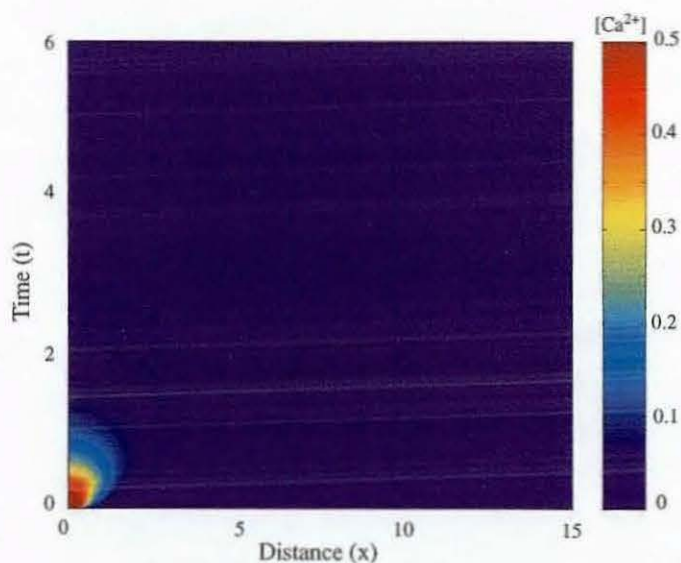


Figure 4.4: Space-time plot of the calcium concentration showing the propagation failure of solitary travelling wave in the continuum FDF model with the parameters from Figure 4.2 and $u_c = 0.25$.

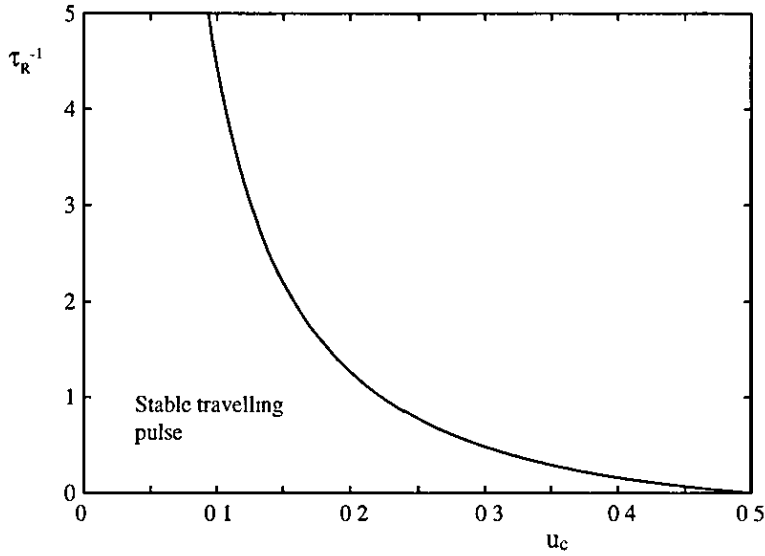


Figure 4.5: Continuation of the limit point shown in Figure 4.2 in the (u_c, τ_R^{-1}) parameter plane

$$u(\xi) = u(\xi + m\Delta):$$

$$u(\xi) = \begin{cases} \alpha_1 e^{\lambda_+ \xi} + \alpha_2 e^{\lambda_- \xi} + \tau_d \sigma / \tau_R & 0 < \xi < s\tau_R \\ \alpha_3 e^{\lambda_+ \xi} + \alpha_4 e^{\lambda_- \xi} & s\tau_R < \xi < s\Delta, \end{cases} \quad (4.14)$$

with λ_{\pm} given by equation (4.8). By demanding continuity of the solution and its first derivative the coefficients $\alpha_1, \dots, \alpha_4$ may be found as follows

$$\alpha_1 = \frac{\tau_d \sigma}{\tau_R} \frac{\lambda_-}{(\lambda_- - \lambda_+)} \frac{(1 - e^{\lambda_+ s(\Delta - \tau_R)})}{(e^{\lambda_+ s\Delta} - 1)} \quad (4.15)$$

$$\alpha_2 = -\frac{\tau_d \sigma}{\tau_R} \frac{\lambda_+}{(\lambda_- - \lambda_+)} \frac{(1 - e^{\lambda_- s(\Delta - \tau_R)})}{(e^{\lambda_- s\Delta} - 1)} \quad (4.16)$$

$$\alpha_3 = \frac{\tau_d \sigma}{\tau_R} \frac{\lambda_-}{(\lambda_- - \lambda_+)} \frac{(1 - e^{-\lambda_+ s\tau_R})}{(e^{\lambda_+ s\Delta} - 1)} \quad (4.17)$$

$$\alpha_4 = -\frac{\tau_d \sigma}{\tau_R} \frac{\lambda_+}{(\lambda_- - \lambda_+)} \frac{(1 - e^{-\lambda_- s\tau_R})}{(e^{\lambda_- s\Delta} - 1)}. \quad (4.18)$$

The self-consistent speed of the periodic travelling wave may be found by demanding $u(s\Delta) = h$. This generates an implicit equation for the dispersion relation $s = s(\Delta)$.

$$u_c \frac{1 - e^{-\Delta/\tau}}{1 - \gamma e^{-\Delta/\tau}} = \frac{\lambda_-}{(\lambda_- - \lambda_+)} \frac{(1 - e^{-\lambda_+ s \tau_R})}{(e^{\lambda_+ s \Delta} - 1)} - \frac{\lambda_+}{(\lambda_- - \lambda_+)} \frac{(1 - e^{-\lambda_- s \tau_R})}{(e^{\lambda_- s \Delta} - 1)}, \quad (4.19)$$

where $u_c = u_{th} \tau_R / \tau_d \sigma$. We plot a typical dispersion curve in Figure 4.6, showing a similar shape to that of the DYK model (see Figure 3.13). No attempt has been made to tune free parameters of the FDF model to obtain a quantitative fit to data from the DYK (or other) model. We invoke the model independent kinematic theory presented earlier to establish that it is the faster of the two possible branches that is stable. Moreover, since the stable branch of the dispersion curve has an exponential shape, stable waves representing connections to periodics are also expected. If we neglect refractoriness and consider a constant threshold, the resulting dispersion curve exhibits unphysical divergent speeds. This is expected in the absence of a refractory process, since release events can occur arbitrarily close in time. In Figure 4.7 we illustrate an

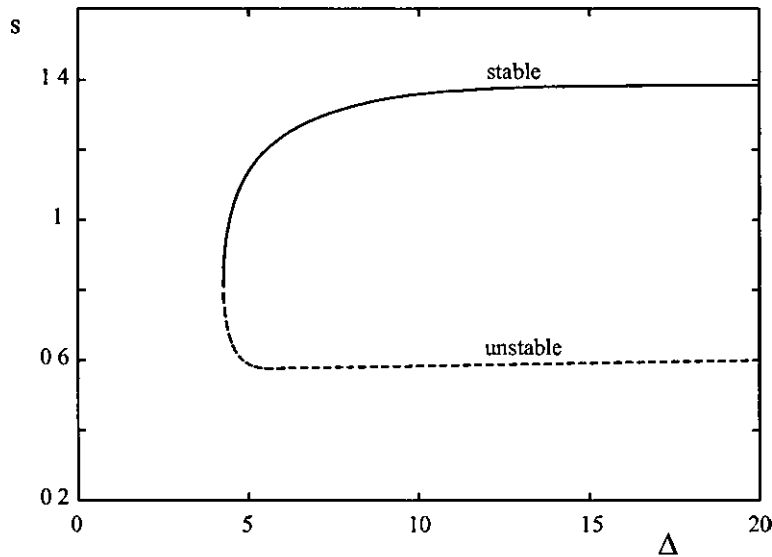


Figure 4.6 The dispersion curve obtained from (4.19) when $u_c = 0.2$, $\tau = 2$, $\gamma = 3$, $\tau_R = 1$, $\tau_d = 1$ and $D = 1$.

example of a periodic travelling wave in the continuum FDF model. Solitary pulses constructed in section 4.2 may also be defined from periodic solution by taking the limit $\Delta \rightarrow \infty$.

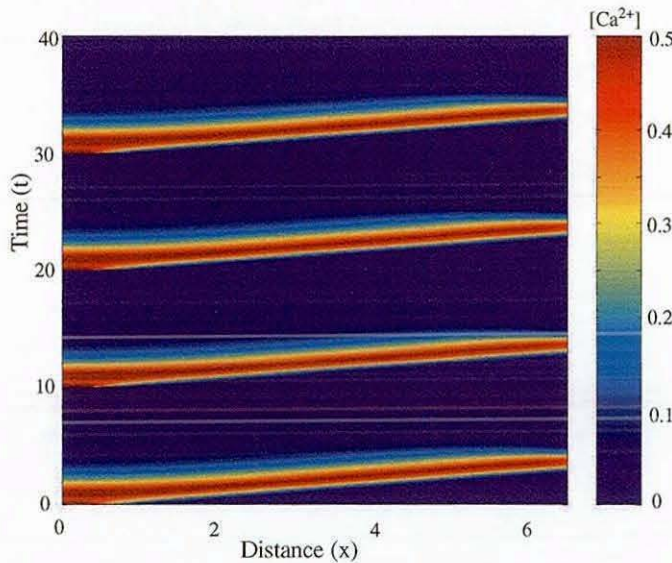


Figure 4.7: *Space-time plot of the calcium concentration showing the periodic travelling wave propagation in the continuum FDF model with the parameters from Figure 4.6 and $\Delta = 10$.*

A weakness of the FDF model is that it is independent of IP_3 concentration, which as we have seen is an important parameter of the DYK model. To include a notion of IP_3 sensitivity within an FDF model it is natural to modify the threshold parameter, such that release events are easier to generate in the presence of high IP_3 . We suggest that the level of Ca^{2+} in the ER, c_{er} , required to generate a periodic travelling wave is a good candidate for determining a threshold function $u_{\text{th}} = u_{\text{th}}(p)$. In Figure 4.8 we continue Hopf points of Figure 3.5 that define the borders of such a region in the (p, c_{er}) parameter plane. This figure shows that for small values of IP_3 waves fail to propagate and that lower levels of c_{er} are required to generate waves with increasing $[\text{IP}_3]$, as observed experimentally. We approximate the threshold function of Figure 4.8 using

$$u_{\text{th}}(p) = k \left[u_0 + A \frac{e^{-Bp}}{p - C} \right], \quad (4.20)$$

where $k = 1$, $u_0 = 0.48$, $A = 0.1627$, $B = 0.5583$ and $C = 0.055$ are fitted numerically.

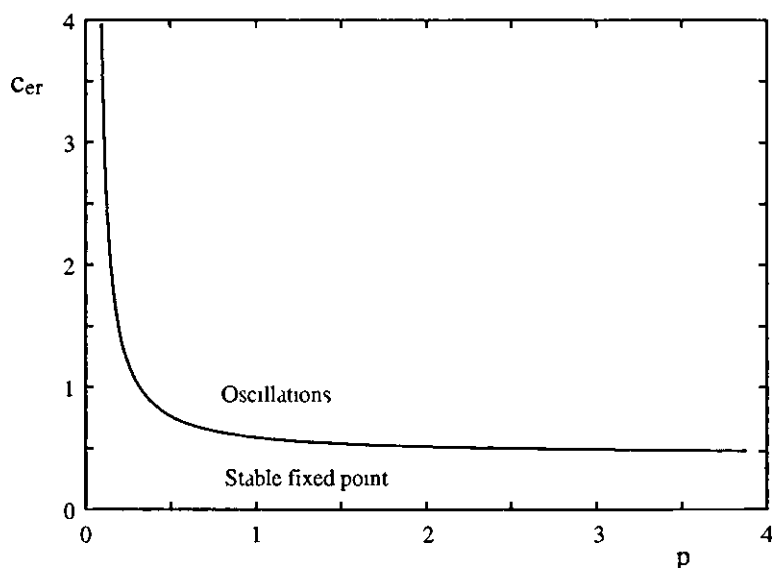


Figure 4.8. Concentration of calcium in the ER, c_{er} , as a function of IP_3 concentration, p , in the DYK model, required to generate travelling waves

The inclusion of an IP_3 dependent threshold level in the FDF model makes it sensitive to IP_3 and allows a more direct comparison with results from the DYK model

In Figure 4.9 we plot the wave speed of a pulse as a function of the IP_3 concentration. In the same figure we plot the homoclinic branch A of the DYK model from Figure 3.5 for better visualisation. For a comparison between the DYK model and the generalised FDF model we choose the same diffusion coefficient and adjust the remaining time and strength scales appropriately. A value for τ_R is chosen simply by reading off the temporal duration of a calcium spike in the DYK model. The time scale of the linear pump in the FDF model is chosen so as best to agree with that of nonlinear pump term in equation (2.16). This term is sigmoidal with a slowly varying gradient for intermediate levels of calcium concentration. The gradient in this intermediate regime provides a reasonable estimate for τ_d . This leaves only one free parameter, namely k , which we choose so as to give the best quantitative agreement of the generalised FDF and DYK models. Note that both curves in Figure 4.9 are very similar. In the

absence of an IP_3 dependent threshold function no such comparison would have been possible.

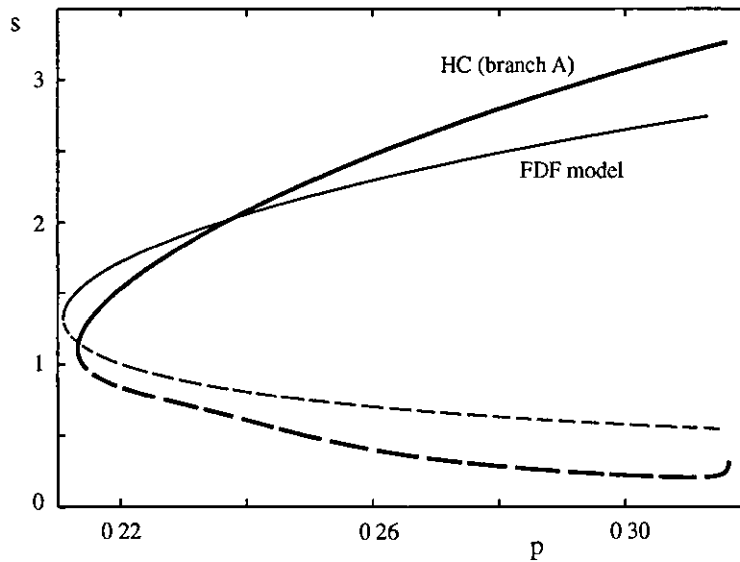


Figure 4.9 Speed of the travelling pulse in the FDF continuum model as a function of $[IP_3]$ with $k = 0.17$, $\tau_R = 0.5$, $\tau_d = 0.29$ and $D = 1$. The second curve is the homoclinic branch A of the DYK model from Figure 3.5

Summary

In this chapter we demonstrated that much of the travelling wave behaviour of the biophysical DYK model in Chapter 3 can be reproduced by a much simpler FDF type model. We presented a generalised form of continuum FDF model with an IP_3 dependent threshold and a simple refractory process. Parameters of the FDF model are constrained using numerical data from the DYK model. The main advantage of studying FDF type models is their mathematical tractability. A mathematical analysis of solitary and periodic travelling waves shows the ability of the generalised FDF model to describe realistic travelling Ca^{2+} waves. The analytical tractability of the model also opens up the possibility to study more realistic distributions of release sites and this is discussed in the next chapter.

Chapter 5

Discrete Fire-Diffuse-Fire model

Our discussion of the FDF model in the previous chapter began with the issue of cellular heterogeneity in a variety of cell types. The majority of the spatial whole-cell models (see Chapter 2) are based on the assumption that the ER can be represented as a compartment continuously distributed throughout the cytosol. Although it can sometimes be rigorously justified, this assumption is made largely for convenience. The images of Ca^{2+} activity in cardiac myocytes confirm the facts of cellular inhomogeneity (see Figure 5.1), demonstrating isolated Ca^{2+} sparks, wave initiation and a spark-mediated propagating Ca^{2+} wave. Skeletal muscle and cardiac cells are invaded by *T-tubules*, which allow communication with the extracellular space. T-tubules have VOCCs allowing the influx of calcium into the cell in response to an action potential. The RyRs through which calcium is released are located directly opposite the calcium channels. The physical arrangement of calcium release sites means that in these cell types it may not be appropriate to view the release of calcium as spatially uniform. In cardiac cells, calcium waves do not normally propagate without T-tubule stimulus. The discreteness of calcium release sites in these cell types prevents the spontaneous propagation of a calcium wave, which would lead to spontaneous (uncontrolled) muscular contraction. This is a possible situation in which the discreteness of release sites

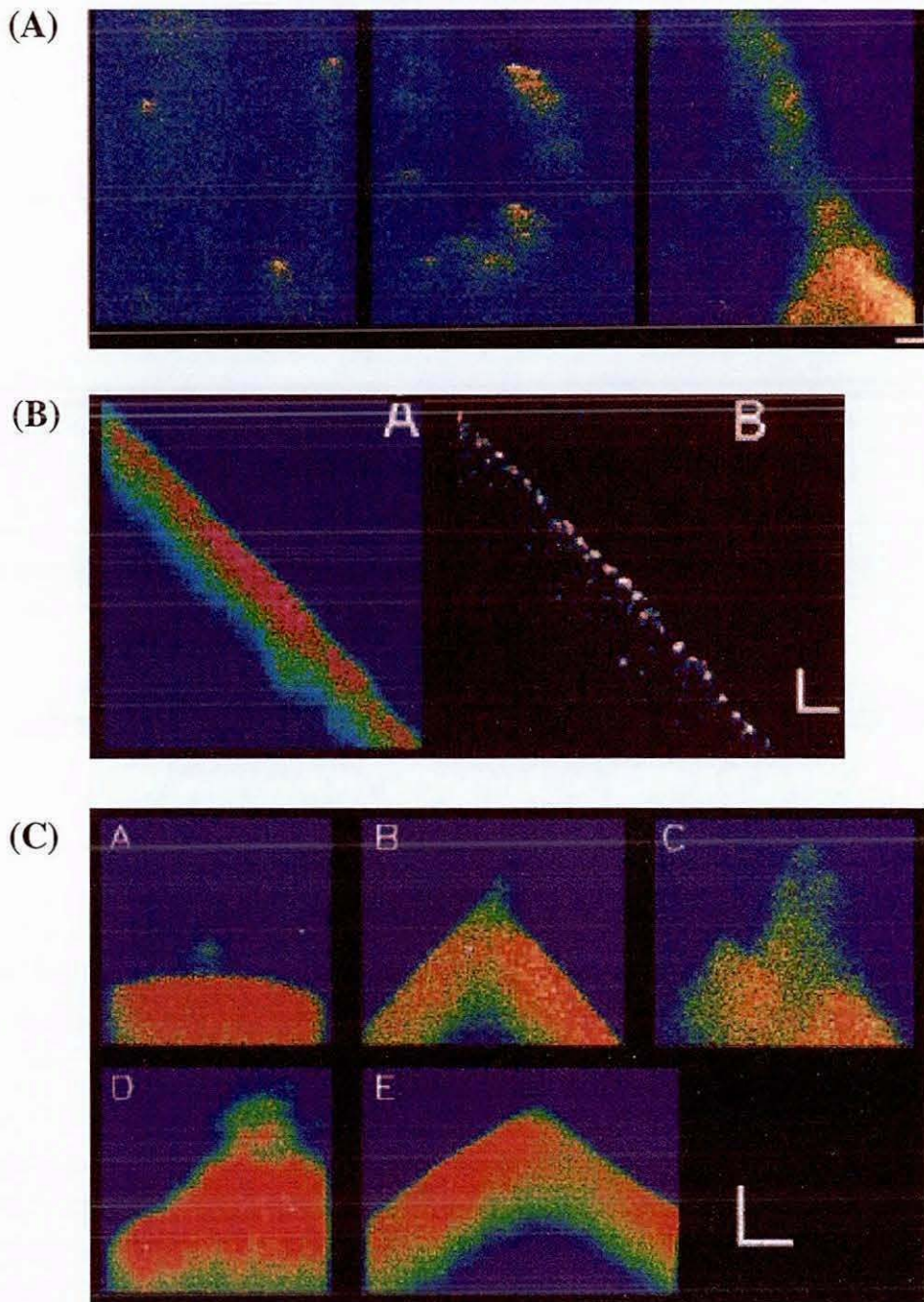


Figure 5.1: *Confocal line-scan images of isolated Ca^{2+} sparks, wave initiation, and a spark-mediated propagating Ca^{2+} wave in cardiac myocytes. Horizontal scale bar (space): $5\text{ }\mu\text{m}$ except for panels B, C and E in (C) which is $10\text{ }\mu\text{m}$; vertical scale bar (time): 100 ms except for (C) and second panel in (A) which is 200 ms . (From the work of Cheng et al. [30]).*

could have major negative consequences. For example, in hypertension, cardiac cells compensate for increased pressure by growing larger (hypertrophy). It is possible that in this hypertrophied state, the separation between RyRs and T-tubules is increased, leading to less effective coupling between action potentials and calcium release, and impaired contraction [176]

The generalised FDF model may be naturally extended to include the discrete nature of calcium stores within a cell. In this chapter we consider the FDF model defined in Chapter 4 with a discrete distribution of calcium release sites. This simple change to any continuum model destroys translation invariance and invalidates many of the standard tools of analysis. However, within the FDF framework analytical progress is still possible. To illustrate this point we investigate how a regular array of release sites influences the propagation of saltatory travelling waves. Making the further assumption that release events occur on a regular temporal lattice we simplify the FDF model so that it may be re-written in the language of binary *release events*. We introduce a dynamics for the release events that are calculated via a thresholding of the calcium profile at a release site. Thus, under the assumption that release times occur on some regular temporal lattice the model does not have to be evolved as a discontinuous PDE with a self-consistent search for the times of threshold crossing that define release events. Direct numerical simulations are used to show that this computationally cheap version of the FDF model provides an accurate representation of the original model.

5.1 Spatially discrete FDF model

One of the major advantages of the generalised FDF model given by equation (4.2) is that it may be naturally extended to account for saltatory travelling wave propagation. Continuous and discrete limits in the model are achieved by specifying the form of the distribution function of Ca^{2+} release sites $\rho(x)$. The discrete approximation

in the FDF model may be obtained by modelling Ca^{2+} release sites as point sources, that is, an array of Dirac delta functions $\delta(x - x_n)$, where x_n is the spatial position of the n th release site. For simplicity we consider an idealised set of point sources so that the function of the distribution of Ca^{2+} release sites is given by $\rho(x) = \sum_n \delta(x - nd)$, where d is the spacing between stores. The general structure of the model is given by the simple schematic diagram of Figure 5.2. The FDF model provides a caricature of Ca^{2+} release events which interact via diffusion of Ca^{2+} and the triggering of a CICR-like mechanism. Ca^{2+} puffs or sparks in the model are triggered from the re-

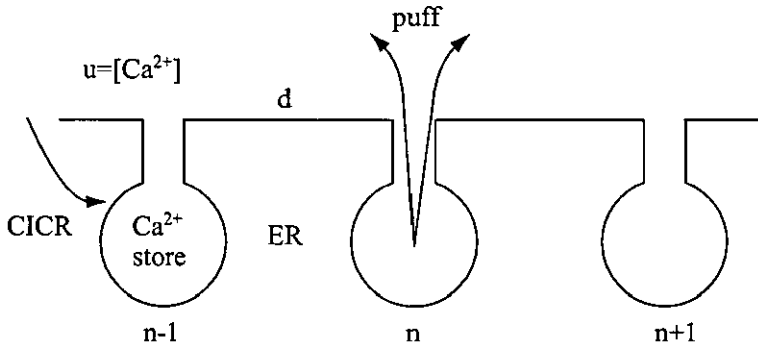


Figure 5.2 Schematic representation of the FDF model

lease site $x_n = nd$ at times $T^m(x_n)$, $m \in \mathbb{Z}$, according to a threshold process defined by (4.3). The shape of the puff is assumed to be the same as in the continuum FDF model and is given by equation (4.5).

5.1.1 Periodic travelling wave

The solution of the FDF model given by equation (4.2) with a discrete distribution of Ca^{2+} release sites can be expressed in the terms of the Green's function for the cable equation as

$$u(x, t) = \frac{\sigma}{\tau_R} \sum_{n=-\infty}^{\infty} \int_{-\infty}^t dt' \int_{-\infty}^{\infty} dx' G(x - x', t - t') \delta(x' - x_n) \sum_{m=0}^{\infty} \eta(t' - T^m(x_n)), \quad (5.1)$$

where

$$G(x, t) = \frac{e^{-t/\tau_d}}{\sqrt{4\pi Dt}} e^{-x^2/(4Dt)} \Theta(t) \quad (5.2)$$

The substituting of the function $\eta(t)$ into equation (5.1) gives

$$\begin{aligned} u(x, t) &= \frac{\sigma}{\tau_R} \sum_{n=-\infty}^{\infty} \int_{-\infty}^t dt' \int_{-\infty}^{\infty} dx' G(x - x', t - t') \delta(x' - x_n) \\ &\times \sum_{m=0}^{\infty} \Theta(t' - T^m(x_n)) \Theta(\tau_R - (t' - T^m(x_n))) \\ &= \frac{\sigma}{\tau_R} \sum_{n=-\infty}^{\infty} \sum_{m=0}^{\infty} \int_{T^m(x_n)}^{T^m(x_n) + \tau_R} G(x - x_n, t - t') dt' \end{aligned} \quad (5.3)$$

We consider periodic travelling waves that satisfy $T^m(x_n) = nd/s + m\Delta \equiv n\Delta_1 + m\Delta$, $m \geq 1$, where s is the speed of threshold crossing events given by $s = d/\Delta_1$ and Δ is the time between successive Ca^{2+} release events at a store. For simplicity we shall consider Δ to be sufficiently large that we do not have to worry about the inclusion of refractory process and take the threshold for release to be $u_{\text{th}}(p)$ defined by equation (4.20). Then the solution describing saltatory periodic travelling waves in the FDF model is

$$u(x, t) = \frac{\sigma}{\tau_R} \sum_{n,m} \int_0^{\min(t - n\Delta_1 - m\Delta, \tau_R)} G(x - nd, t - t' - n\Delta_1 - m\Delta) dt'. \quad (5.4)$$

This can be rewritten as

$$u(x, t) = \sigma \sum_{n,m} H(x - nd, t - n\Delta_1 - m\Delta), \quad (5.5)$$

where

$$H(x, t) = \frac{1}{\tau_R} \int_0^{\min(t, \tau_R)} G(x, t - t') dt' \quad (5.6)$$

We determine the speed of the travelling waves in a self-consistent manner by demanding that

$$\lim_{n,m \rightarrow \infty} u(nd, n\Delta_1 + m\Delta) = u_{\text{th}}(p) \quad (5.7)$$

Then using initial data such that $u(0,0) = 0$ the speed of the wave is implicitly determined by

$$u_{th}(p) = \sigma \sum_{n=0}^{\infty} \sum_{m=1}^{\infty} H(nd, n\Delta_1 + m\Delta), \quad (5.8)$$

with

$$H(x, t) = \frac{1}{\tau_R} \int_0^{\tau_R} G(x, t - t') dt' \quad (5.9)$$

A saltatory periodic travelling wave determined by (5.4) and (5.8) is shown in Figure 5.3. This nicely illustrates that waves propagate with a non-constant profile and that large increase in Ca^{2+} concentration occurs just after a release event. The saltatory nature of the wave may be directly attributed to the fact that release sites are not spread continuously throughout the system.

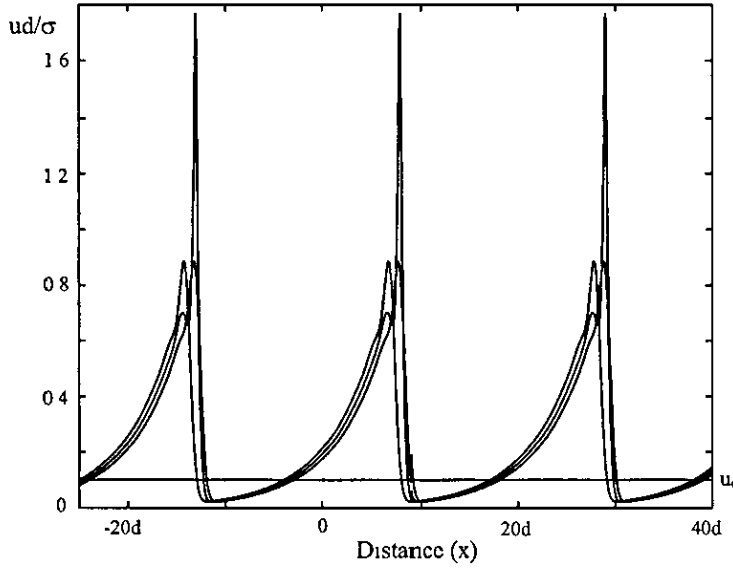


Figure 5.3 An example of a stable saltatory periodic travelling wave. The period Δ_1 is determined self-consistently as $\Delta_1 = 0.2$. Other parameters are $\tau_d = 1$, $d^2/D = 1$, $\tau_R = 0.1$, $\Delta = 4.2$ and $u_c \equiv u_{th}(p)d/\sigma = 0.1$. The system is sampled at some large release time t_0 , then at $t_0 + \tau_R$ and $t_0 + \Delta_1$.

We now demonstrate how the period of travelling waves depends on the main system.

parameters. In the special case $\tau_R \rightarrow 0$ we see from equation (5.9) that $H(x, t) \rightarrow G(x, t)$, which is given in closed form by (5.2). Hence, the speed of the wave can be found by solving

$$\begin{aligned} \frac{u_{th}(p)d}{\sigma} &= d \sum_{n=0}^{\infty} \sum_{m=1}^{\infty} G(nd, n\Delta_1 + m\Delta) \\ &= \sum_{n=0}^{\infty} \sum_{m=1}^{\infty} \sqrt{\frac{\tau_D}{4\pi(n\Delta_1 + m\Delta)}} \exp\left(-n \left[\frac{\Delta_1}{\tau_d} + \frac{n\tau_D}{4(n\Delta_1 + m\Delta)} \right]\right) \exp\left(-\frac{m\Delta}{\tau_d}\right) \end{aligned} \quad (5.10)$$

where $\tau_D = d^2/D$. For finite τ_R , the function $H(x, t)$ is evaluated in [34] as $H(x, t) = A(x, t - \tau_R) - A(x, t)$, where

$$\begin{aligned} A(x, t) &= \frac{\sqrt{\tau_d D}}{4D\tau_R} \left[\exp\left(\frac{-|x|}{\sqrt{\tau_d D}}\right) \operatorname{erfc}\left(-\frac{|x|}{\sqrt{4Dt}} + \sqrt{\frac{t}{\tau_d}}\right) \right. \\ &\quad \left. + \exp\left(\frac{|x|}{\sqrt{\tau_d D}}\right) \operatorname{erfc}\left(\frac{|x|}{\sqrt{4Dt}} + \sqrt{\frac{t}{\tau_d}}\right) \right] \end{aligned} \quad (5.11)$$

In Figure 5.4 we show how the period of travelling waves depends on the value of τ_d^{-1} for the case that $\tau_R = 0$. We see that there is propagation failure at some critical value of τ_d , where two branches of the solutions coalesce. To illustrate the effects of a finite width for the calcium puff on the speed of the periodic travelling wave we continue the LP of the bifurcation diagram in Figure 5.4 as a function of τ_R . The results of a numerical continuation are shown in Figure 5.5. This plot shows the parameter region where saltatory periodic travelling waves can exist and highlights the fact that with increasing τ_R the LP in Figure 5.4 occurs at increasingly larger values of τ_d .

The fact that there are two solution branches for a periodic travelling wave raises the question of stability. To determine the stability of saltatory waves we consider perturbation of the release times where $T^m(nd) \rightarrow T^m(nd) + e^{m\lambda}$, $\lambda \in \mathbb{C}$, and examine the linearised evolution of these perturbations. Solutions are linearly stable if $\operatorname{Re} \lambda <$

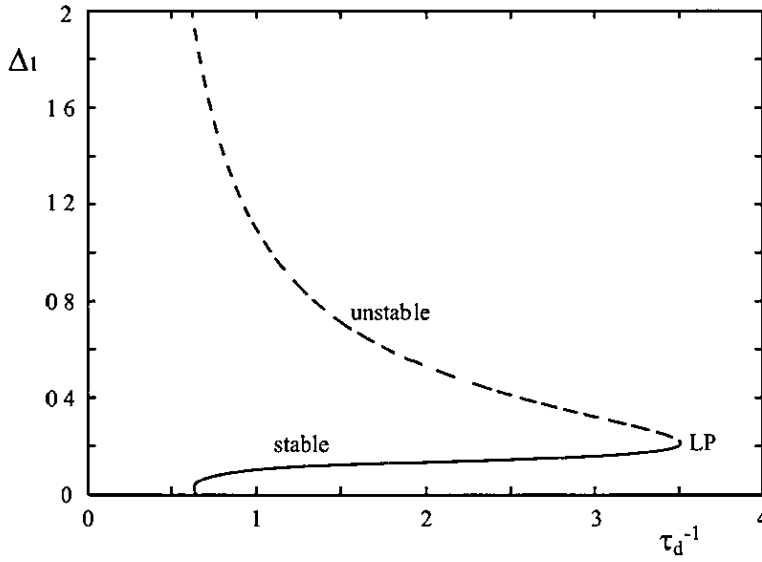


Figure 5.4: Period Δ_1 as a function of the parameter τ_d^{-1} with $\tau_R = 0$. Other parameters as in Figure 5.3

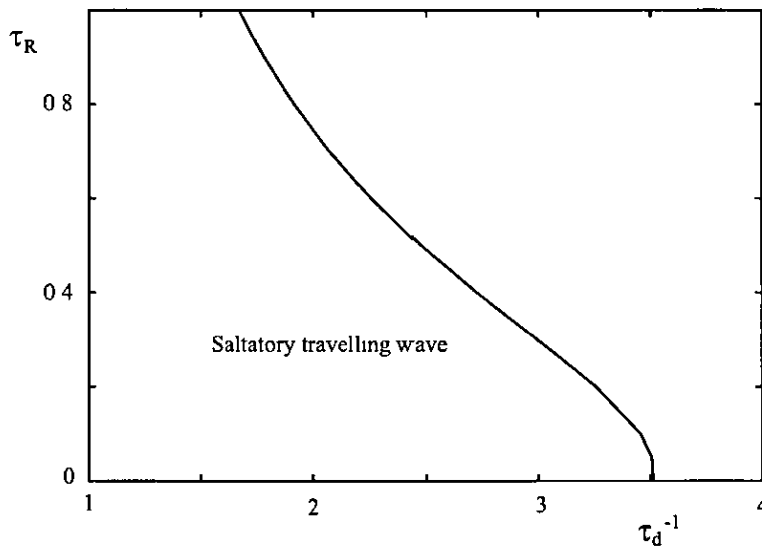


Figure 5.5: Continuation of the LP of Figure 5.4 in the (τ_d^{-1}, τ_R) plane

0 After substituting into equation (5.8) and expanding to first order we obtain

$$\Phi(\alpha, \beta) \equiv \sum_{n,m} e^{m\alpha} e^{im\beta} H'(nd, n\Delta_1 + m\Delta) = 0, \quad (5.12)$$

where we have set $\lambda = \alpha + i\beta$, $\alpha, \beta \in \mathbb{R}$. Here, $H'(x, t) = \partial H(x, t)/\partial t$. Differentiation of equation (5.9) shows that $H'(x, t) = [G(x, t) - G(x, t - \tau_R)]/\tau_R$. To find the stability of the solution as a function of parameters the system of two equations $\text{Re } \Phi(\alpha, \beta) = 0$ and $\text{Im } \Phi(\alpha, \beta) = 0$ has to be solved simultaneously for α and β along the solution branch. Two possible types of bifurcation point are defined by the conditions $\alpha = 0$, $\beta = 0$ and $\alpha = 0$, $\beta \neq 0$. For the first case a change in stability occurs when $\Phi(0, 0) = 0$. The second type of instability arises when a complex

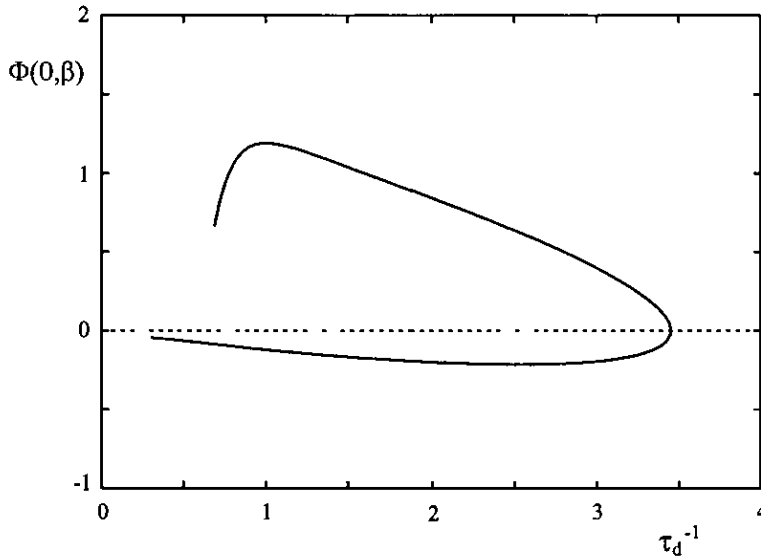


Figure 5.6 A plot of the function $\Phi(0, \pi)$ along the solution of Figure 5.4, showing that there is a change in stability at the LP where propagation failure occurs

eigenvalue crosses the imaginary axis. Then a change of stability occurs when $\beta = \pi$. A plot of the function $\Phi(0, \pi)$ in Figure 5.6 shows that the change of stability for the solution shown in Figure 5.4 occurs at the LP defining propagation failure. A direct examination of $\alpha = \text{Re } \lambda$, along the two solution branches, shows that the faster branch is stable, while the slower one is unstable.

5.1.2 Solitary travelling pulse

In the absence of multiple Ca^{2+} release events from an individual store, i.e. considering the case when $m = 0$, we recover the discrete FDF model of solitary travelling wave propagation [34]. A saltatory travelling pulse solution is analytically determined by the following equation

$$u(x, t) = \frac{\sigma}{\tau_R} \sum_{n=-\infty}^{\infty} \int_0^{\min(t-n\Delta_1, \tau_R)} G(x - nd, t - t' - n\Delta_1) dt' \quad (5.13)$$

and is illustrated in Figure 5.7. The speed of the solitary wave can be found in a

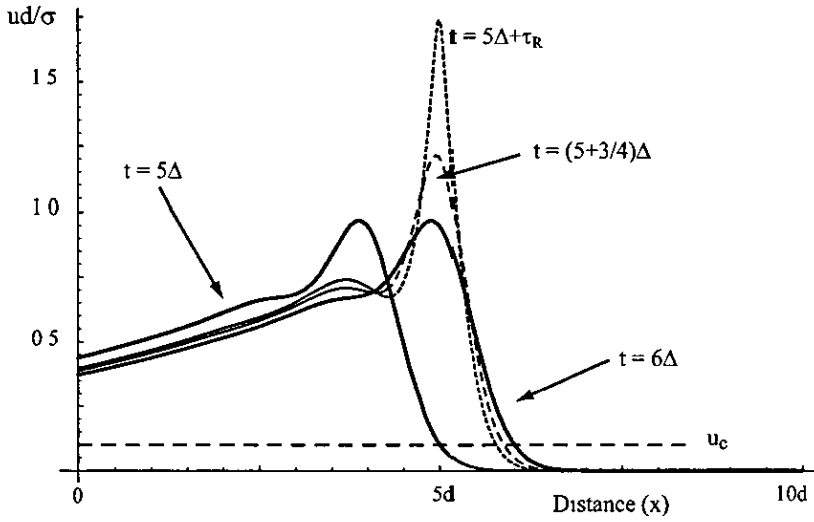


Figure 5.7 An example of a stable saltatory solitary travelling wave. The period Δ_1 is determined self-consistently as $\Delta_1 = 0.17$. Other parameters as in Figure 5.3.

self-consistent manner similar as in the periodic case by demanding that

$$\lim_{n \rightarrow \infty} u(nd, n\Delta_1) = u_{th}(p) \quad (5.14)$$

and for the special case when $\tau_R \rightarrow 0$ this gives

$$u_c \equiv \frac{u_{th}(p)d}{\sigma} = \sum_{n=0}^{\infty} \sqrt{\frac{\tau_D}{4\pi n\Delta_1}} \exp\left(-n \left[\frac{\tau_D}{4\Delta_1} + \frac{\Delta_1}{\tau_d} \right]\right) \quad (5.15)$$

In Figure 5.8 we show how the speed of solitary travelling pulse depends on the dimensionless threshold parameter u_c . In common with the periodic wave solution there is the co-existence of two travelling waves with speeds that approach each other as the threshold parameter increases. Eventually the two solitary waves coalesce at the LP such that propagation failure can result for too large a choice of the threshold parameter.

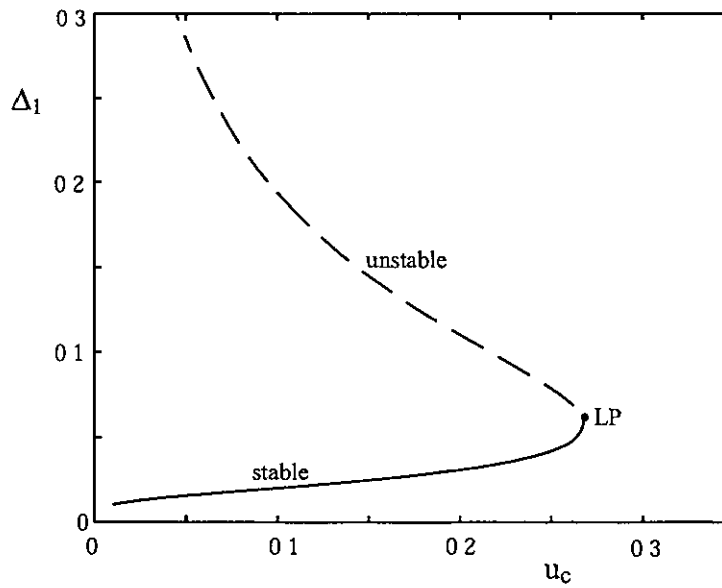


Figure 5.8 Period Δ_1 as a function of the dimensionless threshold parameter u_c with $\tau_R = 0$. Other parameters as in Figure 5.7.

5.2 Discrete-time FDF model

5.2.1 One-dimensional model

The analytical tractability of the discrete FDF model is not only useful for gaining insight into the dependence of wave speed on system parameters, but can help in reducing the computational demands on a numerical scheme for the self-consistent

evolution of the model equation. Consider for the moment the class of solutions where all release times occur at integer multiples of τ_R , the rise-time of the receptor. In this case we may write

$$\sum_m \eta(T_n^m) = \sum_p \eta(p\tau_R) a_n(p), \quad (5.16)$$

for all n , where we define the *release function* $a_n(p)$ as

$$a_n(p) = \begin{cases} 1 & T_n^m = p\tau_R \\ 0 & \text{otherwise} \end{cases}, \quad (5.17)$$

and $T_n^m = T^m(x_n)$ is the time of release of the m th puff at the n th release site. In general the release times will not occur at multiples of τ_R . However, by restricting the system so that release times do occur on a regular temporal lattice and choosing $\tau = R\tau_R$ (the refractory time scale) for some $R \in \mathbb{Z}$, we may write

$$a_n(p) = \Theta(u_n(p) - u_{th}) \prod_{m=1}^{\min(R,p)} \Theta(u_{th} - u_n(p-m)), \quad (5.18)$$

where $u_n(p) \equiv u(x_n, p\tau_R)$. The first term on the right is a simple threshold condition for the determination of a release event whilst the second term ensures that release events are separated by at least the refractory time scale τ . This restriction of the model eliminates the need for the precise determination of release times. The FDF model then takes the particularly simple form

$$Qu(x, t) = \frac{\sigma}{\tau_R} \sum_{n \in \Gamma} a_n(p) \delta(x - x_n), \quad p\tau_R < t < (p+1)\tau_R, \quad (5.19)$$

where Q is the linear differential operator

$$Q = \partial_t + \frac{1}{\tau_d} - D\partial_{xx}, \quad (5.20)$$

with Green's function given by equation (5.2) and Γ is a discrete set that indexes the stores.

The dynamics for $p\tau_R < t < (p+1)\tau_R$ is completely determined in terms of initial data $u_p(x) = u(x, p\tau_R)$ as

$$u(x, t) = \frac{\sigma}{\tau_R} \sum_{n \in \Gamma} a_n(p) H(x - x_n, t - p\tau_R) + (G \otimes u_p)(x, t), \quad (5.21)$$

where

$$H(x, t) = \int_0^t G(x, t-s) ds, \quad (5.22)$$

and

$$(G \otimes u_p)(x, t) = \int_{\mathbb{R}} G(x - x', t - p\tau_R) u_p(x') dx' \quad (5.23)$$

Compared to the original FDF model the one we have described here is computationally cheap to solve. Release events defined by $a_n(p) = 1$ are easily calculated since $u_n(p) \equiv u_p(x_n)$ may be written as a sum of two terms that are both amenable to fast numerical evaluation. In particular $u_p(x)$ may be written in terms of the *basis* functions $H_n(x) = \sigma H(x - x_n, \tau_R)/\tau_R$, so that

$$u_p(x) = \sum_{n \in \Gamma} a_n(p-1) H_n(x) + (G \otimes u_{p-1})(x, p\tau_R) \quad (5.24)$$

Since the basis functions $H_n(x)$ are fixed for all time they need only be computed once. For small τ_R we also have the useful result that $H(x, \tau_R) \rightarrow G(x, \tau_R)$, which is given in closed form by (5.2). The convolution in (5.24) may be performed efficiently using Fast Fourier Transform (FFT) techniques. Once again the FFT of $G(x, \tau_R)$ need only be computed once, so that it is only necessary to successively construct the FFT of $u_p(x)$ for $p = 0, 1, 2, \dots$. We then have that $G \otimes u_p = \mathcal{F}^{-1}(\mathcal{F}[G] \mathcal{F}[u_p])$, where \mathcal{F} denotes the FFT. Hence, under the assumption that release times occur on some regular temporal lattice the model does not have to be evolved as a discontinuous PDE with a self-consistent search for the times of threshold crossings that define release events.

Of course the above approach is only useful if the restricted class of solutions that we have focused on is in some sense close to solutions of the full model. To illustrate that this is the case for practical applications we compare the exact solution

of a saltatory travelling pulse with that from this model. In Figure 5.9 we plot the speed of a lurching solitary pulse for the full FDF model discussed in the previous section. On the same figure we plot numerical results obtained from our reduced FDF model. It can be seen that there is excellent agreement between the two, justifying the practical assumption that release events can be considered to occur only at integer multiples of the calcium puff duration. From experimental data it is apparent that the refractory time-scale is typically 50 times that of the release duration (see [87] for a discussion) so we assume $R = 50$ in our simulations if it is not specified. Typically τ_R is approximately 10 – 20 ms

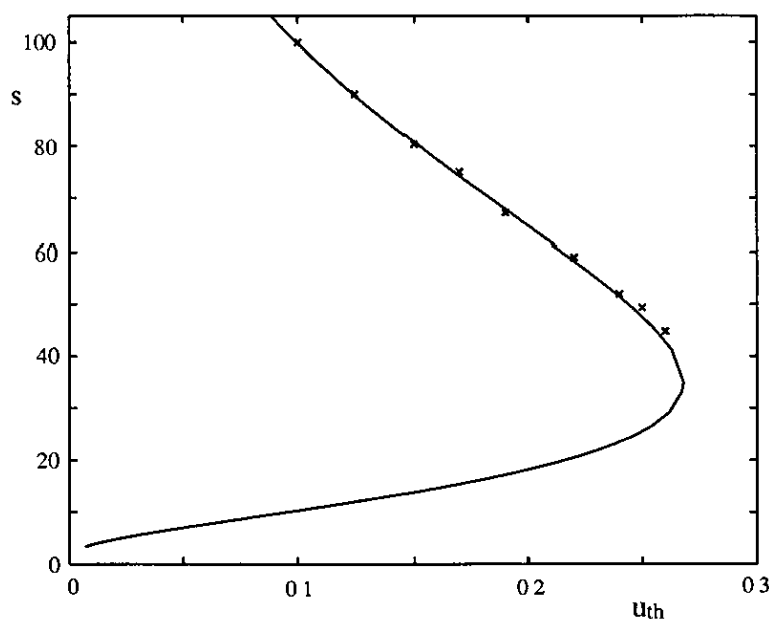


Figure 5.9 *Speed of a solitary pulse as a function of the threshold level u_{th} in the FDF model. Crosses denote results from simulations of the reduced FDF model with 500 regularly spaced stores. Parameters: $d = 2 \mu\text{m}$, $D = 30 \mu\text{m}^2/\text{s}$, $\tau = 10 \text{ ms}$, $\tau_d = 0.2 \mu\text{M}/\text{s}$*

The best way to illustrate the sort of behaviours that can be generated by this reduced model is with a space-time density plot for calcium concentration. In real cells release

sites are not likely to be arranged on a perfectly regular lattice, although for cardiac myocytes release sites are in fact regularly spaced along the longitudinal axis of the cell. In our simulations we focus both on regular and disordered distribution of release sites. Free boundary conditions are assumed in model simulations, i.e. wave propagation in the system is restricted only by cell size.

First of all, we present simulation results in one dimension for a regular lattice of release sites, with lattice spacing d . In Figure 5.10 we show a solitary lurching pulse arising from an initially activated release site in the middle of the cell. This nicely illustrates that a discrete set of release sites can lead to a wave that propagates with a non-constant profile, but with a well defined speed. Experimentally observed calcium waves, for example in immature *Xenopus* oocytes, evoked by stimuli just above the wave threshold do not propagate in a smoothly continuous manner either. The confocal linescan imaging of intracellular Ca^{2+} signal done by Callamaras *et al* [25] clearly shows this in Figure 5.11. In the case when two waves are initiated at well separated release sites, two lurching pulses will propagate toward each other. In Figure 5.12, we show that they are destroyed in wave-wave collisions just after the observed increase in Ca^{2+} concentration caused by their interaction. This phenomenon of wave-wave annihilation may be directly attributed to the refractoriness of the underlying release dynamics. Interestingly, by varying the parameters of the system we may also observe the propagation of periodic travelling waves. In practice this may be easily achieved by decreasing the refractoriness of the system, so that the Ca^{2+} concentration at the initially activated release site is still above the threshold after the refractory time and the system is ready to initiate a new travelling pulse. We demonstrate this behaviour in Figure 5.13. A similar effect may be obtained, for example, by increasing the diffusion or decreasing the threshold parameter in the model.

Now we consider a disordered distribution of release sites. In this case the position of release sites in a regular array is perturbed by a small random vector (of size

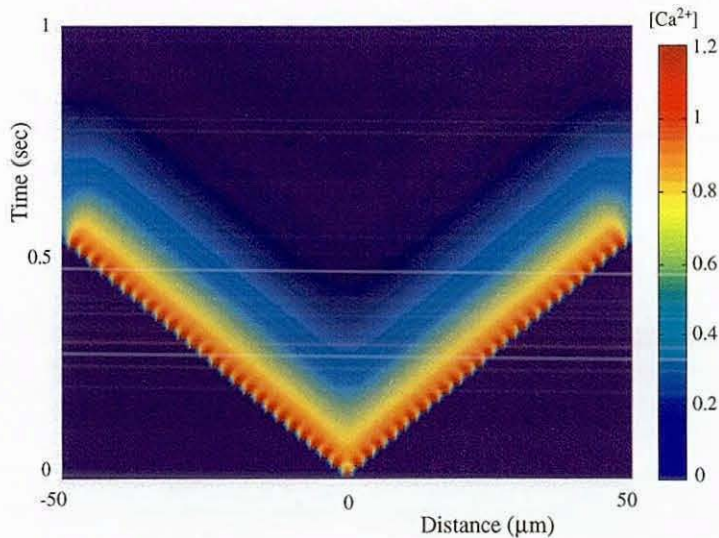


Figure 5.10: An example of two lurching pulses moving out from the center of a deterministic one-dimensional FDF model with 50 regularly spaced release sites. Parameters as in Figure 5.9 for a cell of linear dimension $100\ \mu\text{m}$ and $u_{th} = 0.1$.

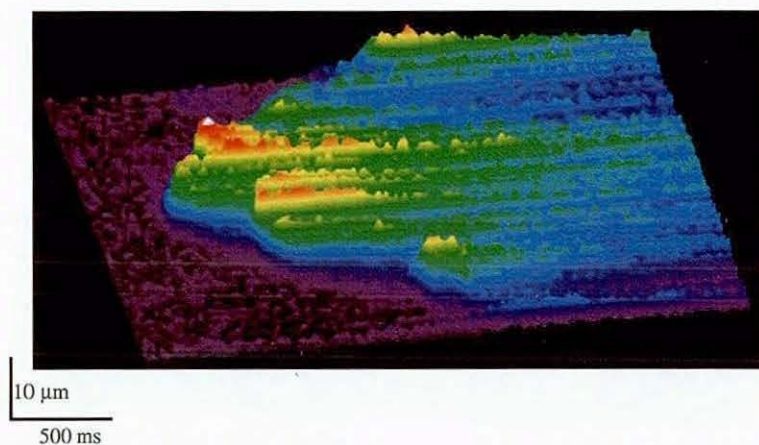


Figure 5.11: The confocal linescan image of saltatory wave propagation evoked by flash photolysis of IP_3 in immature *Xenopus* oocytes [25].

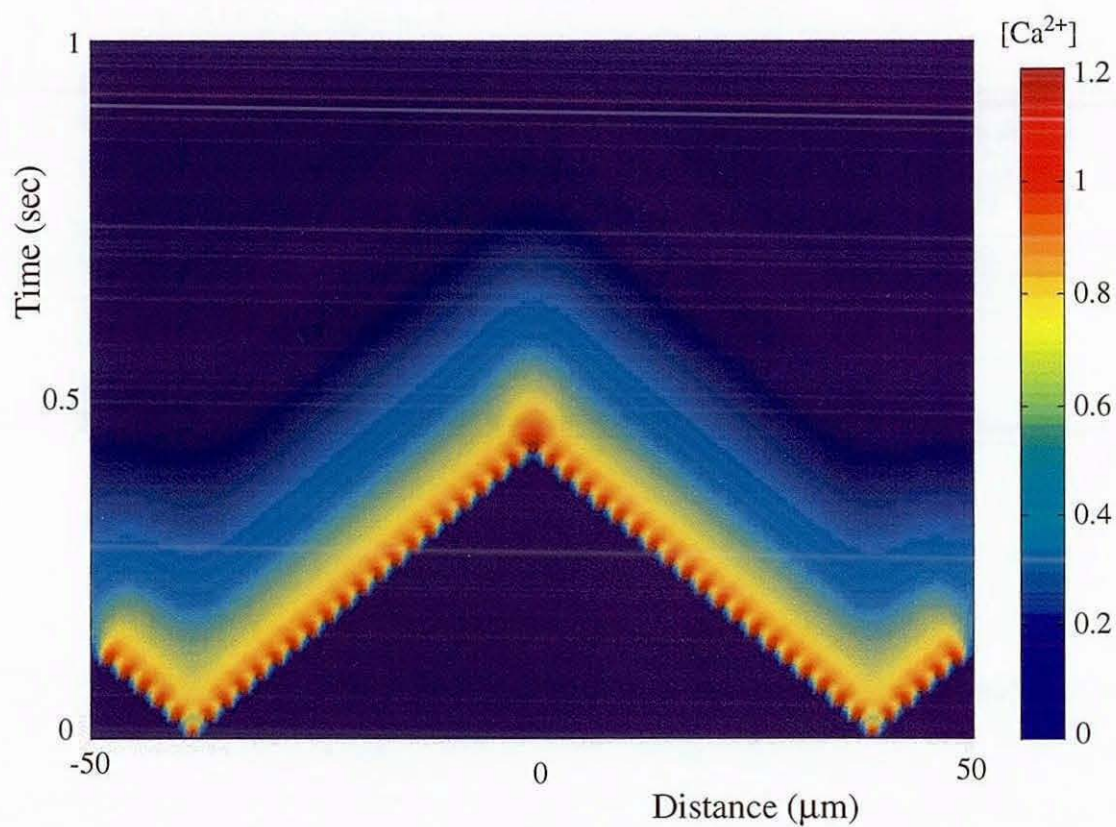


Figure 5.12: *An example of colliding pulses moving out from the release sites located apart on the distance of $60 \mu m$. Other parameters as in Figure 5.10. The interaction between two waves causes the propagation failure.*

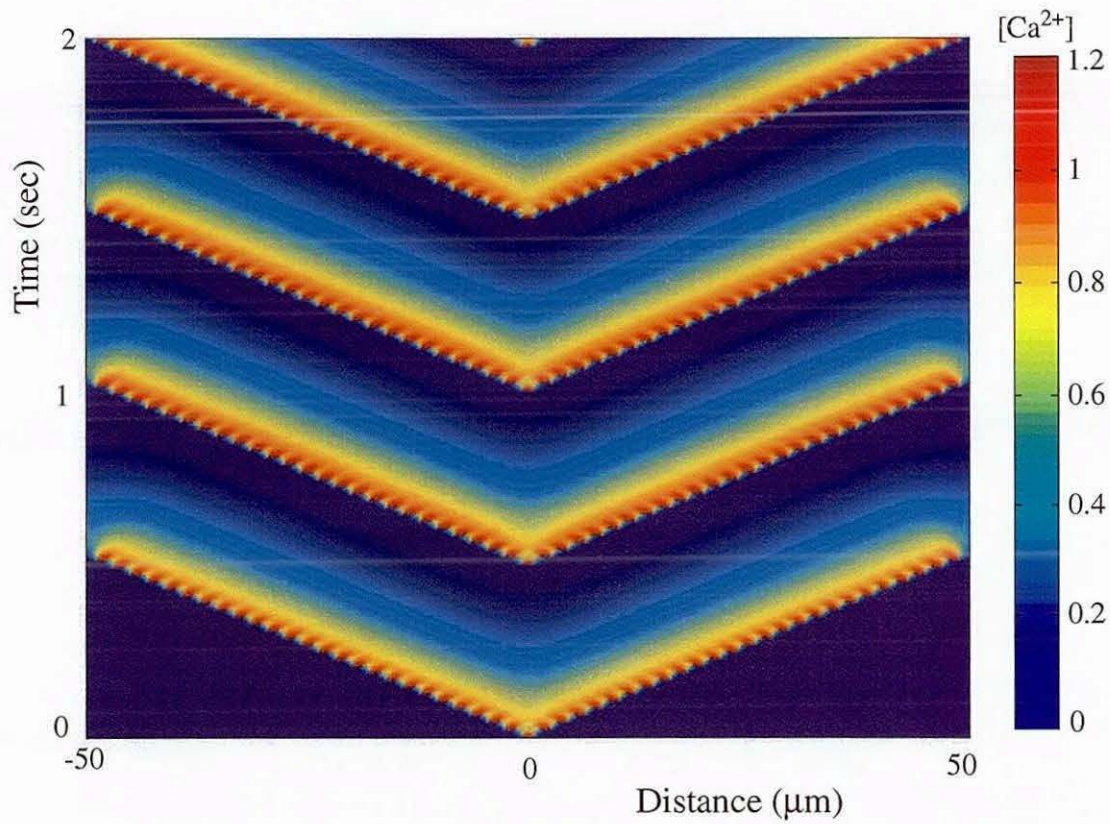


Figure 5.13: *An example of periodic travelling wave moving out from the center of a deterministic one-dimensional FDF model with 50 regularly spaced release sites with $R = 48$. Other parameters as in Figure 5.10.*

ϵd). Simulation results indicate that regular waves give way to more irregular waves, with the degree of irregularity increasing with the amount of spatial disorder. The irregularity of these waves is directly attributable to the quenched disorder of the release sites. Ultimately, if the degree of spatial disorder is sufficiently large we see propagation failure. Figure 5.14 shows an example of a periodic travelling wave in the system with a disordered distribution of release sites. This disorder gives rise to irregular activity, though with well defined periodicity. An example of disorder induced propagation failure is shown in Figure 5.15. The reason for this failure is that the average distance between release sites appears to be too large for the spreading of activity.

5.2.2 Two-dimensional model

The generalisation of our FDF model to two dimensions is both natural and straightforward by introducing a continuous spatial coordinate $\mathbf{r} \in \mathbb{R}^2$ and a discrete set of vectors $\mathbf{r}_n \in \mathbb{R}^2$, $n \in \mathbb{Z}$, indicating the positions of release sites. The basis functions $H(\mathbf{r} - \mathbf{r}_n)$ can be computed numerically from equation (5.22) with

$$G(\mathbf{r}, t) = \frac{e^{-t/\tau_d}}{4\pi Dt} e^{-r^2/(4Dt)} \quad (5.25)$$

and $r = |\mathbf{r}|$. However, it is also possible to compute the basis functions in closed form for two special cases. i) In the limit $\tau_d \rightarrow \infty$ then $H(\mathbf{r}) = E_1(r^2/4D\tau_R)/4\pi D$, where $E_1(x)$ is the exponential integral function

$$E_1(x) = \int_x^\infty dz \frac{e^{-z}}{z}. \quad (5.26)$$

This corresponds to the limit of zero pumping, where calcium is not removed from the cytosol. ii) For small τ_R we also have that $H(\mathbf{r}, t) \rightarrow G(\mathbf{r}, t)$ (as already noted in section 5.1.1). Since the puff duration is very small compared to τ this is a very accurate approximation, and so has been used in numerical simulations for this section.

First of all, we present simulation results on a regular square lattice, with release

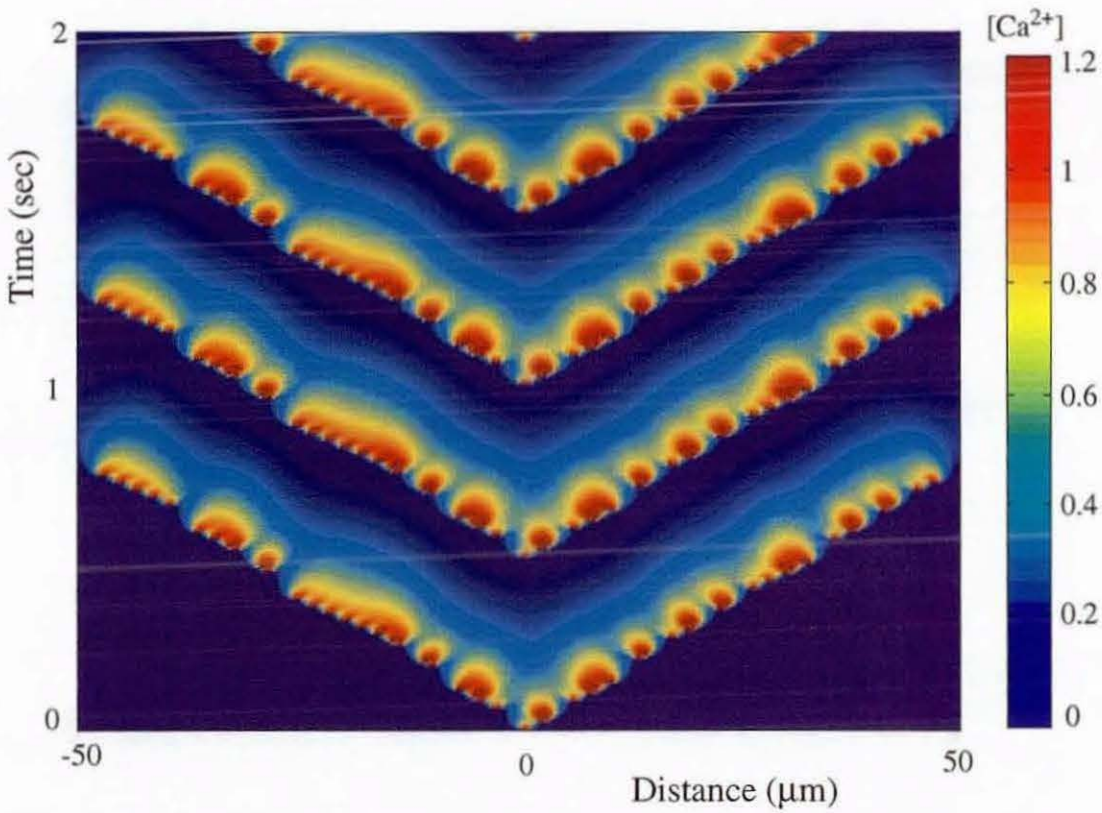


Figure 5.14: An example of periodic travelling wave moving out from the center of a one-dimensional FDF model with irregularly spaced release sites when $\epsilon = 0.4d$ and $R = 48$. Other parameters as in Figure 5.10.

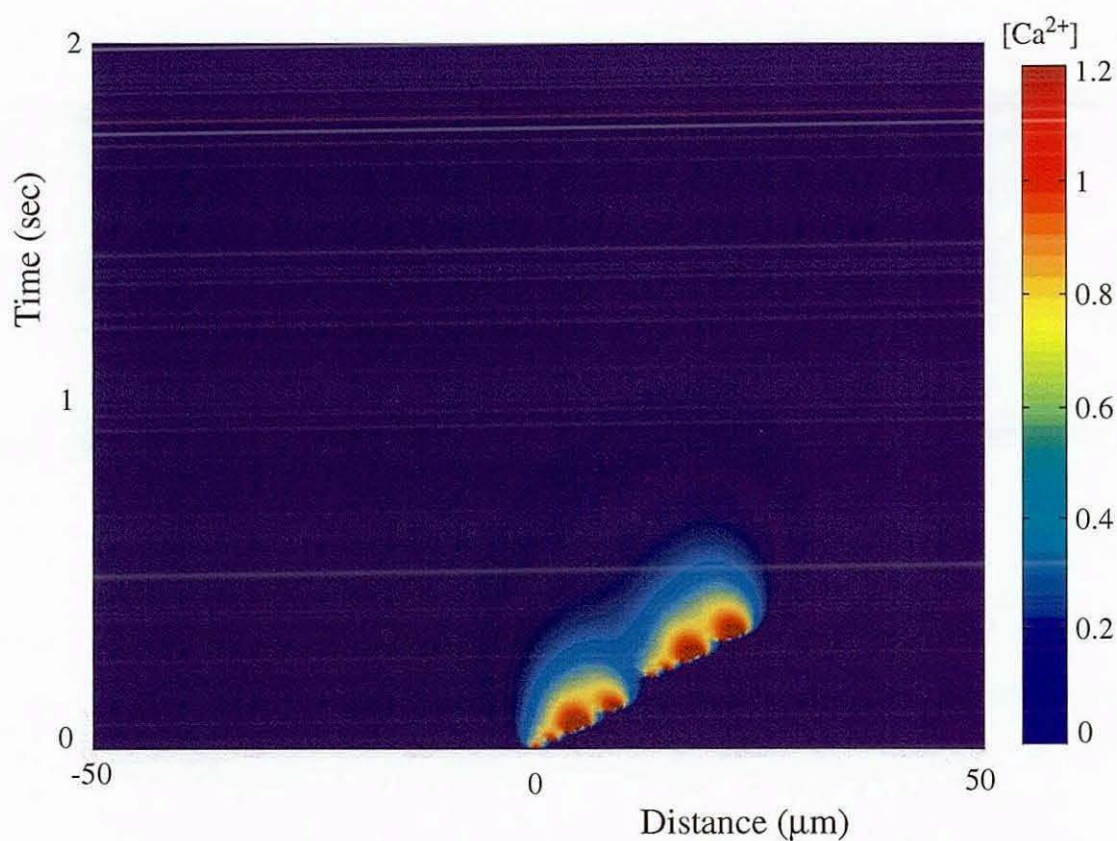


Figure 5.15: An example of travelling wave propagation failure in a one-dimensional FDF model with irregularly spaced release sites when $\epsilon = 0.6d$ and $R = 48$. Other parameters as in Figure 5.10.

site spacing d . An example of behaviour in the deterministic two-dimensional FDF model with an initially active release site in the center of the cell is shown in Figure 5.16. Here a sequence of snap shots shows nucleation of a wave and subsequent propagation of the wave through the cell. Repetitive nucleations occur in the middle of the cell with the period of oscillation largely determined by the refractory time-scale. Note that the octagonal shape of the wave (rather than a circular one) is due to the underlying square array of release sites. Animations of this figure and others may be found on the CD provided, where the corresponding file name is indicated in the caption of each figure (also see Appendix A.2). Different choices of initial conditions give rise to more complex patterns of wave propagation. For example, in Figure 5.17 we show spiral wave propagation, similar in structure to that observed in the work of Dallon and Othmer [41]. In common with our model these authors also consider a discrete/continuum model for signalling in *Dictyostelium discoideum* in which cells (rather than release sites) are treated as discrete points in a continuum of chemoattractant.

Now we consider a disordered distribution of release sites in two-dimensions, in the same manner as in the one-dimensional model. Figure 5.18 demonstrates an example of wave propagation in the presence of an irregular square lattice with an initially active single release site in the center of the cell. Comparing to Figure 5.16, the irregularity of the release sites causes the propagation of more circular waves with unequal activities. As expected, the degree of disorder in the distribution of release sites may change the pattern of wave propagation. To illustrate this we present two figures with different perturbations on the release site positions. Figure 5.20 shows an irregular wave that fails to propagate, whilst Figure 5.19 shows one that propagates and ultimately gives rise to a periodic spread of activity. In Figure 5.21 we show the propagation of spiral wave similar as in Figure 5.17, but with an irregular distribution of release sites.

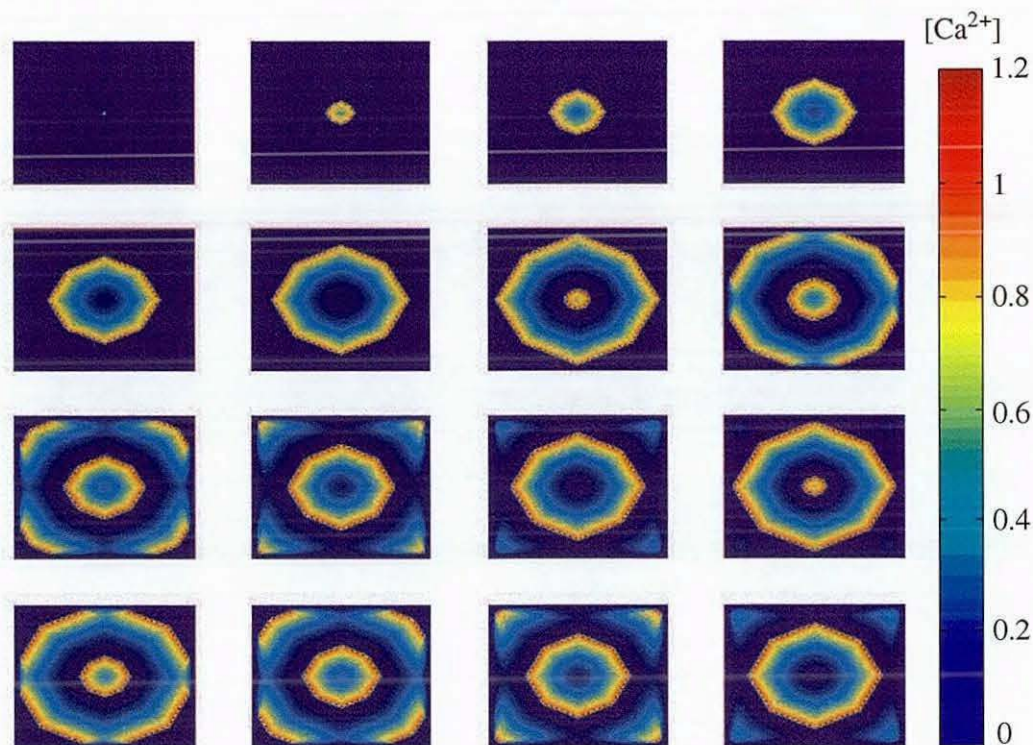


Figure 5.16: *Temporal sequence snapshots for the deterministic two-dimensional FDF model on the regular square lattice cell $120\ \mu\text{m} \times 120\ \mu\text{m}$. Other parameters as in Figure 5.9 and $u_{th} = 0.1$. Frames are presented every $0.1\ \text{s}$ starting in the top left corner and moving rightward and down. An initial seed in the center of the cell model leads to the formation and propagation of the well defined wave front. After the refractory time in $0.5\ \text{s}$ a new release event appears in the middle of the square lattice giving rise to a new propagating front of activity. (File: reg_prop.avi)*

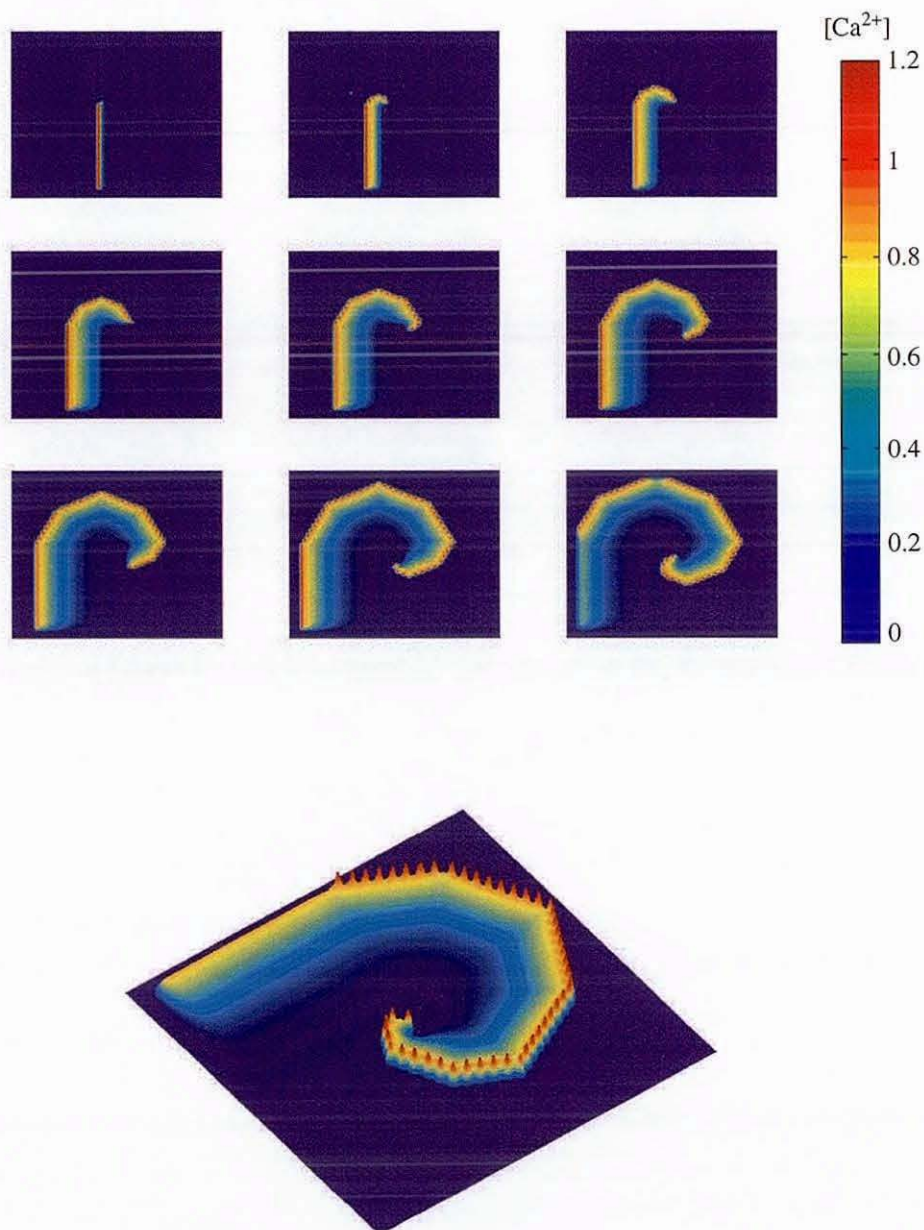


Figure 5.17: *Initiation of a spiral wave in the deterministic two-dimensional FDF model on the regular square lattice cell via activation of a line of release sites. Other parameters as in Figure 5.16. (File: reg-spiral.avi)*

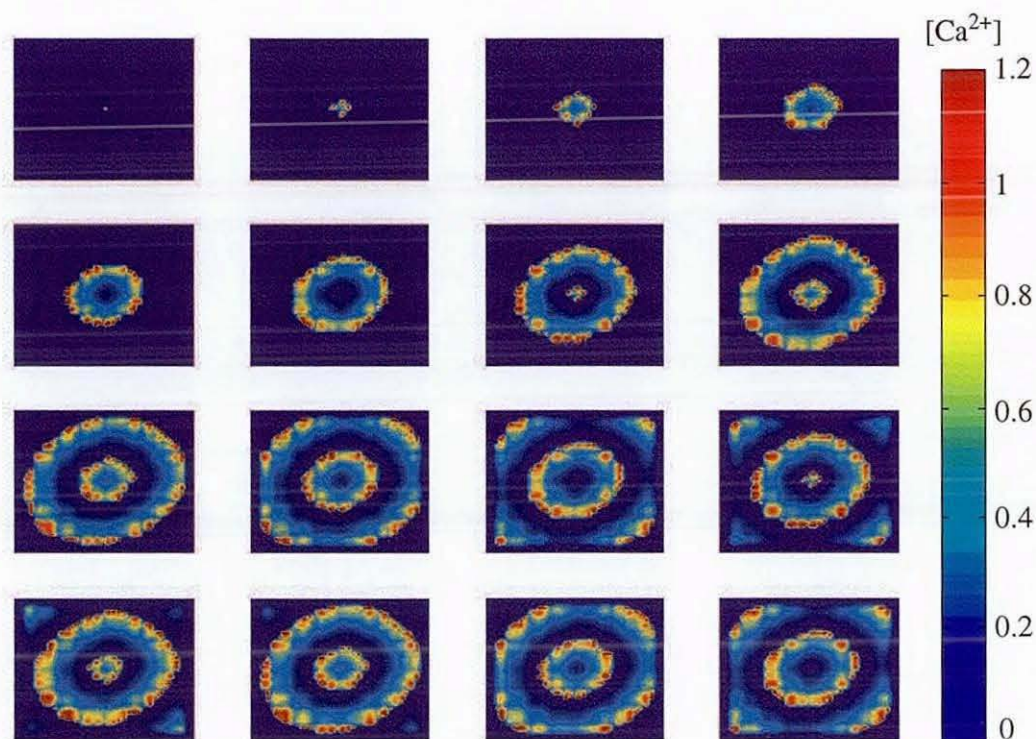


Figure 5.18: Temporal sequence snapshots for the two-dimensional FDF model on the irregular square lattice cell $120 \mu\text{m} \times 120 \mu\text{m}$ with $\epsilon = 0.4d$. Other parameters as in Figure 5.16. Frames are presented every 0.1 s starting in the top left corner and moving rightward and down. An initial seed in the center of the cell model leads to the formation and propagation of the periodic irregular circular wave front. (File: *irreg_prop1.avi*)

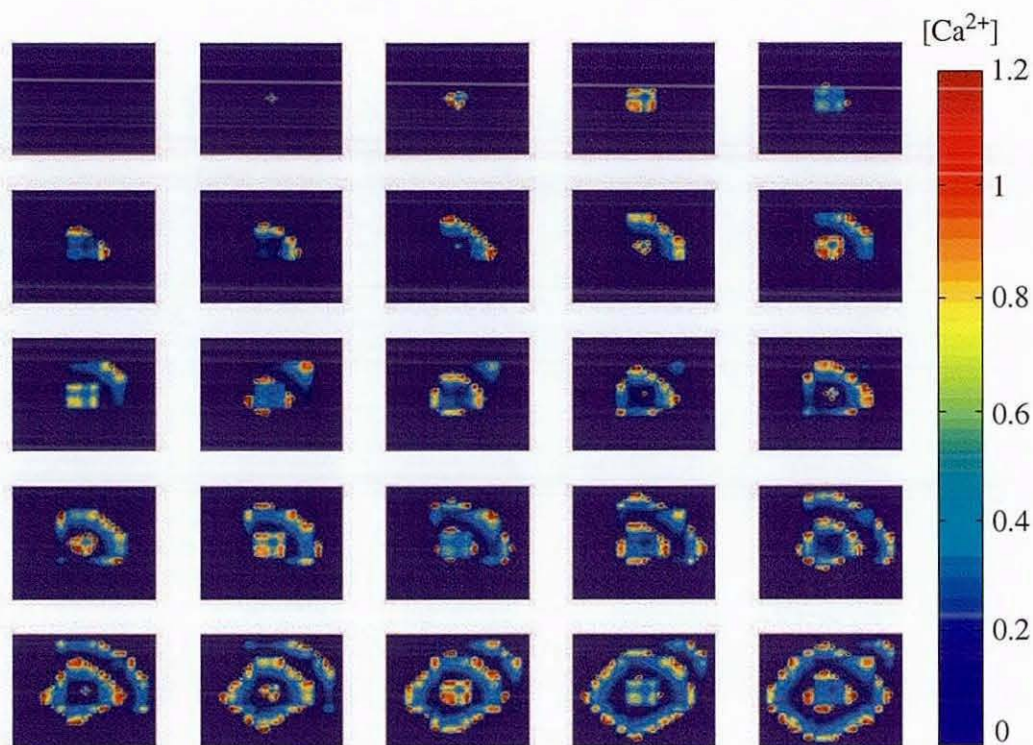


Figure 5.19: Temporal sequence snapshots for the two-dimensional FDF model on the irregular square lattice cell $120 \mu\text{m} \times 120 \mu\text{m}$ with $\epsilon = 0.6d$. Other parameters as in Figure 5.16. Frames are presented every 0.08 s starting in the top left corner and moving rightward and down. This example demonstrates the propagation and ultimate rise to a periodic spread of activity. (File: irreg_prop2.avi)

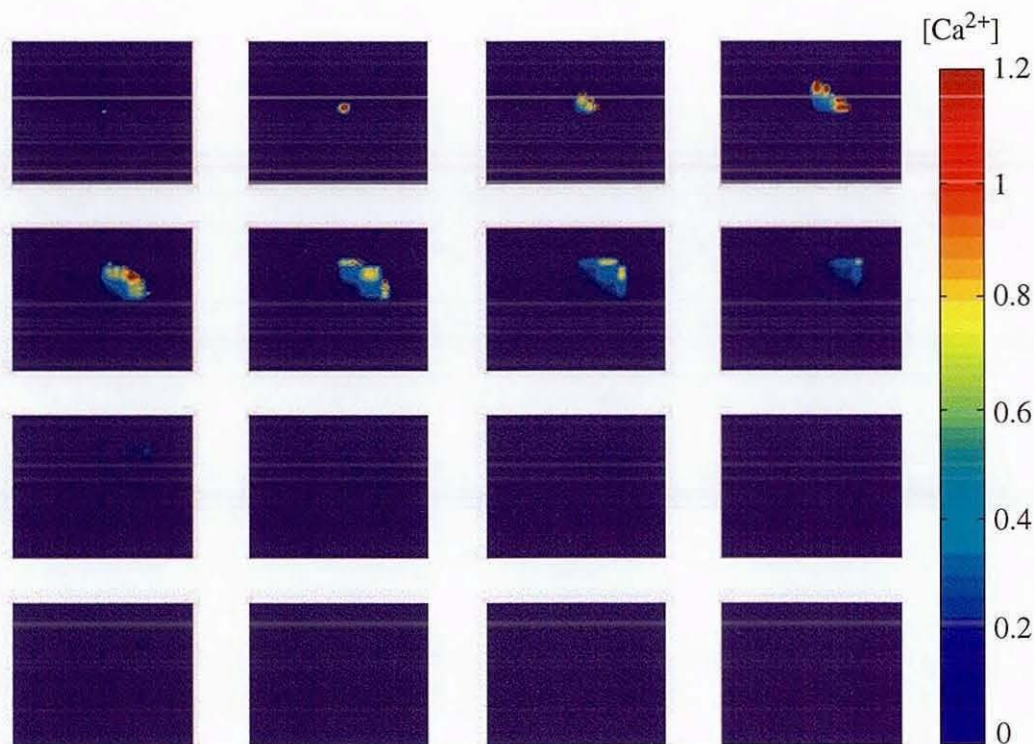


Figure 5.20: Temporal sequence snapshots for the two-dimensional FDF model on the irregular square lattice cell $120 \mu\text{m} \times 120 \mu\text{m}$ with $\epsilon = 0.8d$. Other parameters as in Figure 5.16. Frames are presented every 0.1 s starting in the top left corner and moving rightward and down. This example demonstrates the propagation failure in the model. (File: irreg_failure.avi)

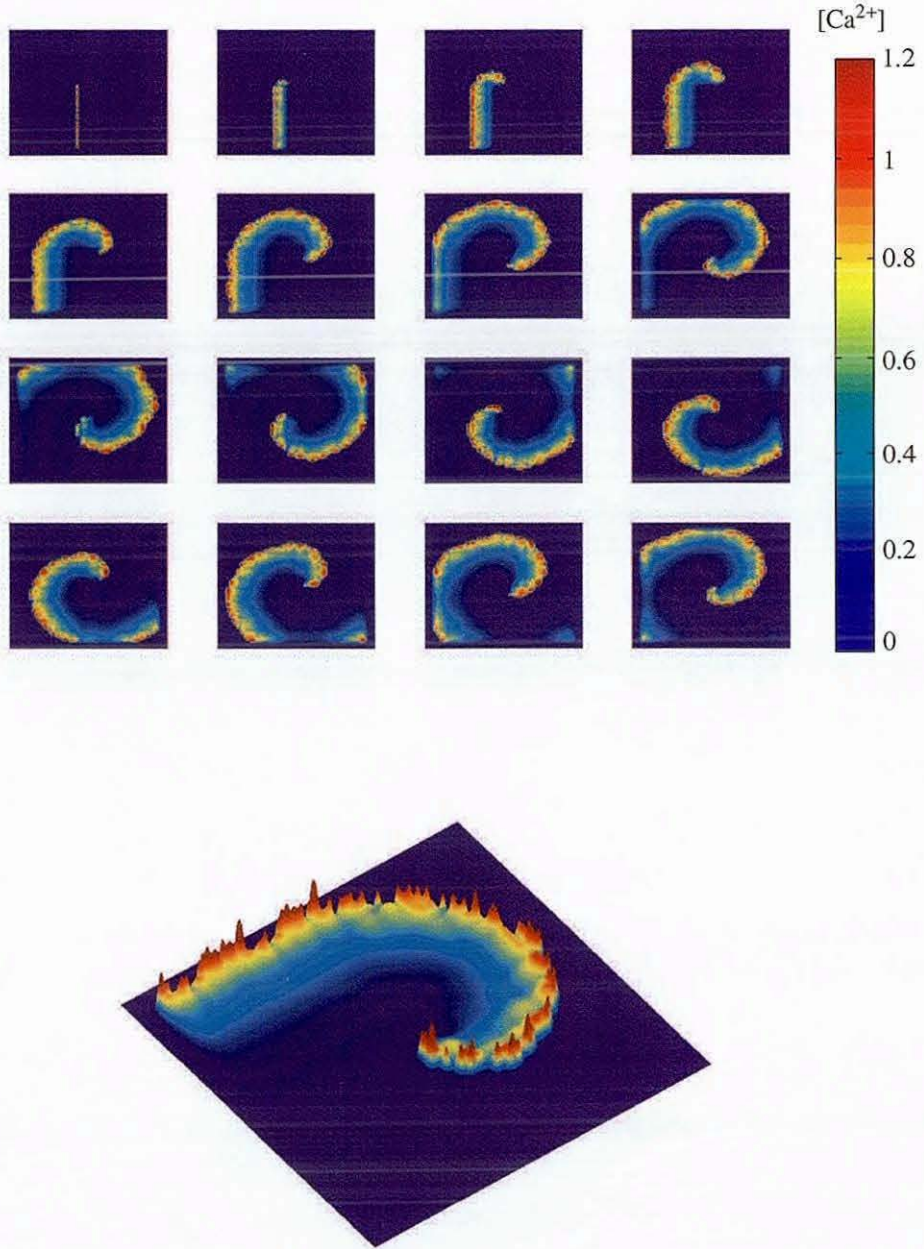


Figure 5.21: *Initiation of a spiral wave in the deterministic two-dimensional FDF model on the irregular square lattice with $\epsilon = 0.2d$. Other parameters as in Figure 5.17. (File: irreg_spiral.avi)*

Summary

In this chapter we have studied the generalised FDF model with a discrete distribution of calcium release sites. The discrete FDF model is still mathematically tractable and solutions that correspond to saltatory solitary and periodic travelling waves have been explicitly constructed. Moreover, we have shown that this minimal model of Ca^{2+} release can be further simplified. Assuming that release times occur on some regular lattice leads to a computationally inexpensive deterministic model where release events are calculated via a thresholding of the calcium profile at a release site. We have shown by direct numerical simulation that this computationally effective version of the FDF model provides an accurate representation of the original model. It is also natural and straightforward to generalise our FDF model to two dimensions. The model has been extensively numerically simulated in both one and two dimensions with regular and irregular distribution of release sites. Simulation results demonstrate that under parameter variation the model supports many patterns of wave propagation including regular and irregular solitary and periodic travelling waves, colliding waves, travelling fronts, spirals and abortive waves. Besides this, the simplified version of the FDF model is in an ideal form to be generalised to incorporate stochastic effects.

Chapter 6

Stochastic FDF model

Ca^{2+} signalling within and between living cells arises through complex mechanisms which have evolved to the specialised needs of particular cell types. It is important not to forget that the release of Ca^{2+} is controlled by the stochastic opening and closing of Ca^{2+} channels and the transitions between these two conductance states are random in time [31, 118, 124]. As we have previously emphasised, Ca^{2+} waves are composed of elementary stochastic release events Ca^{2+} (puffs or sparks) through single channels or several channels in a cluster [104, 105, 159, 163]. The stochastic nature of the release kinetics appears to play a significant role in initiation and propagation of the wave both in systems based on the IP_3R [107] and the RyR [30]. Hence, stochastic effects need to be taken into account when waves are modelled mathematically.

Most of the theoretical research on calcium waves has focused on deterministic models of intracellular Ca^{2+} release (see Chapter 2). Only relatively recently has the stochastic nature of intracellular Ca^{2+} release been considered [51, 52, 53, 87, 145, 146]. Keizer and Smith [87] and Falcke *et al* [53] have both emphasized the importance of modelling stochastic release kinetics when considering initiation and subsequent propagation of waves. Both have observed waves that abort in the presence of noise.

and also shown how noise may generate a spark-to-wave transition. Keizer and Smith [87] introduced a spatially one-dimensional stochastic model with a clustered distribution of RyR release channels for cardiac myocytes. The numerical simulation of their model requires combining the evolution of a nonlinear PDE with a continuous time Markov process describing the transition between the open, closed and several intermediate states of the RyR. The model of Falcke *et al* [53] considers a stochastic version of the DYK IP₃R model, but with channel clusters at lattice points coupled by *fast* diffusion. The assumption of fast diffusion and linearity of the equation for calcium transport allows an adiabatic elimination of the calcium dynamics in favour of a purely stochastic continuous time Markov process for the channel configurations of the IP₃R. A recent numerical study of the spark to wave transition in cardiac cells may be found in [75].

In this chapter we introduce a model of calcium release based upon a stochastic generalisation of the FDF threshold model. We show how this leads to a natural description of release events using a probabilistic rather than a deterministic update rule. Simulation results are presented for both a one and two-dimensional cell model. These simulations illustrate that stochastic calcium release leads to the spontaneous production of calcium puffs/sparks that may merge to form saltatory waves. Sufficiently large threshold noise is able to terminate a wave prematurely suggesting that for some critical noise level there is a non-equilibrium phase transition between propagating and abortive waves. A statistical analysis shows that the model exhibits properties consistent with behaviour of other models from the universality class of directed percolation [70]. In a two-dimensional cell model, we show that not only does the model support noisy circular and spiral waves as expected but that it can also exhibit a form of array enhanced coherence resonance (AECR) [69, 73, 178]. We find that coherent motion, in the form of simultaneous and periodic release of calcium from all stores, can be induced purely by noise.

6.1 One-dimensional stochastic model

The discrete-time FDF threshold model defined by equations (5.18), (5.21) and introduced in the previous chapter is in an ideal form to be generalised to incorporate stochastic effects. The simplicity of the underlying deterministic model means that the calcium profile can be solved for in closed form, without the need for assumptions such as fast diffusion. This obviates the need to numerically evolve a PDE to obtain calcium profiles. Moreover, the FDF threshold is a natural point at which to introduce a source of noise in the system. By avoiding a Markov process description of channel gating we side-step the need for computationally expensive Monte Carlo type simulations.

We consider the stochastic gating of receptor channels to give rise to an effective threshold that can be modelled under the replacement $u_{th} \rightarrow u_{th} + \xi$ where ξ is an additive noise term with distribution $\rho(\xi)$. The probability that $a_n(p) = 1$ is then given by

$$P(a_n(p) = 1) = P(u_n(p) > u_{th}) \prod_{m=1}^{\min(R,p)} P(u_n(p-m) < u_{th}), \quad (6.1)$$

where

$$P(u > u_{th}) = \int \rho(\xi) \Theta(u - u_{th} - \xi) d\xi \quad (6.2)$$

For convenience we choose $\rho(\xi) = f'(\xi)$ so that

$$P(u > u_{th}) = f(u - u_{th}) \quad (6.3)$$

In work by Izu *et al* [75] it has been argued that the probability of release per unit time follows a functional form given by $u^n/(K^n + u^n)$ with the Hill coefficient $n = 1.6$ and Ca^{2+} sensitivity parameter $K = 15 \mu\text{M}$. Moreover, recent work described in [36] shows that such functional forms can be derived from stochastic models of channel

clusters. This also suggests that natural choices for $f(u)$ are sigmoidal functions. Here we shall make the choice

$$f(u) = \left\{ \frac{1}{1 + e^{-\beta u}} - \frac{1}{1 + e^{\beta u_{th}}} \right\} (1 + e^{-\beta u_{th}}), \quad (6.4)$$

so that the probability of release is zero when $u = 0$ and tends to one as $u \rightarrow \infty$. In summary, the stochastic FDF model is defined by equation (5.21) with the $a_n(p) \in \{0, 1\}$ treated as random variables such that $P(a = 1)$ is given by (6.1). In Figure 6.1 we illustrate the release probability function $f(u - u_{th})$. Note, that in the limit $\beta \rightarrow \infty$, this function approaches a step function so that $P(u > u_{th}) = \Theta(u - u_{th})$ and we recover our original deterministic model. Thus we interpret β as a parameter describing the level of noise. For sigmoidal forms of f the noise distribution $\rho = f'$ is bell-shaped with the width of the bell controlled by β (see Figure 6.2). In this framework the refractory time-scale can also be thought of as being drawn from some distribution, since release events are no longer bound by the constraint that they be separated by at least τ .

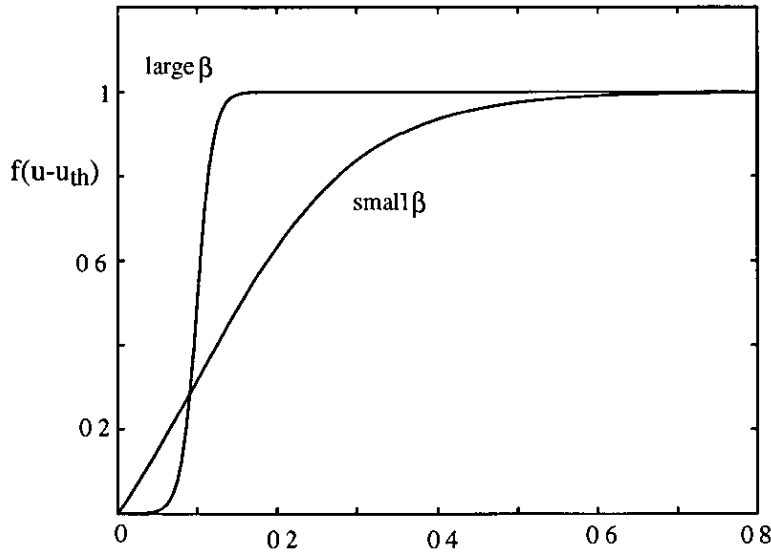


Figure 6.1 The release probability function $f(u - u_{th})$ suggested experimentally [75]

Here we illustrate the sort of behaviors that can be generated by this stochastic model

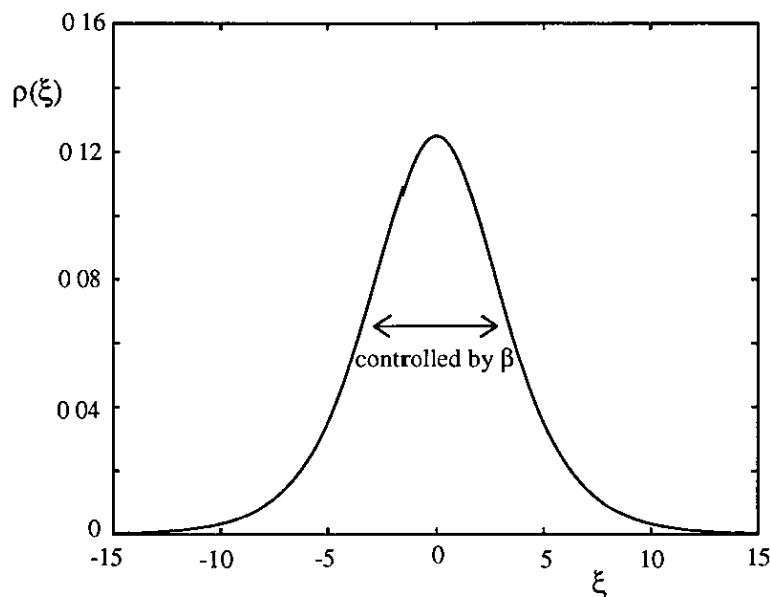


Figure 6.2 The function of noise distribution $\rho(\xi)$ for the given sigmoidal form of function f

A space-time density plot of a solitary lurching pulse arising in the deterministic limit $\beta \rightarrow \infty$ has already been shown in Figure 5.10 (for a regular array of release sites). As we have already noted this is qualitatively the same as that seen in experimental line scans, like that of Figure 5.11. Both these plots are useful for comparison with results from the stochastic model. In Figure 6.3 we plot the corresponding behaviour to Figure 5.10 in the presence of a finite amount of noise. Initial release from the central site leads to a local elevation of Ca^{2+} which initiates a propagating Ca^{2+} wave via activation of nearby sites, as in the deterministic case. However, the stochastic nature of the wave is evident from the fact that it does not propagate symmetrically away from the initial event. A similar type of behaviour can be observed in the deterministic FDF model with an irregular distribution of release sites (see Figures 5.14 and 5.15). However, in this instance (without threshold noise), initial data always leads to the same wave form, whereas in the stochastic FDF model this is not the case. Another example of a stochastic travelling wave is given in Figure 6.4.

for a higher level of threshold noise. Although rather well defined to start with the leftward propagating wave terminates at around 1.4 s. Activity in the wake of the primary stochastic front can also be sufficient to *prime* release sites for subsequent spark production, seen at around 1.6 s and again at around 3.2 s. It is also possible for propagating pulses to lead to the creation (in their wake) of oppositely propagating pulses. This so-called *back-firing* has been observed in a number of models (see for example [3, 58]) including the stochastic calcium release models of Keizer and Smith [87] and Falcke [53]. Simulation results demonstrate that this model captures the main qualitative features of the experimentally observed calcium puff/sparks and waves in a variety of cell types [25, 30, 107] (see, for example, the confocal linescan image of Ca^{2+} signalling in Figure 6.5).

6.1.1 Directed percolation

From Figure 5.9 it is easy to see that the deterministic FDF model can support travelling waves if the threshold for release is not too high, *i.e.*, if $u_{\text{th}} < u_{\text{th}}^*$, where u_{th}^* is defined by the saddle-node bifurcation where the fast and slow branches of $s = s(u_{\text{th}})$ coalesce. However, in the regime where $u_{\text{th}} < u_{\text{th}}^*$ it is possible that noisy versions of these waves will fail to propagate if noise levels are too high. This leads to the interesting possibility of a critical noise that defines a border between waves which *survive* or eventually go *extinct*. Indeed Bar *et al.* [6] have produced numerical evidence that the model of Falcke *et al.* [53] for stochastic calcium waves exhibits a non-equilibrium phase-transition belonging to the so-called directed percolation (DP) universality class.

DP is a $d + 1$ -dimensional dynamic process that is often treated as a testing ground for new ideas in non-equilibrium statistical mechanics [4, 110, 158]. Models within the DP universality class are interesting because they exhibit non-equilibrium phase transitions. In particular they can exhibit transitions from *absorbing* states, *i.e.*

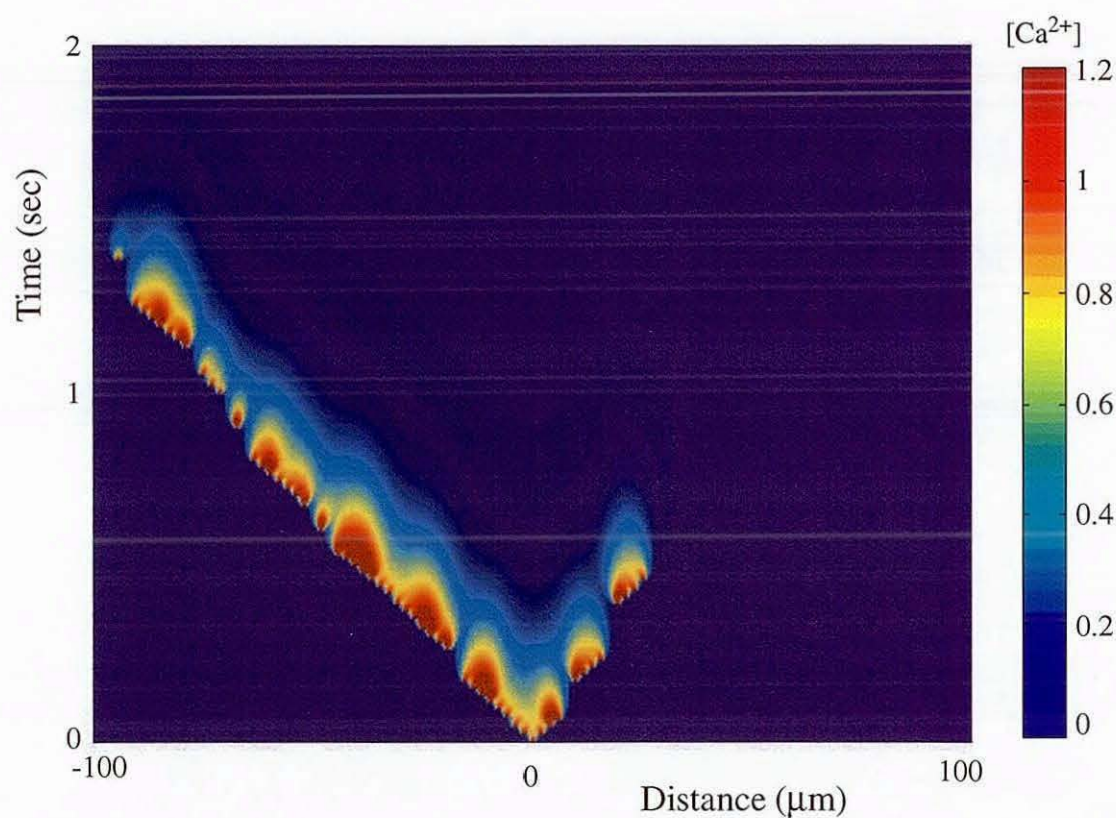


Figure 6.3: *Stochastic travelling wave for the model of Figure 5.10 with a finite amount of noise. Here $\beta = 70$.*

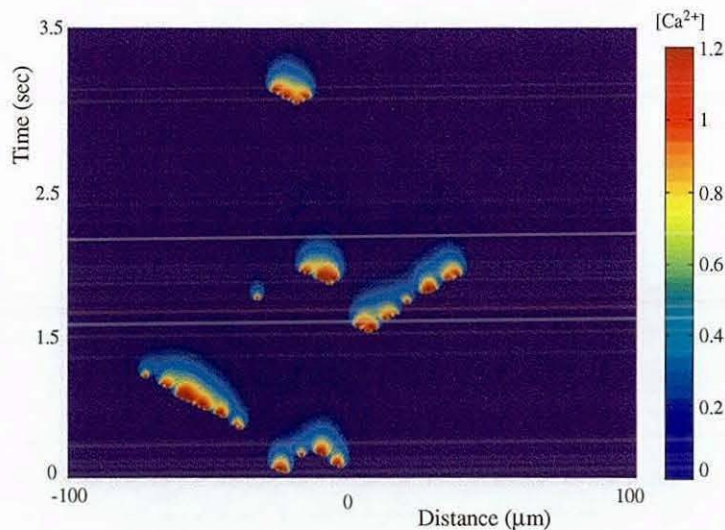


Figure 6.4: *Stochastic travelling wave for the model of Figure 5.10 with a finite amount of noise. Here $\beta = 10$.*

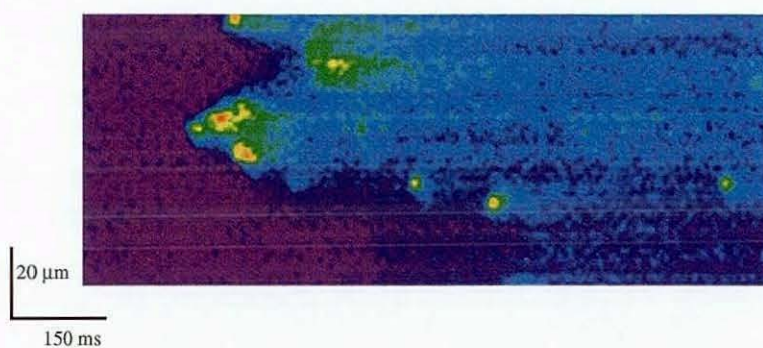


Figure 6.5: *The confocal linescan calcium image in immature *Xenopus* oocytes showing that puffs tend to occur randomly between different release sites [25].*

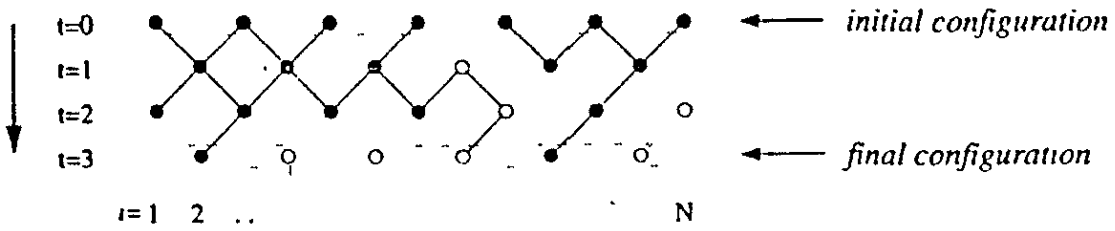


Figure 6.6 DP in 1+1 dimensions interpreted as a time-dependent stochastic process. Open (closed) bonds are indicated by solid (dashed) lines and black (white) circles denote active (inactive) sites. Starting from a fully occupied initial state the model evolves according to the dynamic rules of equation (6.5) and reaches a final state at $t = 3$.

configurations that can be reached by the dynamics but cannot be left, under variation of parameters controlling the level of noise in the model. As an example, a $(1 + 1)$ -dimensional directed bond percolation process is illustrated in Figure 6.6, where the lattice sites are enumerated horizontally by a spatial coordinate i and vertically by a discrete time variable t . A local binary variable $s_i(t)$ is attached to each site. $s_i = 1$ means that the site is active (occupied) while $s_i = 0$ denotes an inactive (unoccupied) site. We define a *cluster* in this context as a group of neighbouring occupied sites. On the contrary, if all nearest neighbours of an occupied site are inactive, this site is *isolated*. For a given configuration at time t , the next configuration at time $t + 1$ can be determined as follows. For each pair of bonds between the sites $(i \pm 1, t)$ and (i, t) two random numbers $z_i^\pm \in (0, 1)$ are generated. A bond is considered to be open (with probability p) if $z_i^\pm < p$, leading to the update rule

$$s_i(t + 1) = \begin{cases} 1, & \text{if } s_{i-1}(t) = 1 \text{ and } z_i^- < p, \\ 1, & \text{if } s_{i+1}(t) = 1 \text{ and } z_i^+ < p, \\ 0, & \text{otherwise} \end{cases} \quad (6.5)$$

Percolation theory deals with the clusters that are formed in this process. When the

probability p is very small, most sites are either isolated or form small clusters which contain a finite number of sites. Clearly, there is no continuous cluster between the two limits of the lattice. As p increases, there appear on the average more and more clusters of larger size. When a certain value of $p = p_c$ is reached, there suddenly appears the possibility of a cluster connecting continuously the two limits of the lattice. This cluster is usually called the *infinite cluster* in the percolation literature, even though the system is finite. For all values $p > p_c$, there is a continuous path of active sites exists connecting the extremes of the lattice (from past to future). A *phase transition* is defined to occur at the point where $p = p_c$ and there is a qualitative change in the system behaviour (from an absorbing state to an infinite cluster) as p is varied through p_c . Numerical simulations of the $(1+1)$ directed bond percolation process show that the temporal evolution of a DP process changes significantly at the phase transition. Typical space-time histories for random initial conditions and a single active seed are shown in Figure 6.7. For $p < p_c$ the number of occupied sites decreases exponentially until the system reaches the absorbing state (no occupied sites), whereas for $p > p_c$ there is a finite probability that the resulting cluster is infinite. At the critical point when $p = p_c$, the mean active site number decays very slowly and the critical cluster is generated with certain scaling properties. Precisely at the critical point the survival probability, $\Pi(t)$, that a wave initiated from a single site has not aborted after t time steps, is expected to scale asymptotically as $t^{-\delta}$, where δ is a universal scaling parameter (see [70] for a review). The analysis of the DP universality class is highly non-trivial and it has only been possible to obtain critical exponents for models in this class numerically. The best current estimate for δ comes from the work of Jensen [81], who finds that $\delta \sim 0.159464$.

According to the Janssen-Grassberger DP conjecture, any spatio-temporal stochastic process with short range interactions, fluctuating active phase and unique nonfluctuating (absorbing) state, single order parameter and no additional symmetries, should belong to the DP class. Since these are almost the defining characteristics of a minimal

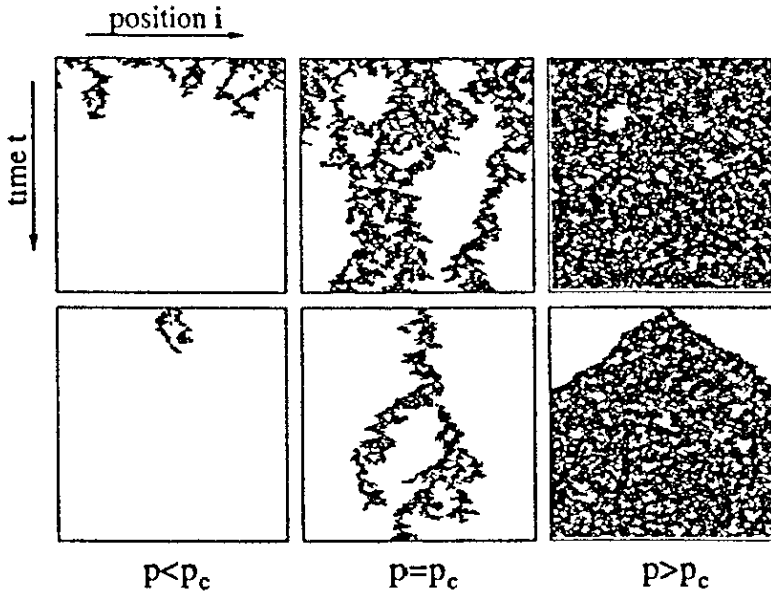


Figure 6.7 DP in 1 + 1 dimensions starting from random initial conditions (top) and from a single active seed (bottom)

model for stochastic calcium release we should not be too surprised if our stochastic FDF model also belongs to the DP class. To explore this possibility we consider the behaviour of our model under variation of the noise parameter β . We denote the critical value of β at the phase transition between propagating and abortive waves by β_c . To obtain a good estimate of the critical exponent δ we construct the effective exponent

$$\delta(t) = \frac{\ln[\Pi(rt)/\Pi(t)]}{\ln r}, \quad (6.6)$$

where $\ln r$ is the distance used for estimating the slope of $\Pi(t)$. For $\beta \neq \beta_c$, $\delta(t)$ will deviate from a straight line (in the large t limit) so that plots of $\delta(t)$ for various choices of β may be used to predict β_c . An estimate of δ is obtained by extrapolating the behaviour of $\delta(t)$ to $t^{-1} = 0$. In Figure 6.8 we plot $\delta(t)$ for various β , showing that for our choice of system parameters $\beta_c \sim 0.47$. In Figure 6.9 we plot the corresponding distribution of survival times $\Pi(t)$ for the activation process started from a single

site. Using our value of β_c we find $\delta \sim 0.159$, suggesting that our model does indeed belong to the DP universality class. Whether or not a DP transition will be seen in a living cell is another matter entirely. As pointed out by Hinrichsen [70], the size of a living cell is only a few orders of magnitude larger than the diffusion length, leading to strong finite size effects. Moreover, inhomogeneities as well as internal cellular structures are a source of disorder that may further complicate matters. To date there is no clear experimental evidence that there is a phase transition between survival and extinction of propagating calcium waves in living cells.

Till now we have illustrated the properties of the stochastic FDF model with one-dimensional studies in the regime where wave propagation is possible in the limit of zero threshold noise. In the next section we turn to two-dimensional studies and also explore the parameter regime where an initial disturbance could not propagate in the deterministic regime.

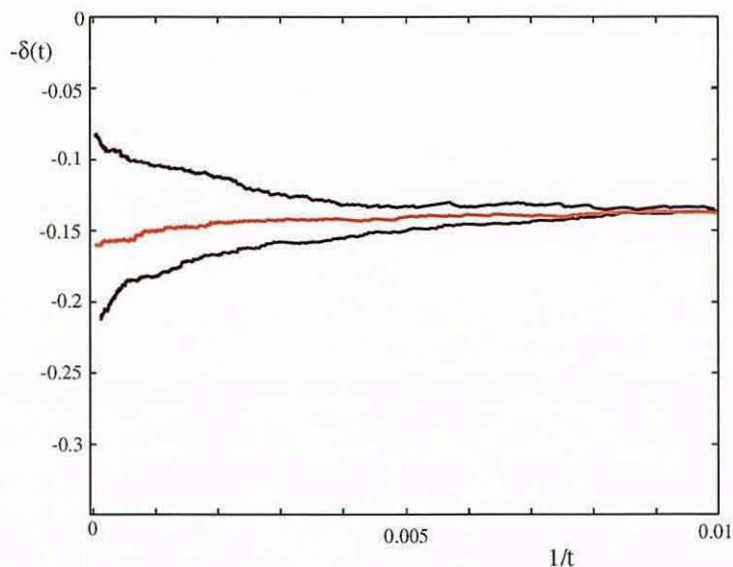


Figure 6.8: A plot of $-\delta(t)$ as a function of $1/t$ for three different level of threshold noise, $\beta = 0.49$ (upper curve), $\beta = 0.47$ (middle curve) and $\beta = 0.45$ (lower curve).

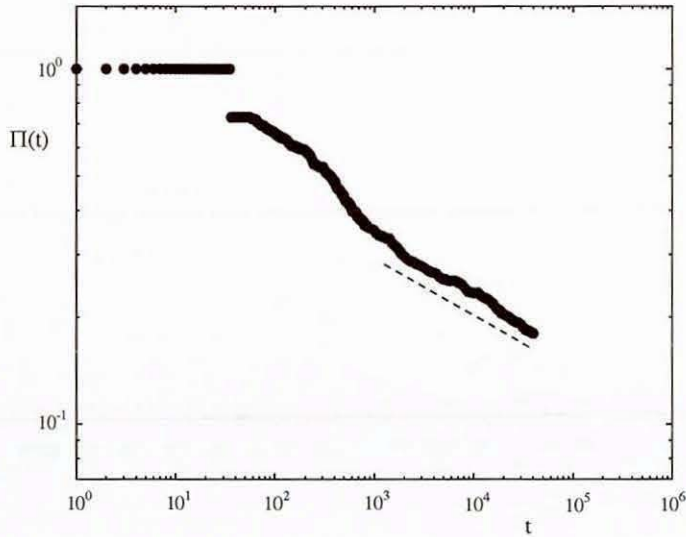


Figure 6.9: *The distribution of survival times for the stochastic FDF model at the critical noise defining the transition between propagating and abortive waves. For large t , $\Pi(t)$ scales as $t^{-0.159}$, indicating that our model belongs to the DP universality class.*

6.2 Two-dimensional stochastic model

In this section we consider a two-dimensional FDF model discussed in section 5.2.2 in the presence of threshold noise. For simplicity we focus only on a regular square lattice of release sites, with lattice spacing d . A single active site is placed in the centre of the square lattice at the beginning of simulations. An example of behaviour in the two-dimensional stochastic FDF model is shown in Figure 6.10. Here a sequence of snap shots shows nucleation of a circular front, subsequent propagation and the emergence of noisy spiral waves. These waves can be annihilated in collisions with other waves and created by spontaneous nucleation. The long time behaviour of the system is dominated by the interaction of irregular target and spiral waves. This is typical of dynamics in noisy spatially extended excitable systems. In fact the role of fluctuations for the generation and propagation of patterns in spatially extended

excitable media is a subject of increasing attention and can be traced back to work by Jung and Mayer-Kress [83, 84]. We note that both the stochastic FDF model and the Jung and Mayer-Kress (JMK) model describe the interaction of threshold devices with spatially decaying connectivity (fixed in the JMK model, but determined by the calcium profile in ours). In the JMK model noise is added to the state variable, whereas in the stochastic FDF model it is added to the threshold.

Importantly it is possible for noise to sustain spatio-temporal structures that could not otherwise occur. In this case a removal of all noise would lead to a deterministic system which could not support travelling waves. Since noise sustained target waves may collide with each other this typically limits their growth to a finite region, whose size is expected to decrease with increasing noise. Indeed the scale of noisy spiral waves has been shown to be dominated by the ratio of longitudinal (normal to the front of high activity) and the traversal (parallel to the front) speed of propagation [84]. As noise levels increase the transversal propagation speeds up, yielding a spiral wave with larger curvature. For increasing noise it is possible that the breakup of spirals and increased spontaneous nucleation of other spirals may destroy any coherent motion. However, it is also possible to see coherent motion for high levels of noise. In fact coherence can actually be enhanced in regions of high noise and it is possible to observe synchronized global release events. This type of behaviour has recently been termed *array enhanced coherence resonance* (AECR) and is typical of the way in which noise can lead to structured activity in spatially extended excitable systems [69, 73, 178]. In Figure 6.11 we show an example of this type of phenomenon in the stochastic FDF model. Here an initial disturbance leads to the propagation of a circular target wave. In the wake of the wave there is then subsequent release from a set of neighbouring sites. After this one sees near simultaneous release from a large number of sites. This process of simultaneous release repeats and at every stage recruits more and more stores. After only a few cycles of this process one sees an almost simultaneous release from all sites. This causes an oscillation in the global

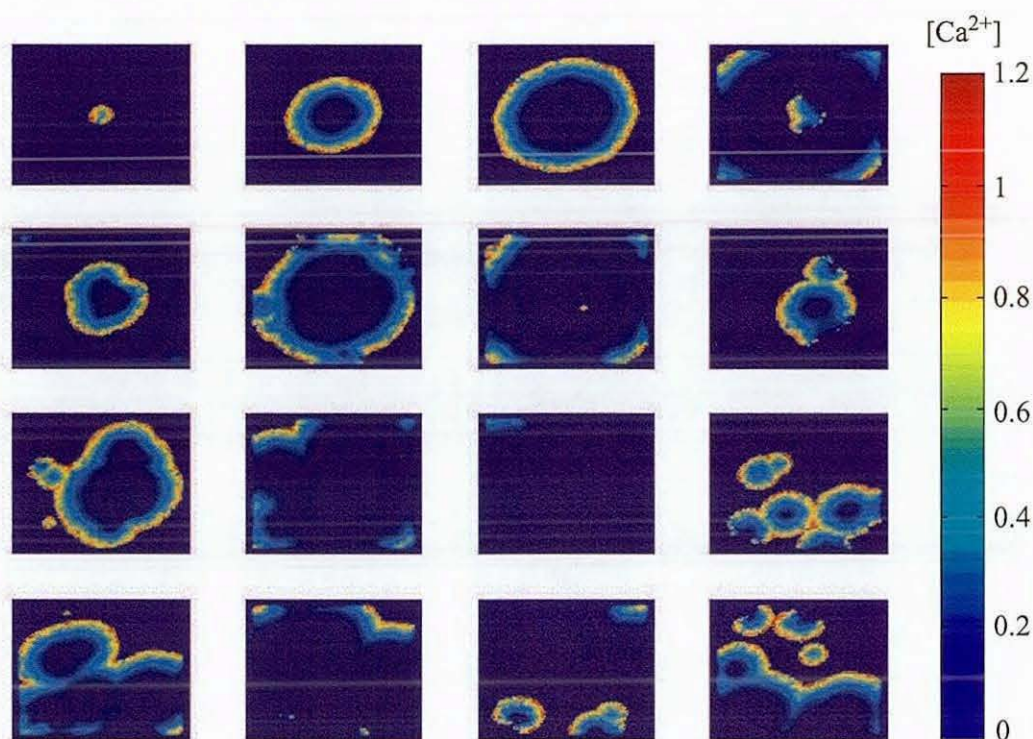


Figure 6.10: *Temporal sequence snapshots for the two-dimensional stochastic FDF model with $\beta = 100$ (low noise). Other parameters as in Figure 5.9. Frames are presented every 0.45 s starting in the top left corner and moving rightward and down. An initial seed in the center of the cell model leads to the formation and propagation of a circular front. Spiral waves form in the wake of the wave by spontaneous nucleation. These can be destroyed in wave-wave collisions and created by spontaneous nucleation. (File: noisy_prop.mpg)*

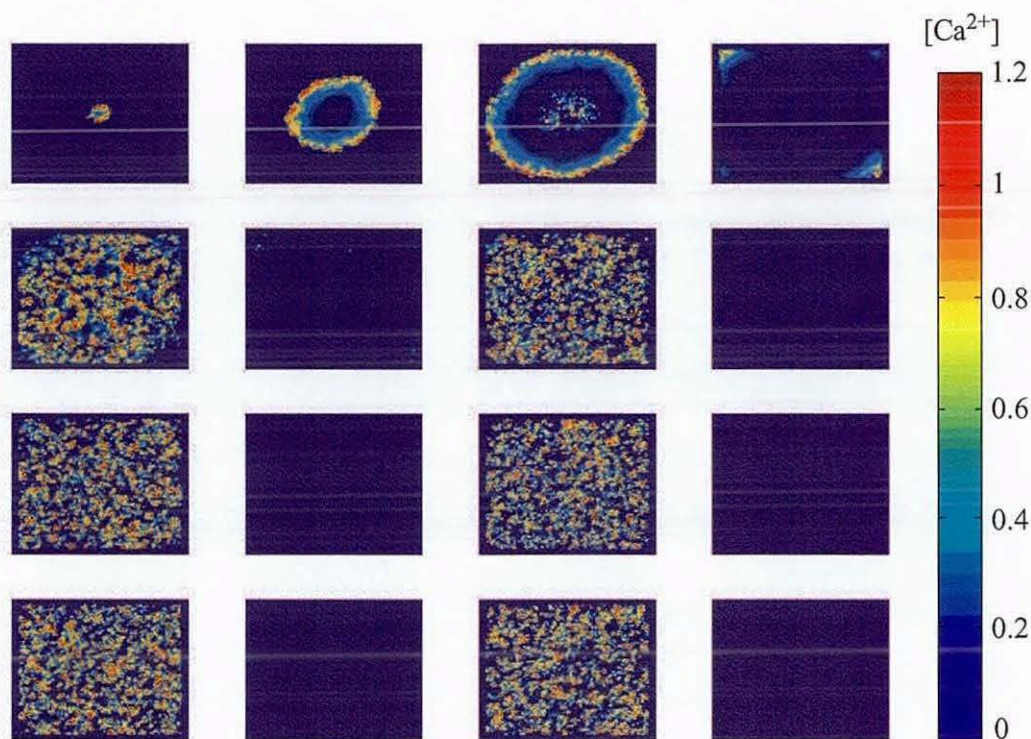


Figure 6.11: *Temporal sequence snapshots for the two-dimensional stochastic FDF model with $\beta = 10$ (high noise). Other parameters as in Figure 5.9. Frames are presented every 0.45 s starting in the top left corner and moving rightward and down. An initial seed leads to the formation of a circular travelling front. In the wake of the wave there is periodic and near simultaneous release from a large number of stores, typical of systems exhibiting array enhanced coherence resonance. (File: AECR.mpg)*

signal $U(t)$ defined by

$$U(t) = \frac{1}{|\Gamma|} \sum_{n=1}^{|\Gamma|} u(\mathbf{r}_n, t), \quad (6.7)$$

where $|\Gamma|$ is the number of release sites. An example of this oscillation is shown in Figure 6.12 for the data of Figure 6.11. In this figure we also plot the variation of $U(t)$ for the data presented in Figure 6.10. Although showing some level of periodic behaviour, it is clearly not as regular as that of the AECR example. The frequency of the AECR oscillation (as measured by variation in $U(t)$) increases monotonically with the noise level β^{-1} (above a cut-off below which AECR fails), and is shown in Figure 6.13.

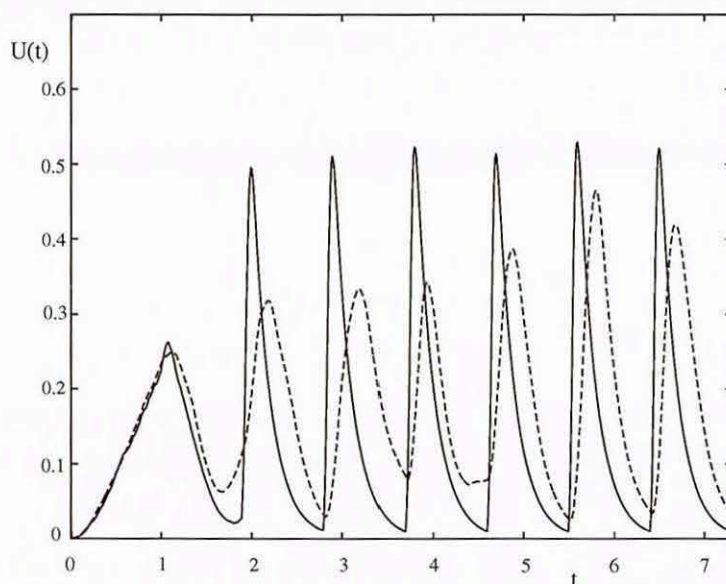


Figure 6.12: Plot of the global signal $U(t)$ for the data of Figure 6.11 (solid line) and also that of Figure 6.10 (dashed line).

We emphasize that the coherent motion illustrated in Figure 6.11 is induced purely by noise without an external periodic signal. This is very reminiscent of the behaviour of an excitable activator-inhibitor medium recently discussed by Hempel *et al.* [69]. They also consider a model with threshold noise (but with fixed Gaussian spatial

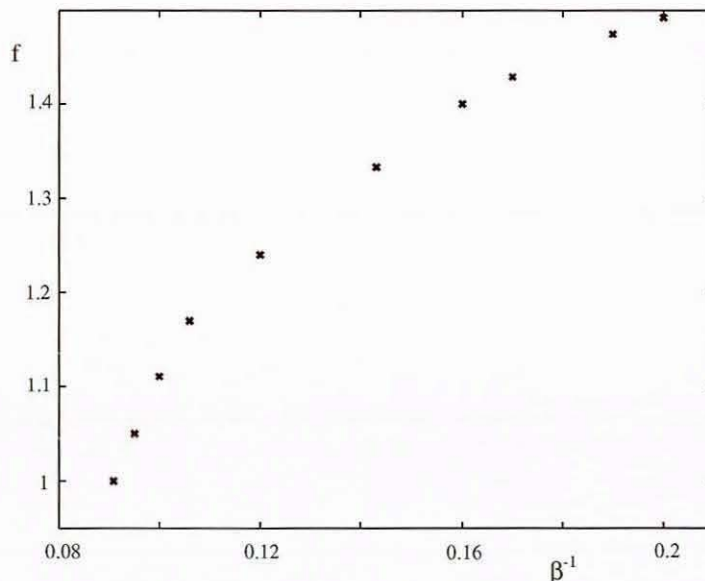


Figure 6.13: *Frequency f of oscillation of $U(t)$ for the system exhibiting AECR as a function of β^{-1} . Note that frequency increases monotonically with increasing noise levels. Parameters as in Figure 6.11.*

interactions) and note that when the nucleation time becomes much smaller than the intrinsic refractory time of the system, all cells fire and come back to rest essentially at the same time.

Finally we demonstrate that the stochastic FDF model may generate Ca^{2+} sparks and waves in the fashion similar to that seen in experiments. In Figure 6.14 we illustrate the visual similarity between our model results and those of Marchant and Parker [107]. Figure 6.14 (B) demonstrates the summation of activity from many stochastic puff sites generating regularly repetitive Ca^{2+} waves in *Xenopus* oocytes. The similar behaviour of wave propagation in the stochastic FDF model is shown in Figure 6.14 (A) for the low level of noise and by decreasing the refractoriness of the system. Experimental results in Figure 6.14 (C) illustrate an example of disruption of CICR resulting from Ca^{2+} diffusing between release sites, thereby functionally uncoupling individual sites. By increasing the level of noise and refractoriness in the stochastic

FDF model we observe the continued rise of individual puffs without generation of repetitive waves (Figure 6.14 (D)) similar to that in Figure 6.14 (C).

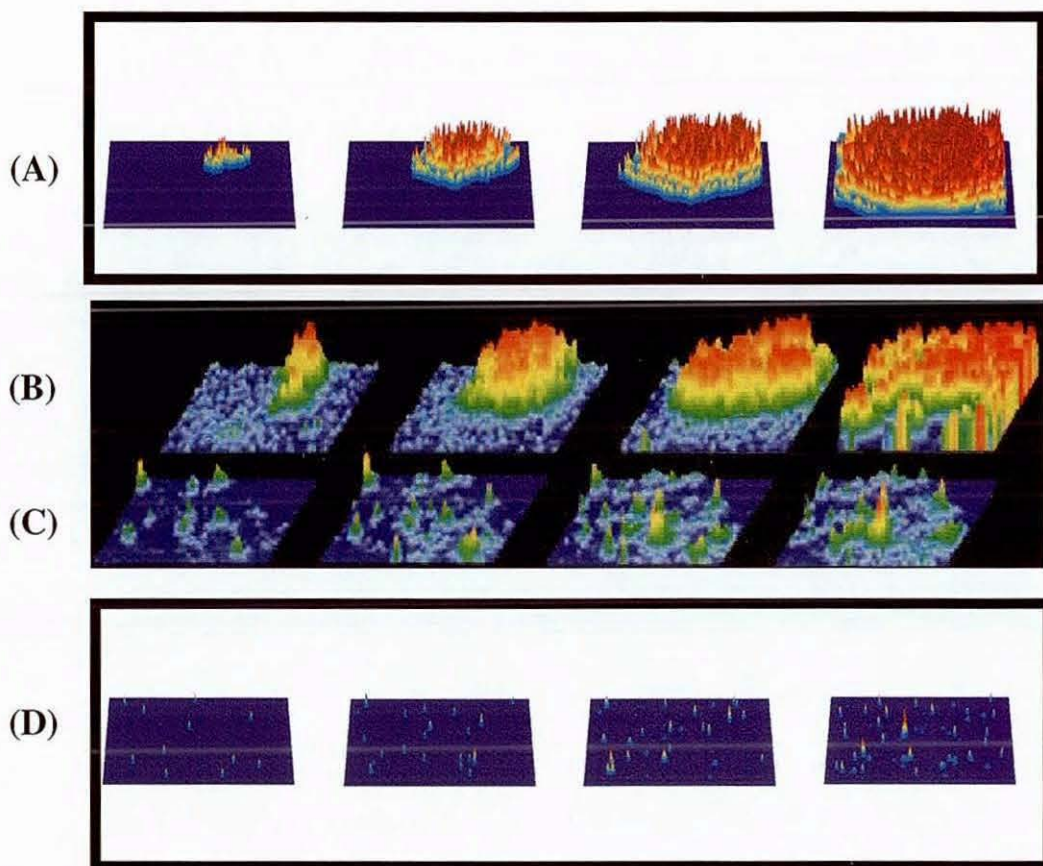


Figure 6.14: (B) and (C): Image sequences illustrating the patterns of Ca^{2+} liberation evoked in immature *Xenopus* oocytes by a photolysis flash of IP_3 . Each image sequence was captured at intervals of 0.1 s. (From [107]). (A) and (D): An example of generated Ca^{2+} puffs/sparks and propagating waves in the stochastic two-dimensional FDF model of Ca^{2+} release for $\beta = 70$, $R = 5$ and $\beta = 5$, $R = 50$ respectively. Frames are presented every 0.25 s.

Summary

In this chapter we have introduced a stochastic generalisation of the FDF model for

Ca^{2+} release One of the main advantages of our model is that it is computationally inexpensive. The stochastic nature of the release events is modelled by the inclusion of additive noise to the threshold. For high noise we observe spontaneous Ca^{2+} sparks and the possibility of global coherent signals in the form of simultaneous and periodic release from all sites. For low noise Ca^{2+} sparks can reinforce each other and propagate as waves. A statistical analysis of the model shows the interesting possibility of a non-equilibrium phase transition between propagating and non-propagating waves suggesting that the model belongs to the directed percolation universality class.

Chapter 7

Intercellular calcium waves

In many cell types, an initiated wave of increased intracellular calcium can spread from cell to cell to form an intercellular wave. Distinct from the previous chapters where we studied intracellular waves, this chapter considers some aspects of intercellular calcium signal propagation. In particular we are interested in the issue of wave propagation failure through the cell culture as a function of cell-cell coupling parameters. The focus is on the detailed biophysical DYK model discussed in Chapter 3 and the much simpler FDF model discussed in Chapter 4. Both of these models are extended to the tissue level by connecting model cells with gap junctions. In the case of the deterministic and continuous FDF model precise analytic statements about intercellular wave propagation failure are made as a function of gap junction permeability. The important effect of IP_3 regulation and transport on intercellular wave propagation is explored numerically for both FDF and DYK models, and in both instances is shown to severely restrict wave propagation. Moreover, comparisons between the two models show both qualitative and quantitative agreement, lending further support to the notion that the FDF model with an IP_3 dependent threshold provides a realistic caricature of the more complicated DYK model.

7.1 Mechanisms of intercellular calcium wave propagation

There is considerable experimental evidence to show that intracellular calcium signals can mediate intercellular communication by activating calcium signals in surrounding cells [19, 26, 42, 43, 59, 139, 140, 177]. It has been proposed that intercellular Ca^{2+} waves can serve to coordinate a multicellular response to a local stimulus. In some systems, such as the airway epithelium, the cell culture forms a thin layer of cells, connected by gap junctions. When a cell in the middle of the culture is mechanically stimulated, the Ca^{2+} in this cell increases quickly generating an intracellular wave. After a time delay of a second or so, the neighbours of the stimulated cell also show an increase in Ca^{2+} , and this increase spreads sequentially through the culture. An intracellular wave moves across each cell and after a short delay at the cell boundary initiates a similar intracellular wave in the neighbouring cell. Repetition of this process results in an intercellular wave moving across the culture. The distance the wave propagates appears to depend on the magnitude of the initial stimulus.

IP_3 can play the role of a second messenger, releasing Ca^{2+} from ER via IP_3R Ca^{2+} channels that are sensitive to both Ca^{2+} and IP_3 (discussed in detail in Chapter 2). Evidence also indicates that intercellular waves are mediated by the movement of IP_3 through gap junctions. When intercellular signalling of this type was first discovered, several qualitative models of the underlying mechanisms were proposed [19, 140, 150, 151, 153]. The main idea of these models is based on the passive-diffusion hypothesis which is shown as a schematic diagram in Figure 7.1. Mechanical stimulation of a single cell initiates the production of IP_3 in that cell and consequent release of Ca^{2+} . Some of this IP_3 moves through gap junctions to neighbouring cells, releasing Ca^{2+} from internal stores there. A small amount of IP_3 can stimulate a large release of Ca^{2+} via a positive-feedback process. The subsequent transport of

Ca^{2+} through neighbouring cells stimulates further release resulting in an intercellular Ca^{2+} wave. This hypothesis for the propagation of intercellular Ca^{2+} waves relies on the passive diffusion of IP_3 between cells via gap junctions.

It is important to emphasise that this diffusional hypothesis of wave propagation cannot fully account for the observed behaviour of all Ca^{2+} waves. For example, the

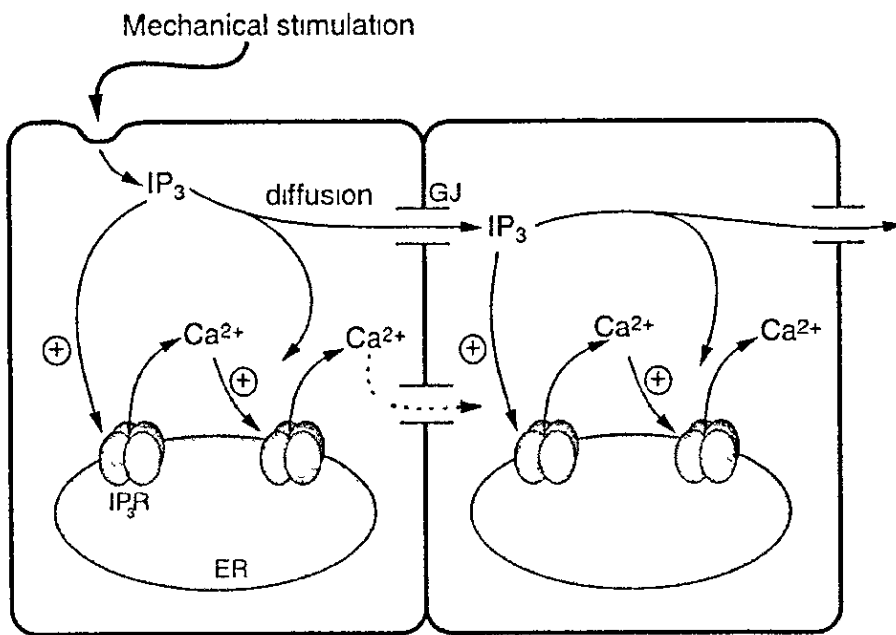


Figure 7.1 Schematic diagram of the passive diffusion hypothesis for the propagation of intercellular Ca^{2+} waves. GJ gap junction, IP_3R IP_3 receptor/ Ca^{2+} channel. The \oplus sign denotes Ca^{2+} -induced Ca^{2+} release. (From [140])

intercellular Ca^{2+} waves observed in the liver [125, 133] and the astrocyte networks of the central nervous system [38, 59] propagate over large distances and cannot simply rely on the diffusion of a messenger from a single point or cell. In these cases, it is likely that a process of regeneration is required to actively propagate the wave. This can be explained by the fact that both the calcium-releasing messenger IP_3 and calcium can participate in the gap-junctional mode transmission [32, 137]. In some

systems, an external signal is applied globally, so that IP_3 concentration increases in practically all cells. Under these conditions, calcium release in the presence of IP_3R and RyR calcium channels can be activated by the CICR mechanism (discussed in detail in Chapter 2). Thus, calcium influx through gap junctions may trigger calcium release in a cell acting as an intercellular mediator and in this way a regenerative intercellular calcium wave could spread.

CICR and gap-junctional calcium diffusion may be considered as a basic mechanism of intercellular calcium signalling. Recently, models based on a CICR/gap-junctional calcium diffusion mechanism have been developed for the formation of intercellular spiral waves of calcium in hippocampal slices [171], for the synchronisation of calcium oscillations in hepatocyte couplets [66] and for the propagation of calcium wavefronts in a model of calcium elevation through CICR coupled to cytoplasmic and gap-junctional calcium diffusion [67]. A common finding in these studies is the existence of a critical junctional calcium permeability which must be exceeded for intercellular wave propagation or synchronisation to occur. Our intention in the investigation of intercellular wave signalling is to begin with a simple mathematical model and focus on the conditions under which intercellular calcium waves can occur, and on how the occurrence and properties of the waves depend on the parameters of the calcium transport processes in the cell. The FDF model of intracellular calcium waves discussed in Chapter 4 can be considered as a good candidate to start the analysis of intercellular wave propagation.

7.2 Intercellular Ca^{2+} waves in the Fire-Diffuse-Fire model

A detailed analysis of the previously presented FDF model demonstrates the formation of intracellular travelling pulse of calcium propagating via the interaction of

CICR and calcium diffusion Considering multiple cells with gap-junctional connections and calcium fluxes across the gap junctions, we may study the characteristics of intercellular Ca^{2+} wave propagation in the FDF type model in terms of basic cellular parameters

7.2.1 Model equations

We introduce a linear cell array connected by the gap junctions shown in Figure 7.2. The change in the concentration of cytoplasmic calcium in the i -th cell, $u_i(x, t) = [\text{Ca}^{2+}]$, $i = 0, 1, \dots, n$, is given using a continuum FDF model in the following form

$$\frac{\partial u_i}{\partial t} = D \frac{\partial^2 u_i}{\partial x^2} + \sum_m \eta(t - T^m(x)) - \frac{u_i}{\tau_d}, \quad 0 \leq x \leq L, \quad (7.1)$$

where L denotes the length of a cell and x is mapped for each cell individually to the interval $(0, L)$. A detailed discussion of this equation can be found in Chapter 4

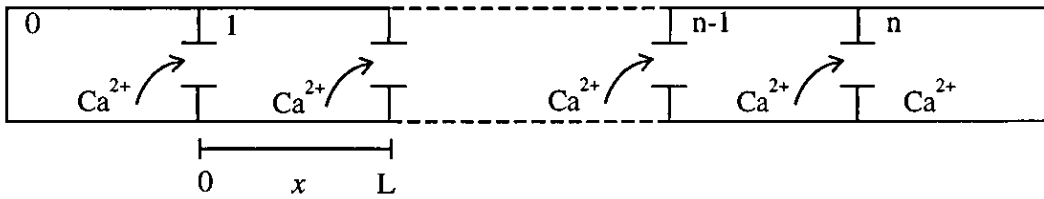


Figure 7.2 Linear array of cells of uniform length L , coupled by the gap junctions

We only mention here that the function $\eta(t)$ describing the shape of the Ca^{2+} puff is given by

$$\eta(t) = \sigma \Theta(t) \Theta(\tau_R - t), \quad (7.2)$$

where $\Theta(\cdot)$ is the Heaviside step function, σ is the strength of the Ca^{2+} puff and τ_R its duration. Note that in comparison to Chapter 4 we do not consider the puff shape to be normalised

The intercellular calcium fluxes through gap junctions are assumed to be proportional to the concentration differences across the gap junctions so that

$$-D \frac{\partial u_i}{\partial x} \Big|_{x=0} = F_c [u_{i-1}(L, t) - u_i(0, t)], \quad (7.3)$$

$$D \frac{\partial u_i}{\partial x} \Big|_{x=L} = F_c [u_{i+1}(0, t) - u_i(L, t)],$$

where F_c is the effective gap-junctional calcium permeability. We study the case of a solitary travelling pulse. From the analysis of Chapter 4 (section 4.2) we may write the following implicit equation for the speed of solitary travelling pulses in an infinitely long single FDF cell model as

$$\frac{u_{th}}{\sigma \tau_d} = \frac{\lambda_-}{\lambda_- - \lambda_+} [1 - e^{-\lambda_+ s \tau_R}], \quad (7.4)$$

where s denotes the speed of the wave, u_{th} is the FDF threshold and $\lambda_{\pm} = [s \pm \sqrt{s^2 + 4D/\tau_d}]/2D$. The bifurcation diagram in Figure 7.3 shows the speed of the travelling pulse as a function of the calcium puff duration τ_R . One notes that the speed of the stable solution branch is constant for almost the whole parameter region of τ_R where solitary travelling pulse can exist. This implies that large values of τ_R do not significantly influence the speed of the propagating pulse (at least for a large cell). In this respect we assume that the duration of a Ca^{2+} puff is large enough so that its shape can be approximated by the simple threshold condition $\sigma \Theta(u - u_{th})$. Thus, to carry out mathematical analysis of a single pulse, we consider the simplified equation for the concentration of cytoplasmic calcium in the form

$$\frac{\partial u_i}{\partial t} = D \frac{\partial^2 u_i}{\partial x^2} + \sigma \Theta(u_i - u_{th}) - \frac{u_i}{\tau_d}, \quad 0 \leq x \leq L, \quad i = 0, 1, \dots, n, \quad (7.5)$$

together with equations (7.3) for the intercellular calcium fluxes across the gap junctions.

7.2.2 Analysis of the model

The analysis of wave propagation in the model follows a similar approach to that of Hofer *et al* [67]. For convenience we non-dimensionalise the model equation by

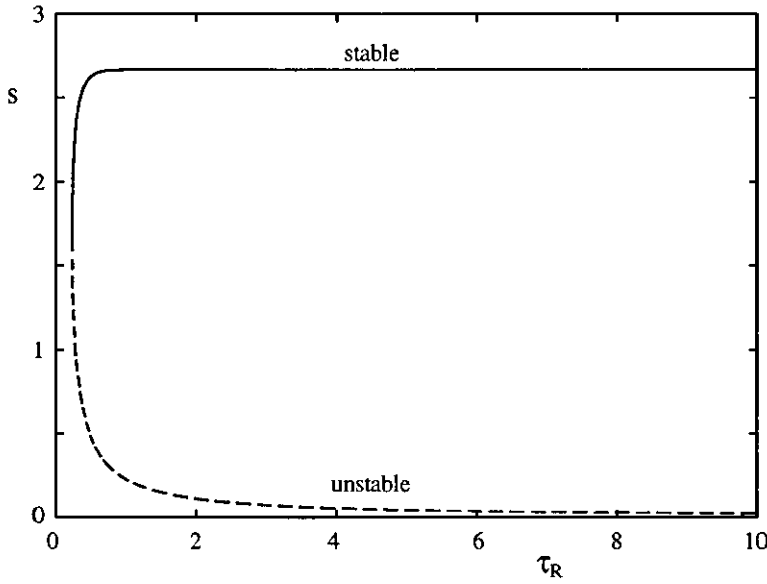


Figure 7.3 Speed of the intracellular travelling pulse in the FDF model as a function of the Ca^{2+} puff duration τ_R for the choice of parameters $D = 1$, $\tau_d = 1$, $\sigma = 1$ and $u_{th} = 0.1$

introducing the scaled time $\tau = t/\tau_d$, space $\xi = x/L$ and calcium concentration $\tilde{u} = u/u_{th}$. In the remainder of this chapter we will use the symbol $u(\xi, \tau)$ instead of \tilde{u} for the scaled concentration. Hence, the model takes the following form

$$\frac{\partial u_i}{\partial \tau} = \delta \frac{\partial^2 u_i}{\partial \xi^2} + \alpha \Theta(u_i - 1) - u_i, \quad 0 \leq \xi \leq 1, \quad (7.6)$$

$$-\delta \frac{\partial u_i}{\partial \xi} \Big|_{x=0} = p[u_{i-1}(1, \tau) - u_i(0, \tau)], \quad (7.7)$$

$$\delta \frac{\partial u_i}{\partial \xi} \Big|_{x=1} = p[u_{i+1}(0, \tau) - u_i(1, \tau)],$$

with the three dimensionless parameters

$$\delta = \frac{D\tau_d}{L^2}, \quad \alpha = \frac{\sigma\tau_d}{u_{th}}, \quad p = \frac{F_c\tau_d}{L}. \quad (7.8)$$

Provided that $\alpha > 1$ the kinetics of CICR and calcium removal given by $f(u) = \alpha\Theta(u-1) - u$ exhibit bistability. Figure 7.4 shows that a calcium signal is represented

by the transition from the rest state of low cytoplasmic calcium $u = 0$ to the excited state $u = \alpha$ which corresponds to the elevated calcium level following the triggering of CICR. We suppose that a local stimulus is applied in cell 0, at position $\xi = 0$,

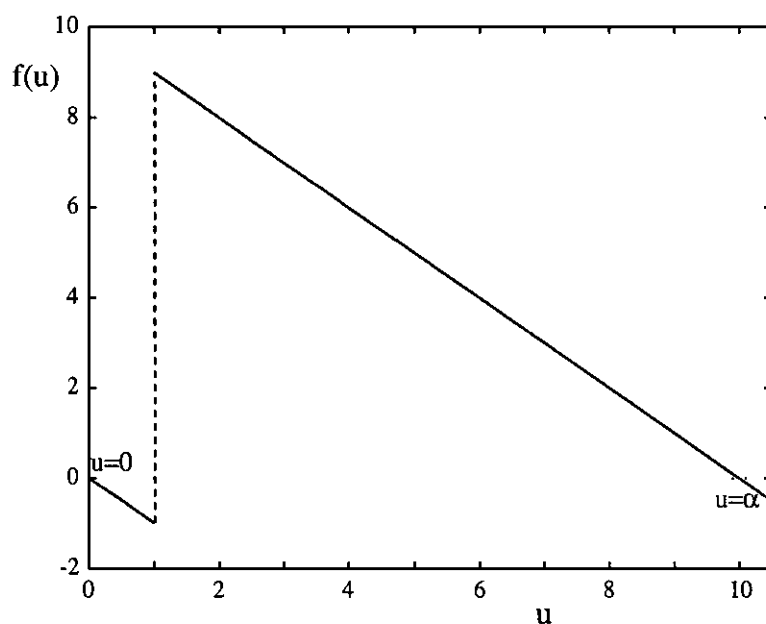


Figure 7.4. *Bistable kinetics of ER calcium release and removal $f(u)$ with step-function CICR when $\alpha = 10$*

$$u_0(0, \tau) = c_0, \quad \tau > 0, \quad (7.9)$$

and that initial calcium concentration in all cells is at the rest state, $u_i(\xi, 0) = 0$. If the stimulus triggers a regenerative intercellular calcium wave, it may be that all cells of the array become activated. However, it is also possible that signal propagation fails at some distance from the point of initiation, because the gap-junctional calcium influx into a cell becomes too small to excite CICR and limits the spatial range of the signal. Regenerative intercellular calcium waves and spatially limited calcium signals can be expressed in terms of the asymptotic behavior, $\tau \rightarrow \infty$, as

$$\lim_{t \rightarrow \infty} u_i(\xi) = \alpha \quad (7.10)$$

and

$$\lim_{i \rightarrow \infty} u_i(\xi) = 0 \quad (7.11)$$

respectively, where $u_i(\xi)$, $0 \leq i < \infty$, denote stationary concentrations. Thus, if the $u_i(\xi, \tau)$ approach the solution given by equation (7.11) after application of a local stimulus c_0 we observe the failure of regenerative intercellular wave propagation. Stationary solutions to equations (7.6) and (7.7) may satisfy equations (7.9) and (7.11), if calcium in cells up to cell m , $m \geq 0$, is above the CICR threshold, while in the remaining cells it is below

$$u_i(\xi) = \begin{cases} > 1, & 0 \leq i \leq m \\ < 1, & m+1 \leq i < \infty. \end{cases} \quad (7.12)$$

Letting $\partial u_i / \partial \tau = 0$ in equation (7.6) yields the following solution for the calcium profile

$$u_i(\xi) = \alpha_i + \beta_i e^{-\xi/\sqrt{\delta}} + \gamma_i e^{\xi/\sqrt{\delta}}, \quad 0 < \xi < 1, \quad (7.13)$$

where

$$\alpha_i = \begin{cases} \alpha, & 0 \leq i \leq m \\ 0, & \text{otherwise} \end{cases} \quad (7.14)$$

By connecting the solutions for neighbouring cells using equations (7.7), one may obtain a linear system of difference equations for β_i and γ_i in the form

$$\begin{pmatrix} \beta_i \\ \gamma_i \end{pmatrix} = A \begin{pmatrix} \beta_{i-1} \\ \gamma_{i-1} \end{pmatrix} \quad (7.15)$$

The matrix A results from evaluating equations (7.7) for calcium fluxes with equation (7.13) for $i < m$ and $i > m+1$ and is found as

$$A = \begin{pmatrix} (1 - \frac{\sqrt{\delta}}{2p})e^{-1/\sqrt{\delta}} & \frac{\sqrt{\delta}}{2p}e^{1/\sqrt{\delta}} \\ -\frac{\sqrt{\delta}}{2p}e^{-1/\sqrt{\delta}} & (1 + \frac{\sqrt{\delta}}{2p})e^{1/\sqrt{\delta}} \end{pmatrix} \quad (7.16)$$

The system of difference equations (7.15) can be explicitly solved for in closed form in terms of (β_0, γ_0) as

$$\begin{pmatrix} \beta_i \\ \gamma_i \end{pmatrix} = \mathcal{P} \begin{pmatrix} \lambda_-^i & 0 \\ 0 & \lambda_+^i \end{pmatrix} \mathcal{P}^{-1} \begin{pmatrix} \beta_0 \\ \gamma_0 \end{pmatrix}, \quad (7.17)$$

where λ_{\pm} are the eigenvalues of matrix A and \mathcal{P} is a modal matrix with linearly independent eigenvectors as its columns. The system of equations (7.17) is solved by

$$\beta_i = b_1 \lambda^i + b_2 \lambda^{-i}, \quad \gamma_i = \nu_1 b_1 \lambda^i + \nu_2 b_2 \lambda^{-i} \quad \text{for } 0 \leq i \leq m, \quad (7.18)$$

$$\beta_i = B_1 \lambda^i, \quad \gamma_i = \nu_1 B_1 \lambda^i \quad \text{for } m+1 \leq i \leq \infty, \quad (7.19)$$

with the following spectrum for A

$$\begin{aligned} \lambda_- &\equiv \lambda = T(1 - \sqrt{1 - 1/T^2}) \\ \lambda_+ &= 1/\lambda_- \end{aligned} \quad (7.20)$$

where

$$T = \cosh\left(\frac{1}{\sqrt{\delta}}\right) + \frac{\sqrt{\delta}}{2p} \sinh\left(\frac{1}{\sqrt{\delta}}\right) \quad (7.21)$$

We note that $T \geq 1$ and, therefore, it is straightforward to identify that λ is real and $0 \leq \lambda \leq 1$. The terms λ^{-i} are excluded from equations (7.19) because of the use of the boundary condition given by equation (7.11). Substituting the expressions for β_i and γ_i given by (7.18) into the system of difference equations (7.15) and solving this system in respect of ν_1 and ν_2 show that

$$\nu_1 = \frac{e^{-1/\sqrt{\delta}} - \lambda}{e^{1/\sqrt{\delta}} - \lambda} \quad \text{and} \quad \nu_2 = \frac{e^{-1/\sqrt{\delta}} \lambda - 1}{e^{1/\sqrt{\delta}} \lambda - 1}. \quad (7.22)$$

Using equations (7.18) and (7.19) with equation (7.13) the gap-junctional flux conditions (7.7) between cells m and $m+1$ and the left boundary condition (7.9) introduce a linear system of equations for b_1 , b_2 and B_1 as a function of m . This system is given in Appendix (A.4) and has a unique solution. In this way, the calcium profile

$u_i(\xi)$ given by equation (7.13) is found in terms of the model parameters with the spatial range of signal m to be determined. The relation (7.12) yields m such that the conditions to the solution

$$u_m(0) > 1, \quad u_{m+1}(0) < 1 \quad (7.23)$$

are satisfied. A critical situation occurs if the calcium concentration in cell $m+1$ just reaches the CICR threshold, i.e. $u_{m+1}(0) = 1$. This condition separates the case when the $(m+1)$ st cell is not excited from the case when it is excited. The expression for $u_{m+1}(0)$ is simply defined by

$$u_{m+1}(0) = B_1 \lambda^{m+1} + \nu_1 B_1 \lambda^{m+1}, \quad (7.24)$$

and is derived in Appendix A.4. For the spatially limited calcium signals $u_{m+1} < 1$ for some finite value of m . The other case is when $\lim_{m \rightarrow \infty} u_{m+1}(0) > 1$ and we expect the stimulus to induce nondecaying intercellular calcium waves. The critical condition separating the two cases is

$$\lim_{m \rightarrow \infty} u_{m+1}(0) = 1 \quad (7.25)$$

Taking the limit $m \rightarrow \infty$ in equation (7.24) (and correspondingly in equation (A.5)), we find that the condition for propagation depends on the cellular parameters α , p and δ and does not depend on the size of the initiating stimulus s . This critical condition is given by the following equation

$$\frac{\lambda(\cosh(\frac{1}{\sqrt{\delta}}) - \lambda)}{1 - \lambda^2} = \frac{1}{\alpha} \quad (7.26)$$

This equation implicitly defines a critical value of permeability, F_{critical} , which defines a border between propagating and non-propagating intercellular travelling waves. In fact condition (7.26) may be regarded as a special case of that considered by Hofer *et al.* [67] (who treat a more general scenario where gap junctions occupy a finite fraction of the size of each cell). As Figure 7.5 demonstrates the critical junctional permeability is a monotonically increasing function of the effective calcium diffusivity. In this figure the physical variables F_c and D have been plotted (rather than

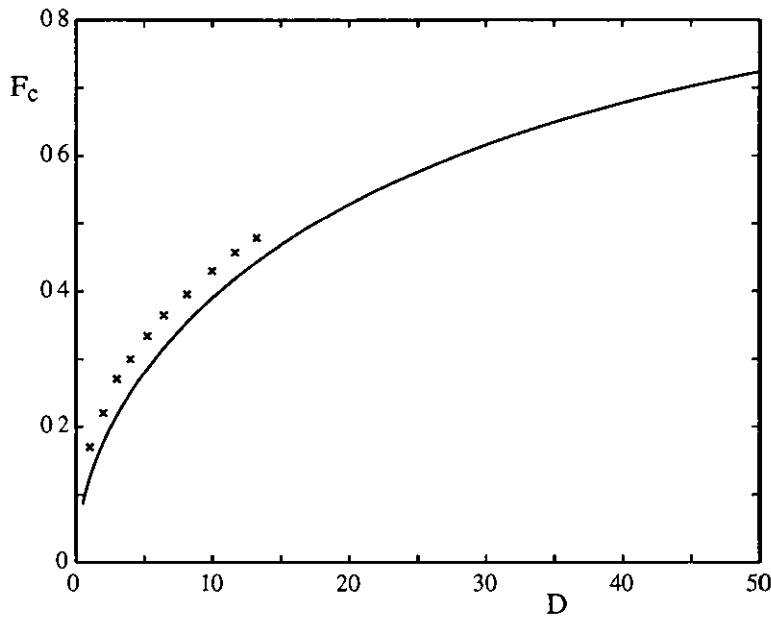


Figure 7.5 Critical gap-junctional permeability F_{critical} required for intercellular calcium wave propagation according to equation (7.26) for the choice of parameters $\sigma = 1$, $\tau_d = 1$, $u_{th} = 0.1$ and $L = 7.5$. Crosses indicate the results from numerical simulation of the full FDF model of intercellular waves with the same parameters and $\tau_R = 1$. Increasing agreement between numerical experiments and theory is found with increasing τ_R , as expected.

their non-dimensionalised counterparts, p and δ). It is worth remembering that the mathematical analysis for deriving the implicit equation (7.26) was only carried using an approximate puff shape. To test the validity of this approximation, the critical permeability in the full FDF model of intercellular Ca^{2+} waves (equation (7.1)) was found numerically. The results of this numerical analysis is shown by crosses in Figure 7.5. It can be seen that there is good, but not precise, agreement between the two models, justifying the assumptions of the simplified model. Figure 7.6 demonstrates the calcium concentration for intercellular waves in two cases of being just above or below the numerically found critical curve. For $F > F_{\text{critical}}$, a local stimulus triggers a regenerative intercellular calcium wave. It consists of a series of intracellular waves

punctuated by gap-junctional delays (Figure 7.6 a). The spatial range of propagation is potentially arbitrarily large, only limited by system boundaries, and the intracellular speed of propagation is constant. Very long-ranging calcium waves of constant speed were reported for systems in which PLC-activating agonist has been applied globally, and junctional calcium diffusion has been hypothesised as a coupling mechanism [38, 133, 179]. If $F < F_{\text{critical}}$, no regenerative intercellular waves exist and the signal does not propagate beyond the stimulated cell (Figure 7.6 b). Thus, regenerative calcium waves are triggered if the propagation condition is satisfied; otherwise the signal remains restricted to the first cell. Moreover, the permeability of Ca^{2+} at

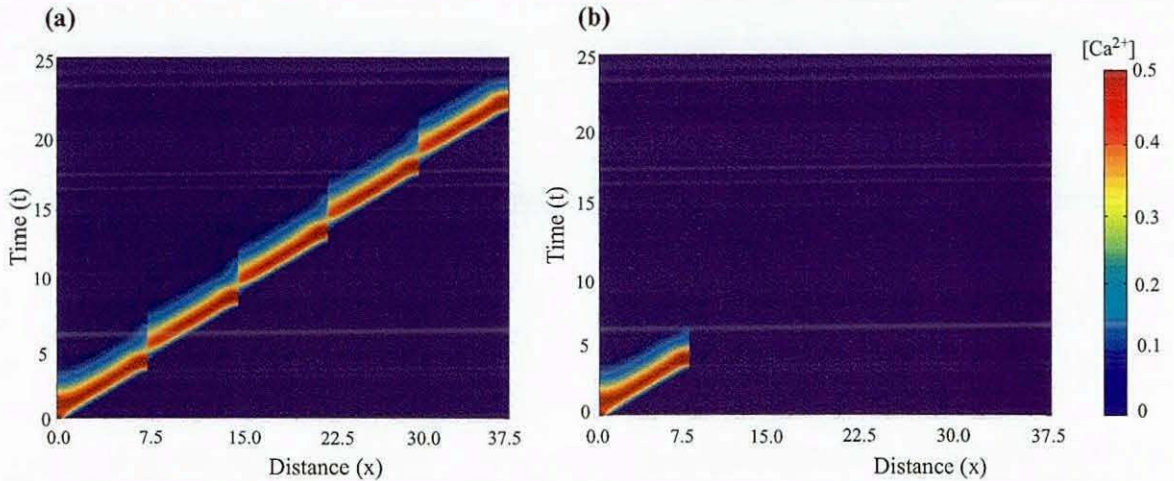


Figure 7.6: *Space-time plot of the calcium concentration in the FDF model of intercellular waves for the following parameters: $\sigma = 1$, $\tau_d = 1$, $\tau_R = 1$, $u_{th} = 0.1$, $L = 7.5$, $D = 1$ and (a) $F_c = 0.18$ (regenerative intercellular wave), (b) $F_c = 0.16$ (propagation failure). In both cases the left most cell was stimulated and the first 5 cells are shown.*

the gap junction controls a delay in the transmission of the wave between cells. In Figure 7.7 we plot the position of the wave front against time. The wave front is defined to be the place at which $[\text{Ca}^{2+}] = 0.3$. The rising portion of the curves correspond to the movement of the wave across a cell, whereas the flat portion correspond to the intercellular delay. As F_c decreases, the intercellular wave moves more slowly,

due principally to an increase in the intercellular delay

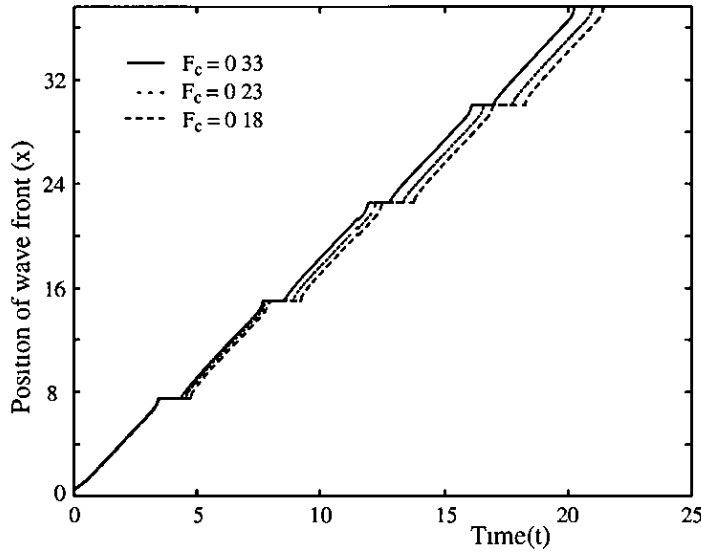


Figure 7.7 Position of wave front as a function of time for 3 different values of F_c in the FDF model. All other parameters are as in Figure 7.6

We have investigated a basic model of intercellular calcium signal propagation based on CICR via ryanodine receptors and gap-junctional calcium diffusion. This type of wave propagation cannot fully account for the observed behaviour of all Ca^{2+} waves. In the presence of IP_3R calcium release channels both the calcium-releasing messenger IP_3 and calcium can participate in the gap-junctional mode of transmission. The next section introduces some features of intercellular calcium waves in IP_3 sensitive systems.

7.3 Intercellular Ca^{2+} waves in the presence of mobile IP_3

Experimental evidence supports the hypothesis that mechanically-stimulated intercellular Ca^{2+} waves in some systems can result from the diffusion of IP_3 through

gap-junctions (see Figure 7.1). In this case a model based on the dynamic properties of IP_3 is essential for the representation of these processes. We assume that IP_3 moves through the culture by passive diffusion, moving from cell to cell via gap junctions, and decays at the same time. Then, within each cell equation for the cytoplasmic IP_3 concentration denoted by $p = [\text{IP}_3]$ is

$$\frac{\partial p}{\partial t} = D_p \frac{\partial^2 p}{\partial x^2} - \frac{V_p p}{k_\mu + p}, \quad (7.27)$$

where D_p is the diffusion coefficient of IP_3 , V_p is the maximal rate of IP_3 degradation, and k_μ is the concentration at which IP_3 degradation is half-maximal. The intercellular fluxes of IP_3 are assumed to be proportional to the concentration differences across the gap junctions, i.e.

$$-D_p \frac{\partial p_i}{\partial x} \Big|_{x=0} = F_p [p_{i-1}(L, t) - p_i(0, t)], \quad (7.28)$$

$$D_p \frac{\partial p_i}{\partial x} \Big|_{x=L} = F_p [p_{i+1}(0, t) - p_i(L, t)],$$

where L denotes the length of a single cell and p_i is the IP_3 concentration in cell i . F_p defines the gap-junctional IP_3 permeability coefficient.

The Ca^{2+} dynamics within each cell can be described by the reduced DYK model given by equations (2.16) and (3.14). The detailed derivation of these equations has been given in Chapter 3 with the parameter values listed in Table 2.1.

Similar to the IP_3 , the intercellular Ca^{2+} fluxes are assumed to be proportional to the concentration differences across the gap junctions

$$-D_c \frac{\partial c_i}{\partial x} \Big|_{x=0} = F_c [c_{i-1}(L, t) - c_i(0, t)], \quad (7.29)$$

$$D_c \frac{\partial c_i}{\partial x} \Big|_{x=L} = F_c [c_{i+1}(0, t) - c_i(L, t)]$$

with the gap-junctional calcium permeability F_c . We are now in a position to consider the effects of mobile IP_3 on intercellular calcium waves in both DYK and FDF based models.

7.3.1 Intercellular Ca^{2+} waves using the DYK single cell model

Before we analyse intercellular signal propagation in the presence of diffusing IP_3 we first consider the simpler case when the value of IP_3 concentration throughout the culture is constant. We assume that the wave spreads from cell to cell only by the Ca^{2+} fluxes given by equations (7.29). The extended analysis of intracellular oscillations and waves in the DYK model represented in Chapter 3 determines the IP_3 concentration, which is required for the wave generation in a single cell. This generated intracellular wave may propagate through the culture with propagation controlled by gap-junctional calcium permeability. From Chapter 4 we expect that a DYK model, with constant level of IP_3 throughout the tissue, will behave qualitatively like an FDF model with an appropriate IP_3 dependent threshold. This is illustrated in Figure 7.8, where the calcium concentration of intercellular waves is shown for two different values of calcium permeability. Figure 7.8 shows exactly the same qualitative features as that for the FDF single cell model, shown in Figure 7.6. For both single cell models intercellular calcium wave propagation is favoured with increasing gap-junctional coupling. The critical calcium permeability for wave propagation can be found numerically for the DYK single cell model and analytically for the FDF single cell model, using (7.26) and (4.20). In Figure 7.9 we plot the critical F_c dependence on the effective Ca^{2+} diffusivity for both single cell models. It is seen to be a monotonically increasing function. For completeness the wave front position as a function of F_c for the DYK model is shown in Figure 7.10. As expected the variation of permeability through the gap junctions causes a delay time in the transmission of the wave between cells, precisely of the type already found for the FDF model (see Figure 7.7).

We now consider the full dynamics for IP_3 concentration defined by equation (7.27), coupled to equation (2.16) describing the dynamics of intracellular Ca^{2+} . Both IP_3 and Ca^{2+} fluxes through the gap junctions are assumed to be proportional to the

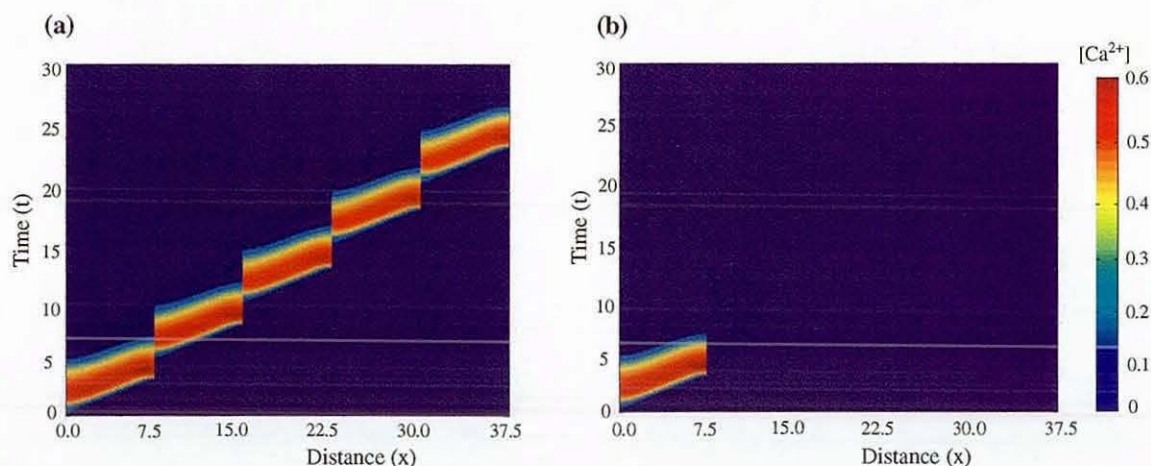


Figure 7.8: Space-time plot of the calcium concentration in the DYK model of intercellular waves with the constant IP_3 concentration $p = 0.25$ for the parameters given in Table 2.1, $L = 7.5$, $D_c = 1$ and (a) $F_c = 0.07$ (intercellular wave propagation), (b) $F_c = 0.04$ (propagation failure). In both cases the left most cell was stimulated and the first 5 cells are shown.

concentration differences, given by equations (7.28) and (7.29) respectively. In Figure 7.11 we illustrate the effect of varying the gap-junctional IP_3 permeability on the system behaviour. This plot demonstrates that arrival time of the propagating intercellular wave (at a cell boundary) is sensitive to changes in F_p and a decrease in this parameter leads to a decrease in wave speed or ultimately to propagation failure. This is in qualitative agreement with the work of Sneyd *et al.* [150] for the analysis of intercellular waves in the Atri model [2].

The bifurcation diagram of the reduced DYK model in Figure 3.3 shows the existence of a stable limit cycle for an intermediate range of IP_3 concentrations. Thus, if the IP_3 concentration is steadily increased in all cells, the cells within a specific physiological range of IP_3 concentrations will exhibit Ca^{2+} oscillations. This is clearly seen in space-time plot of the calcium concentration in Figure 7.12. The left most cell was stimulated by IP_3 and the first five cells are shown. The decrease in gap-junctional

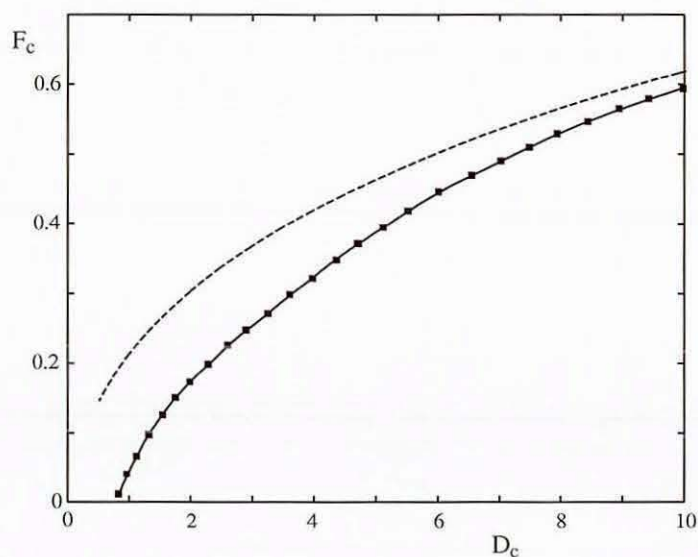


Figure 7.9: The critical gap-junctional permeability required for intercellular calcium wave propagation found numerically for the DYK single cell model (solid curve) and analytically for the FDF single cell model (dashed curve) with constant IP_3 concentration $p = 0.25$ and $k = 0.13$ in equation (4.20).

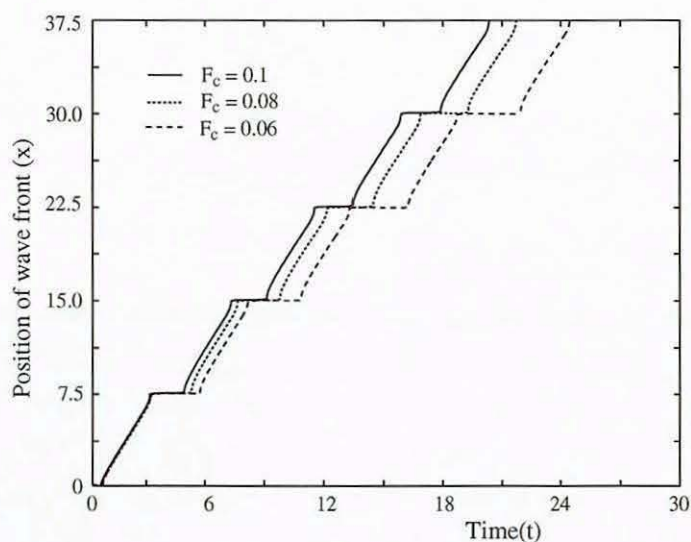


Figure 7.10: Position of wave front (defined to be where $[Ca^{2+}] = 0.3$) as a function of time for three different values of F_c in the DYK model. All other parameters are as in Figure 7.8.

IP_3 permeability makes it difficult for IP_3 to spread through the system causing failure of an intercellular wave. We demonstrate this in Figure 7.13.

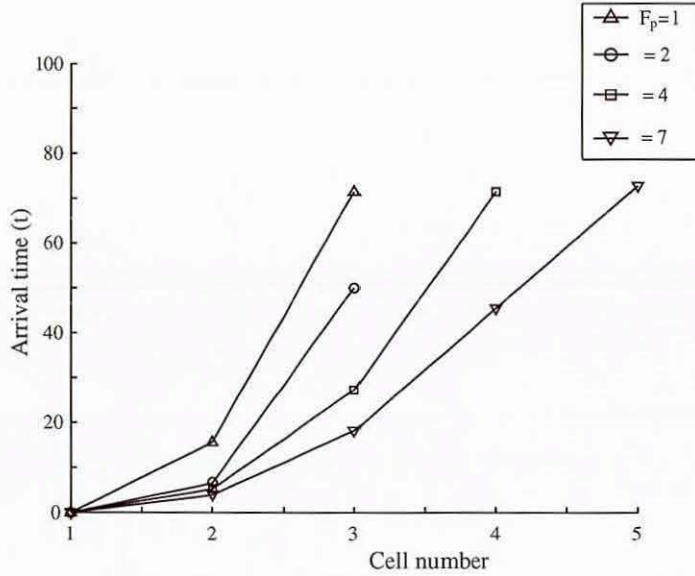


Figure 7.11: *Arrival time of wave in the DYK model for four different values of F_p for the parameters given in Table 2.1 and $L = 7.5$, $D_c = 1$, $F_c = 0.2$, $D_p = 15$, $V_p = 0.01$, $k_\mu = 5$.*

7.3.2 Intercellular Ca^{2+} waves using the FDF single cell model

We now consider the FDF model defined by equation (7.1) together with (4.4) (for periodic travelling wave) and (4.20) and coupled to equation (7.27) describing the dynamics for cytoplasmic IP_3 concentration. Intercellular fluxes of both Ca^{2+} and IP_3 are assumed to be proportional to the concentration differences across the gap junctions and given by equations (7.3) and (7.28) respectively.

In Figure 7.14 we illustrate how the system behaviour depends on the variation in the gap-junctional IP_3 permeability. As for the DYK model (Figure 7.11), this plot demonstrates that the speed and range of propagation are sensitive to changes in

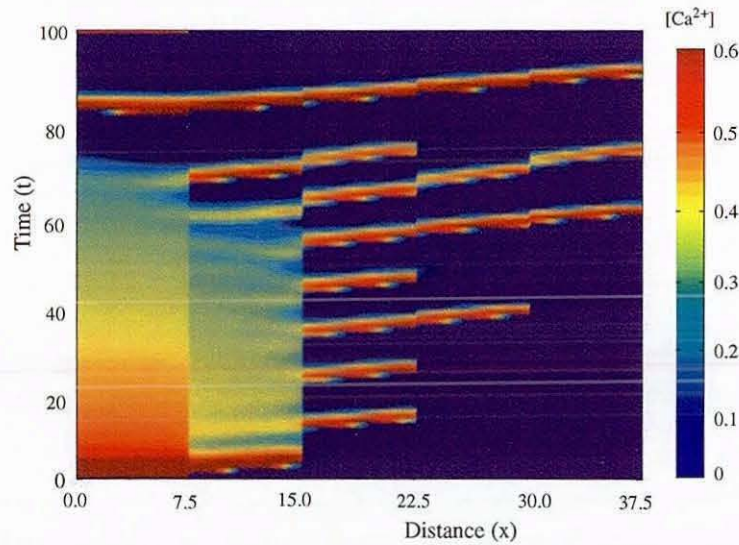


Figure 7.12: *Space-time plot of the calcium concentration in the DYK model of inter-cellular waves for the parameters in Figure 7.11 and $F_p = 7$.*

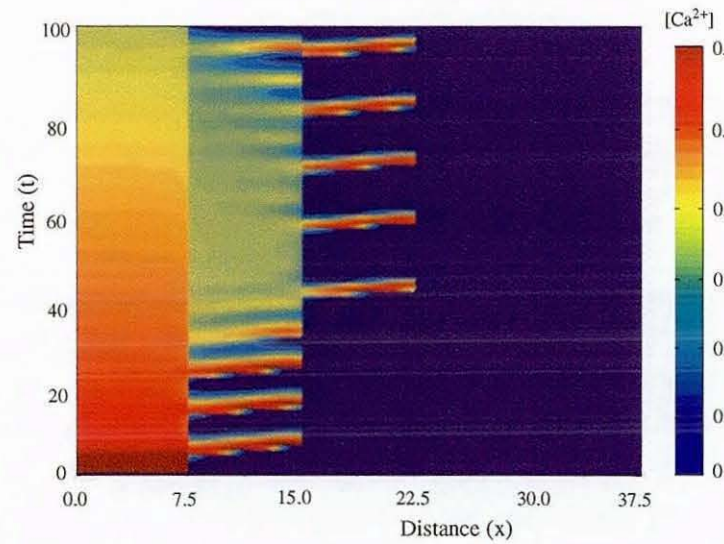


Figure 7.13: *Space-time plot of the calcium concentration in the DYK model of inter-cellular waves for the parameters in Figure 7.11 and $F_p = 2$.*

F_p . Similar to the DYK model, we illustrate two space-time plots of the calcium concentration for different values of gap-junctional IP_3 permeability. The left most cell was stimulated by IP_3 and the first five cells are shown. Figure 7.15 demonstrates the propagation of intercellular periodic travelling waves via the whole system with the observed increase in a gap-junctional delay times farther away from the stimulated cell. This is caused by the process of IP_3 diffusion through gap junctions. Figure 7.16 shows a case of decreased IP_3 permeability and as the result of this the failure of intercellular wave propagation.

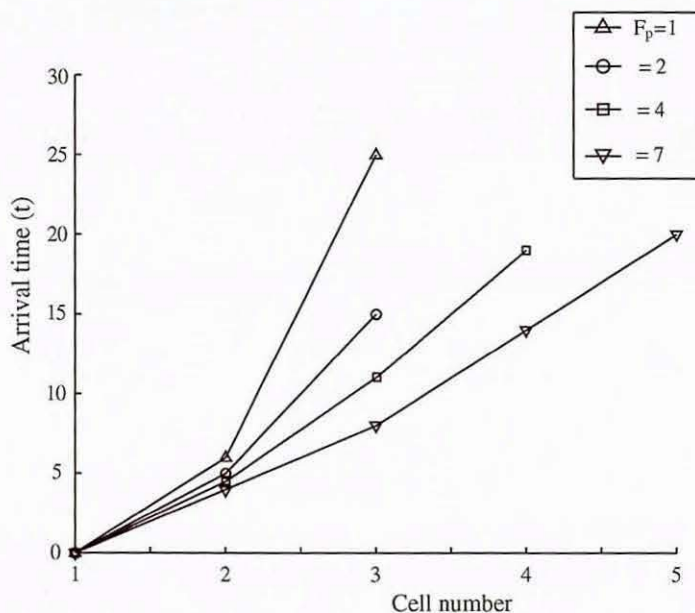


Figure 7.14: *Arrival time of wave in the FDF model for four different values of F_p for the following parameters $\sigma = 1$, $\tau_d = 1$, $L = 7.5$, $D_c = 1$, $F_c = 0.2$, $D_p = 15$, $V_p = 0.01$, $k_\mu = 5$ and $k = 0.1$.*

Summary

In this chapter we have investigated the subject of wave propagation failure through the cell tissue in two different models of Ca^{2+} release, DYK and FDF. In the first part of the analysis (analytical and numerical) the level of IP_3 concentration is assumed to

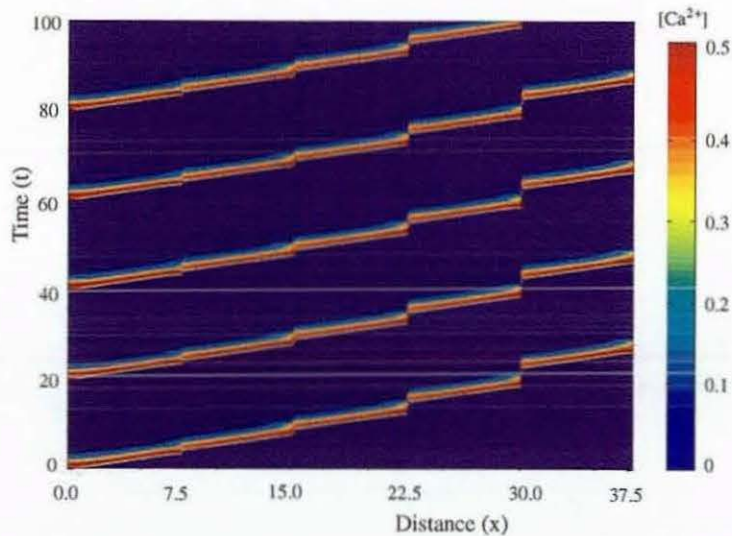


Figure 7.15: Space-time plot of the calcium concentration in the FDF model of inter-cellular waves for the parameters in Figure 7.14 and $F_p = 7$.

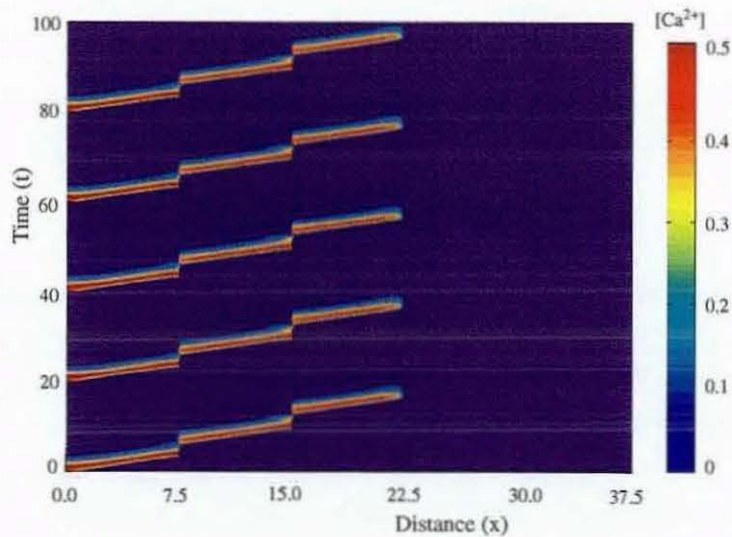


Figure 7.16: Space-time plot of the calcium concentration in the FDF model of inter-cellular waves for the parameters in Figure 7.14 and $F_p = 2$.

be constant throughout the cell culture and the intercellular Ca^{2+} wave is mediated by a passive Ca^{2+} diffusion through gap junctions. Numerical simulation of the DYK model shows that the critical gap-junctional calcium permeability is consistent with that found from the mathematical analysis of the FDF model. In the second part, we have included the dynamics of IP_3 into these two models assuming a passive diffusion of IP_3 from the stimulated cell as well as Ca^{2+} propagation through the gap junction. A qualitative comparison of the simulation results of both the DYK and FDF models in respect of wave propagation dependence on gap-junctional permeability shows the similarity in behaviour of a propagating intercellular wave through the cell tissue.

Conclusions and further work

In this chapter we describe some natural ways to extend the work presented in this thesis. First, however, we briefly summarise the main achievements of this thesis

8.1 Conclusions

In this thesis we have studied oscillations and waves of cytosolic Ca^{2+} in single cells as well as multi-cellular systems from a mathematical perspective. We have focused on two models of Ca^{2+} release (DYK and FDF) for a systematic analytical and numerical analysis of Ca^{2+} dynamics.

First of all, a detailed numerical bifurcation analysis together with a linear stability analysis in the reduced DYK model was presented. The dispersion curve for periodic waves and a kinematic theory of irregular wave propagation were used to predict the existence of a non-periodic travelling wave connecting periodic orbits. This prediction was confirmed by direct numerical simulation. We have used a detailed analysis of the DYK model to motivate the form of a much simpler minimal FDF model capable of exhibiting qualitatively similar behaviour to that of the more complex biophysical

DYK model We have presented the generalised form of the original FDF model supporting both solitary and periodic travelling waves and retaining mathematical tractability. One of the important features of this generalised model is the inclusion of an IP_3 sensitive threshold. The explicit construction of travelling waves has allowed us to probe the mechanisms for propagation failure in the two extremes of i) a continuous distribution of calcium stores and ii) a discrete distribution.

Moreover, we have presented an integrative multi-scale framework which opens up new possibilities for mathematical progress in studying the dynamics of Ca^{2+} release in cells. In particular we have shown that the FDF model may be naturally extended to include further layers of biological reality. The important extensions presented in this thesis include more general choices of the distribution of release sites, the stochastic triggering of release and studying the model in one and two dimensions. The computationally efficient FDF framework is ideal for investigating spark to wave transitions within a spatially extended cell model with a discrete distribution of release sites. Numerical simulations of the model in one and two dimensions (with stores arranged on both regular and disordered lattices) have illustrated the spontaneous production of Ca^{2+} sparks, the spreading of circular Ca^{2+} waves, spirals and more irregular waves. This highlights the ability of the model to describe realistic travelling Ca^{2+} waves. Furthermore, this approach allowed us to examine behaviour which can only be produced in stochastic systems, and in particular AECR. This phenomenon could play a potentially important role in the development of ectopic beats in the heart. For an intracellular Ca^{2+} oscillation to trigger an ectopic beat it is necessary that it first triggers an action potential. This can only be triggered if the sodium-calcium exchange current associated with a Ca^{2+} oscillation is sufficiently large and rapid. However, in experiments on isolated myocytes, Ca^{2+} waves rarely trigger an action potential. If Ca^{2+} release was simultaneous throughout the cell (i.e. if the Ca^{2+} oscillations were due to AECR) rather than in the form of a wave, the induced sodium-calcium exchange current would have a larger amplitude, increasing the likelihood of

an action potential being evoked

In numerical simulations of a one-dimensional stochastic FDF model it has also been possible to identify a critical level of noise defining a non-equilibrium phase-transition between propagating and abortive structures. A statistical analysis shows that this transition is the same as for models in the DP universality class. The analysis of calcium release and transport in the generalised stochastic FDF model may be used for determination of the critical levels of extracellular Ca^{2+} , and values of other controllable variables, necessary for an experiment to exhibit the types of abortive waves that would signal the onset of a DP phase transition. This may provide the first experimental realisation of the critical exponents for the intensely studied DP universality class in statistical physics.

8.2 Further work

We have shown that the biophysically motivated DYK model of calcium release can be viewed as possessing an IP_3 sensitive threshold (Chapter 4). The use of this IP_3 sensitive threshold within the stochastic FDF framework would allow the investigation of the effects of stochastic fluctuations in IP_3 levels. Although not expected to influence any critical exponents (since these should be independent of the details of the model), the background level of IP_3 would be expected to influence the speed and shape of a travelling wave. Interestingly precisely this issue has been recently addressed by Shuai and Jung [147] in a model of Ca^{2+} release which incorporates a stochastic model of an IP_3R .

Throughout this work we have made the assumption that diffusion is isotropic. However, the relaxation of this assumption does not lead to any technical difficulties. For example, in two dimensions we might consider the replacement $D\nabla^2 \rightarrow D_x\partial_{xx} + D_y\partial_{yy}$ so that $G(x, y, t) = \exp[-t/\tau_d] \exp[-x^2/4D_xt - y^2/4D_yt]/4\pi\sqrt{D_xD_yt}$. The remain-

der of the formalism we have employed then carries over. Also as it stands the FDF framework incorporates only a linear model of SERCA pump, although a common model of such a process is to consider a sink of the form $u^n/(K + u^n)$. A piecewise constant version of such a function (valid as $n \rightarrow \infty$) may be easily studied within the FDF framework

The stochastic phase plane analysis used for addressing threshold noise [36] may also be suited for establishing the distribution of release event duration. Once this is determined the discrete time update rule can be replaced by an iterated function system where τ_R is treated as a random variable (with known distribution)

In the FDF framework it will also be possible to explore the importance of *focal sites* on wave initiation and propagation. Focal release sites are distinguished by their higher sensitivity to IP_3 and their close apposition to neighboring release sites. They are known to be able to entrain both the temporal frequency and spatial directionality of calcium waves [107]. This issue has recently been considered by Falcke from a theoretical perspective [51, 52]. Falcke shows that, for a stochastic realisation of the DYK model, large period (noise induced) oscillations may be perceived as a nucleation phenomena where the period of oscillation depends on the geometry of the array of release sites.

The recent experimental progress in determining the precise spatio-temporal recruitment pattern of sparks in rat atrial myocytes [100] provides an ideal testing ground for the use of a stochastic FDF framework to understand the behaviour of real cells. An important aspect of this particular cell that can naturally be accommodated within our FDF framework is the separation of stores into subsarcolemmal junctional SR (JSR) and central nonjunctional SR (NJSR) classes. It is known that Ca^{2+} rise in atrial myocytes occurs at so-called *eager-sites* in the subsarcolemmal region followed by CICR wave propagation into the deeper layers of the cell. It would appear that enhanced excitability of the eager-sites leads to a predetermined microscopic

activation sequence of Ca^{2+} sparks whereby single cells produce reproducible inhomogeneous Ca^{2+} release upon depolarisation. Models of the VOCC channels (that mediate the entry of the electrical signal into the cell) may be developed using an appropriate FDF voltage dependent (rather than Ca^{2+}) threshold function. Since eager-sites display the highest frequency of spontaneous Ca^{2+} sparks in resting cells the functional distinction between JSR and NJSR stores may be modelled using a non-uniform distribution of thresholds. In particular the use of a stochastic FDF model will allow the investigation of how the geometry of release sites gives rise to nucleation phenomena. Furthermore, such a modelling study will be able to probe the way in which the failure to recruit Ca^{2+} sparks appropriately can lead to defective excitation-contraction coupling in cardiac cells [64].

In addition to forming the global Ca^{2+} transient underlying contraction, Ca^{2+} sparks can also cause depolarisation of cardiac cells and thereby enhance or corrupt the rhythm of the heart. Incubation of electrically-paced atrial myocytes causes the appearance of spontaneous subsarcolemmal Ca^{2+} sparks [97], which are probably due to the activation of IP_3Rs that co-localise with RyRs in these cells. The progressive increase in cytoplasmic Ca^{2+} caused by the summation of infrequent subsarcolemmal Ca^{2+} sparks promotes electrogenic forwardmode $\text{Na}^+/\text{Ca}^{2+}$ exchange. Because of the strategic firing of subsarcolemmal Ca^{2+} spark sites, only a few events may be necessary to create enough inward current to drive a cell to the threshold for depolarisation [68]. The ability of a few Ca^{2+} sparks to enhance cardiac automaticity (increase the frequency of spontaneous action potentials) has potentially serious implications for the generation of cardiac arrhythmias and sudden heart failure. The FDF framework may be suited to probing the issue of spontaneous release from the SR from a theoretical perspective. In particular, it is possible to consider the role of the dual presence of both RyRs and IP_3Rs and their spatial distribution in generating delayed after-depolarising (DAD) currents [101]. Moreover, a theoretical study of wave initiation and propagation can be compared to experiments where each receptor class is

pharmacologically knocked out. Using a theoretical approach we may determine the conditions that separate subthreshold DADs (associated with a non-regenerative ring of Ca^{2+} around the cell) from suprathreshold DADs (associated with a ring of sparks that propagates to the deep cell layers).

Finally, the generalised FDF model can be easily extended to a fully three dimensional system. This is especially relevant to the modelling of subsarcolemmal waves in atrial myocytes, where release sites are arranged along one-dimensional lines in a three-dimensional cell. By generalising the one-dimensional analysis and incorporating the appropriate inhomogeneous mixed boundary conditions this problem may be tackled using Fourier techniques along the lines described by Lemon [95].

Appendix A

Numerical Issues

A.1 XPPAUT

The XPPAUT package has been developed by Bard Ermentrout [49] at the University of Pittsburgh and is freely available free at <http://www.pitt.edu/~phase/>. It is an interactive package for numerically solving and analysing differential equations. It also provides a simple interface to most of the common features of the numerical bifurcation software AUTO (<ftp://ftp.cs.concordia.ca/pub/doedel/auto>), originally developed by E J Doedel [46].

We list XPPAUT codes (*ode files) that have been used to produce some of the figures in Chapters 2 and 5.

Program 1. Oscillations in the two-pool model

```
#Parameters
par mu=0.2,gam=2,eps=0.04,bet=0.13,alfa=0.9,del=0.004,n=2,m=2,p=4
#Equations
```

```

u' = mu - u - gam * f(u, v) / eps
v' = f(u, v) / eps
f(u, v) = bet * ((u^n) / (1 + u^n)) - ((v^m) / ((v^m) + 1)) * ((u^p) / (alfa^p + u^p)) - del * v
done

```

Program 2. Oscillations in the full DYK model of IP₃R

```

#Parameters
par p=1
#Equations
dx000/dt = -(v1+v2+v3)
dx100/dt = -(v4+v5-v1)
dx001/dt = -(-v2+v8+v9)
dx010/dt = -(-v3+v11+v12)
dx101/dt = -(-v9-v4+v15)
dx011/dt = -(-v8+v17-v11)
dx110/dt = -(v19-v5-v12)
dc/dt = (r1*(x110)^3+r2)*(caer-c) - (r3*c^2)/((c^2)+(kp^2))
#Functions
x111 = 1 - (x000+x100+x001+x010+x101+x011+x110)
v1 = kp1*p*x000 - km1*x100
v2 = kp4*c*x000 - km4*x001
v3 = kp5*c*x000 - km5*x010
v4 = kp2*c*x100 - km2*x101
v5 = kp5*c*x100 - km5*x110
v8 = kp5*c*x001 - km5*x011
v9 = kp3*p*x001 - km3*x101
v11 = kp4*c*x010 - km4*x011
v12 = kp1*p*x010 - km1*x110

```

```

v15=kp5*c*x101-km5*x111
v17=kp3*p*x011-km3*x111
v19=kp2*c*x110-km2*x111
#Fixed variables
kp1=400,kp2=0.2,kp3=400,kp4=0.2,kp5=20
km1=52,km2=0.21,km3=377.36,km4=0.029,km5=1.65
caer=1,kp=0.1,r1=20,r2=0.004,r3=1 2
done

```

Program 3. Travelling waves in the reduced DYK model

```

#Parameters
par p=0.7,s=2
#Initial conditions
c(0)=0.2944
w(0)=0
y(0)=0.6431
#Fixed variables
k1=400,k2=0.2,k3=400,k4=0.2,k5=20
km1=52,km2=0.21,km3=377.36,km4=0.029,km5=1.65,
kp=0.1,D=1,caer=1, r1=20,r2=0.004,r3=1.2
bigK1=km1/k1
bigK3=km3/k3
bigK5=km5/k5
bigK2=km2/k2
bigK4=km4/k4
#Equations
c'=w
w'=(s*w-(r1*x110^3+r2)*(caer-c)+r3*c^2/(c^2+kp^2))/D

```

```

y'=((hinf(c,p)-y)/tau(c,p))/s
#Functions
alfa(c,p)=(km4*bigK2*bigK1+km2*p*bigK4)*c/(bigK4*bigK2*(p+bigK1))
beta(c,p)=(km2*p+km4*bigK3)/(p+bigK3)
x110=p*c*y/((p+bigK1)*(c+bigK5))
hinf(c,p)=beta(c,p)/(alfa(c,p)+beta(c,p))
tau(c,p)=1/(alfa(c,p)+beta(c,p))
done

```

Program 4. Oscillations in the Atri model

```

#Parameters
par mu=1
#Equations
c'= kflux*mu*h*(b+c*(1-b)/(k1+c)) - gam*c/(kgam+c)
h'=(k2^2/(k2^2+c^2)-h)/tauh
#Fixed variables
b=0.111,gam=2,tauh=2,k1=0.7,k2=0.7,kgam=0.1,kflux=8.1
done

```

Program 5. Numerical simulation for orbit connection in the reduced DYK model

```

#Parameters
par p=0.2622,caer=1,dx=1,nstar=200,I0=35
par del1=30,del2=50,td=1,r1=20,r2=0.004,r3=1.2
#Initial conditions
c[0..200](0)=0.00825
y[0..200](0)=0.97643

```



```

#Equations
dc0/dt=(r1*x110(c0,y0)^3+r2)*(caer-c0)-r3*c0^2/(c0^2+kp^2)+
+D*(c1-c0)/dx^2+I(t)
dc[1..199]/dt=(r1*x110(c[j],y[j])^3+r2)*(caer-c[j])-r3*c[j]^2/(c[j]^2+kp^2)+
+D*(c[j-1]-2*c[j]+c[j+1])/dx^2
dc200/dt=(r1*x110(c200,y200)^3+r2)*(caer-c200)-r3*c200^2/(c200^2+kp^2)+
+D*(c199-c200)/dx^2
dy[0..200]/dt=(hinf(c[j])-y[j])/tau(c[j])
#Functions
alfa(c)=(km4*bigK2*bigK1+km2*p*bigK4)*c/(bigK4*bigK2*(p+bigK1))
betta(c)=(km2*p+km4*bigK3)/(p+bigK3)
x110(c,y)=p*c*y/((p+bigK1)*(c+bigK5))
hinf(c)=betta(c)/(alfa(c)+betta(c))
tau(c)=1/(alfa(c)+betta(c))
bigK1=km1/k1
bigK3=km3/k3
bigK5=km5/k5
bigK2=km2/k2
bigK4=km4/k4
I(t)=sum(0,nstar)of(I0*heav(t-1'*del1)*heav(td-(t-1'*del1)))+
+sum(nstar+1,400)of(I0*heav(t-nstar*del1-(1'-nstar)*del2)*heav(td-
-(t-nstar*del1-(1'-nstar)*del2)))
#Fixed variables
k1=400,k2=0.2,k3=400,km4=0.029,km5=1.65,km1=52,km2=0.21
km3=377.36,k5=20,k4=0.2,kp=0.1,vc=0.185,D=1
@ MAXSTOR=1000000
#dt=0.1
done

```

Program 6. Travelling front in the continuum FDF model

```

# Bistable wave simulation
#Parameters
par d=30,dx=0.2,sigma=5,taur=1,taud=10000000,cth=0.1
#Initial conditions
c[0..100](0)=0
s[0..20](0)=1.0
s[21..100](0)=0
#global 1 c0-cth {s0=1}
global 1 c10-cth {s10=1}
global 1 c20-cth {s20=1}
global 1 c30-cth {s30=1}
global 1 c40-cth {s40=1}
global 1 c50-cth {s50=1}
global 1 c60-cth {s60=1}
global 1 c70-cth {s70=1}
global 1 c80-cth {s80=1}
global 1 c90-cth {s90=1}
global 1 c100-cth {s100=1}
#Equations
dc0/dt = sigma*heav(s0)/2/taur-c0/taud+d*(c1-c0)/dx^2
dc[1..99]/dt = sigma*heav(s[j])/taur-c[j]/taud+d*(c[j-1]-2*c[j]+c[j+1])/dx^2
dc100/dt = sigma*heav(s100)/2/taur-c100/taud+d*(c99-c100)/dx^2
ds[0..100]/dt = -heav(s[j])/taur
#Auxiliary function
aux logc[0..100] = c[j]
#Numerical method characteristics
@ total=2,trans=0,dt=0.0001,xlo=0,xhi=2000,ylo=0,yhi=1

```

```
@ maxstore=1000000,bounds=10000
@ xplot=x,yplot=Ca10
done
```

Program 7. Travelling front in the discrete FDF model

```
# Bistable wave simulation
#Parameters
par d=30,dx=0.2,sigma=5,taur=0.01,taud=100000000,cth=0.1
#Initial conditions
c[0..100](0)=0
s[0](0)=1.0
s[1..100](0)=0
#global 1 c0-cth {s0=1}
global 1 c10-cth {s10=1}
global 1 c20-cth {s20=1}
global 1 c30-cth {s30=1}
global 1 c40-cth {s40=1}
global 1 c50-cth {s50=1}
global 1 c60-cth {s60=1}
global 1 c70-cth {s70=1}
global 1 c80-cth {s80=1}
global 1 c90-cth {s90=1}
global 1 c100-cth {s100=1}
#Equations
dc0/dt = sigma*heav(s0)/2/taur-c0/taud+d*(c1-c0)/dx^2
dc[1..99]/dt = sigma*heav(s[j])/taur-c[j]/taud+d*(c[j-1]-2*c[j]+c[j+1])/dx^2
dc100/dt = sigma*heav(s100)/2/taur-c100/taud+d*(c99-c100)/dx^2
ds[0..100]/dt = -heav(s[j])/taur
```

```

#Auxiliary function
aux logc[0..100] = c[j]
#Numerical method characteristics
@ total=0.5,trans=0,dt=0.0001,xlo=0,xhi=2000,ylo=0,yhi=1
@ maxstore=1000000,bounds=10000
@ xplot=x,yplot=Ca10
done

```

A.2 MATLAB

Many figures and all animations have been performed using the software package MATLAB produced by The MathWorks, Inc ([http //www mathworks com](http://www.mathworks.com)) MATLAB provides an interactive development tool for scientific and engineering problems and more generally for those areas where significant numerical computations have to be generated Program codes and animations are presented on the CD provided

A.3 Fourier spectral methods

Spectral methods are based on the global representations of functions, usually by a trigonometric or polynomial interpolants, whereas in other methods, such as finite elements or finite differences, the underlying expansion involves local interpolants such as piecewise polynomials In practice this means that the accuracy of the spectral method is much higher than others

We have used a Fourier interpolant on a bounded domain for the generation of spectral differentiation matrices. The nodes have been determined by

$$x_k = (k-1)h, \quad h = \frac{2\pi}{N}, \quad k = 1, \dots, N. \quad (\text{A } 1)$$

Since the canonical interval for the method is $[0, 2\pi]$, we have applied a linear trans-

formation $x_k \longleftrightarrow \frac{Lx_k}{2\pi}$ to convert the domain $[0, L]$ where the differential equation is defined to $[0, 2\pi]$. The differentiation processes in the Jacobian \mathcal{M} of Chapter 3 has been represented by a first- and second - order differentiation matrices

$$D_{k,j}^{(1)} = \begin{cases} 0, & k = j \\ \frac{1}{2}(-1)^{k-j} \cot \frac{(k-j)h}{2}, & k \neq j \end{cases} \quad (\text{A } 2)$$

and

$$D_{k,j}^{(2)} = \begin{cases} 0, & k = j \\ -\frac{1}{2}(-1)^{k-j} \csc^2 \frac{(k-j)h}{2}, & k \neq j, \end{cases} \quad (\text{A } 3)$$

$$\cot(z) = \frac{1}{\tan(z)}, \quad \csc(z) = \frac{1}{\sin(z)}$$

A.4 Intercellular waves in the FDF model

The system of equations for b_1 , b_2 and B_1 as a function of m is as follows

$$\begin{cases} p\lambda^m \rho_1^+ b_1 + p\lambda^{-m} \rho_2^+ b_2 + \lambda^{m+1}(\sqrt{\delta}(\nu_1 - 1) - p(\nu_1 + 1))B_1 = -p\alpha \\ \lambda^m(\sqrt{\delta}\rho_1^- + p\rho_1^+)b_1 + \lambda^{-m}(\sqrt{\delta}\rho_2^- + p\rho_2^+)b_2 - p\lambda^{m+1}(\nu_1 + 1)B_1 = -p\alpha \\ (\nu_1 + 1)b_1 + (\nu_2 + 1)b_2 = s - \alpha, \end{cases} \quad (\text{A } 4)$$

where

$$\begin{aligned} \rho_1^+ &= e^{1/\sqrt{\delta}}\nu_1 + e^{-1/\sqrt{\delta}}, & \rho_1^- &= e^{1/\sqrt{\delta}}\nu_1 - e^{-1/\sqrt{\delta}}, \\ \rho_2^+ &= e^{1/\sqrt{\delta}}\nu_2 + e^{-1/\sqrt{\delta}}, & \rho_2^- &= e^{1/\sqrt{\delta}}\nu_2 - e^{-1/\sqrt{\delta}} \end{aligned}$$

The concentration of calcium in the $(m + 1)$ cell satisfies the equation $u_{m+1}(0) = B_1\lambda^{m+1} + \nu_1 B_1\lambda^{m+1}$, where B_1 is obtained from the system of equations (A.4). Thus, $u_{m+1}(0)$ is given by

$$u_{m+1}(0) = p(1 + \nu_1)[2e^{1/\sqrt{\delta}}\lambda^m(\alpha - s)(\nu_2 - \nu_1) + \alpha(1 + \nu_1)(1 - e^{2/\sqrt{\delta}}\nu_2) +$$

$$\alpha\lambda^{2m}(1 + \nu_2)(e^{2/\sqrt{\delta}}\nu_1 - 1)]/\mathcal{D}, \quad (\text{A } 5)$$

where

$$\mathcal{D} = \lambda^{2m}(1 + \nu_2)[\sqrt{\delta}(1 - \nu_1)(e^{1/\sqrt{\delta}}\nu_1 - 1) + 2p\nu_1(e^{1/\sqrt{\delta}} - 1)] + \\ \sqrt{\delta}(1 - \nu_1^2)(1 - e^{1/\sqrt{\delta}}\nu_2) + 2p(1 + \nu_1)(\nu_1 - e^{1/\sqrt{\delta}}\nu_2).$$

Bibliography

- [1] J Amundson and D Clapham Calcium waves. *Current Opinion in Neurobiology*, 3 375–382, 1993
- [2] A Atri, J Amundson, D Clapham, and J Sneyd. A single-pool model for intracellular calcium oscillations and waves in the *Xenopus laevis* oocyte *Biophysical Journal*, 65 1727–1739, 1993
- [3] P Bak, K Chen, and M Paczuski Solitons in the one-dimensional forest fire model *Physical Review Letters*, 86 2475–2477, 2001
- [4] R Balescu *Statistical Dynamics Matters out of Equilibrium*. Imperial College Press, 1997
- [5] H J Balmforth, G R Ierley, and E A Spiegel Chaotic pulse trains *SIAM Journal on Applied Mathematics*, 54 1291–1334, 1994
- [6] M Bar, M Falcke, H Levine, and L S Tsimring Discrete stochastic modeling of calcium channel dynamics *Physical Review Letters*, 84 5664–5667, 2000
- [7] M J Berridge *Cell to Cell Signalling From Experiments to Theoretical Models*, ed A Goldbeter, chapter Cell signalling through cytoplasmic calcium oscillations, pages 449–459 Academic Press, London, 1989

- [8] M J Berridge Calcium oscillations. *Journal of Biological Chemistry*, 265 9583–9586, 1990
- [9] M J Berridge Inositol trisphosphate and calcium signaling *Nature*, 361 315–325, 1993.
- [10] M J Berridge, M D Bootman, and P Lipp Calcium - a life and death signal *Nature*, 395 645–648, 1998
- [11] M J Berridge, M D Bootman, and H Llewelyn Roderick Calcium signalling: dynamics, homeostasis and remodelling *Nature Reviews, Molecular Cell Biology*, 4 517–529, 2003.
- [12] M J Berridge, P H Cobbold, and K S R Cuthbertson Spatial and temporal aspects of cell signalling *Philosophical Transactions, Royal Society, London (Series B)*, 320 325–343, 1988
- [13] M J Berridge and G Dupont. Spatial and temporal signalling by calcium *Current Opinion in Cell Biology*, 6:267–274, 1994
- [14] M J Berridge and A Galione Cytosolic calcium oscillators *FASEB Journal*, 2 3074–3082, 1988
- [15] M J Berridge and R F Irvine Inositol phosphates and cell signalling. *Nature*, 341 197–205, 1989
- [16] M J Berridge, P Lipp, and M D Bootman Calcium signalling *Current Biology*, 9 R157–R159, 1999
- [17] M J Berridge, P Lipp, and M D Bootman The versatility and universality of calcium signalling *Nature Reviews, Molecular Cell Biology*, 1.11–21, 2000
- [18] I Bezprozvanny, J Watras, and B E Ehrlich Bell-shaped calcium-response curves of $\text{Ins}(1,4,5)\text{P}_3$ -and calcium-gated channels from endoplasmic reticulum of cerebellum *Nature (London)*, 351 751–754, 1991.

- [19] S Boitano, E R Dirksen, and M J Sanderson Intercellular propagation of calcium waves mediated by inositol trisphosphate *Science*, 258 292–294, 1992
- [20] M D Bootman and M J Berridge The elemental principles of calcium signaling *Cell*, 83 675–678, 1995
- [21] M D Bootman, M J Berridge, and P Lipp Cooking with calcium the recipes for composing global signals from elementary events *Cell*, 91 367–373, 1997
- [22] M D Bootman, P Lipp, and M J Berridge The organisation and functions of local Ca^{2+} signals *Journal of Cell Science*, 114 2213–2222, 2001
- [23] J A M Borghans, G Dupont, and A Goldbeter Complex intracellular calcium oscillations. A theoretical exploration of possible mechanisms. *Biophysical Chemistry*, 66 25–41, 1997
- [24] W B Busa and R Nuccitelli An elevated free cytosolic Ca^{2+} wave follows fertilization in eggs of the frog *Xenopus laevis* *Journal of Cell Biology*, 100.1325–1329, 1985
- [25] N Callamaras, J S Marchant, X P Sun, and I Parker Activation and coordination of $\text{InsP}(3)$ -mediated elementary Ca^{2+} events during global Ca^{2+} signals in *Xenopus* oocytes *Journal of Physiology*, 509 81–91, 1998
- [26] A Charles Intercellular calcium waves in glia *Glia*, 24 39–49, 1998
- [27] A C Charles, C C G Naus, D Zhu, G M Kidder, E R Dirksen, and M J Sanderson Intercellular signaling via gap junctions in glioma cells *Journal of Cell Biology*, 118 195–201, 1992
- [28] T R Chay Electrical bursting and luminal calcium oscillation in excitable cell models *Biological Cybernetics*, 75 419–431, 1996

- [29] T R Chay Effects of extracellular calcium on electrical bursting and intracellular and luminal calcium oscillations in insulin secreting pancreatic β -cells *Biophysical Journal*, 73 1673–1688, 1997.
- [30] H Cheng, M R Lederer, W J Lederer, and M B Cannell Calcium sparks and $[Ca^{2+}]_i$ waves in cardiac myocytes *American Journal of Physiology*, 270 C148–C159, 1996
- [31] H Cheng, W J Lederer, and M B Cannell Calcium sparks - elementary events underlying excitation-contraction coupling in heart muscle *Science*, 262:740–744, 1993
- [32] G J Christ, A P Moreno, A Melman, and D C Spray Gap junction-mediated intercellular diffusion of Ca^{2+} in cultured human corporal smooth muscle cells *American Journal of Physiology (Cell Physiology)*, 263 C373–C383, 1992.
- [33] P H Cobbold and K S R Cuthbertson Calcium oscillations Phenomena, mechanisms and significance *Seminars in Cell Biology*, 1 311–321, 1990
- [34] S Coombes. The effect of ion pumps on the speed of travelling waves in the fire-diffuse-fire model of Ca^{2+} release *Bulletin of Mathematical Biology*, 63 1–20, 2001
- [35] S Coombes From periodic travelling waves to travelling fronts in the spike-diffuse-spike model of dendritic waves *Mathematical Biosciences*, 170 155–172, 2001.
- [36] S Coombes, R Hinch, and Y Timofeeva Receptors, sparks and waves in a fire-diffuse-fire framework for calcium release *Progress in Biophysics and Molecular Biology*, to appear, 2003
- [37] S Coombes and Y Timofeeva Sparks and waves in a stochastic fire-diffuse-fire model of calcium release *Physical review E*, 68 021915, 2003

- [38] A H Cornell-Bell, S M Finkbeiner, M S Cooper, and S J Smith. Glutamate induces calcium waves in cultured astrocytes: long-range glial signaling. *Science*, 247:470–473, 1990.
- [39] K S R Cuthbertson. *Cell to Cell Signalling: From Experiments to Theoretical Models*, ed. A Goldbeter, chapter Intracellular calcium oscillators, pages 435–447. Academic Press, London, 1989.
- [40] K S R Cuthbertson and P H Cobbold. Phorbol ester and sperm activate mouse oocytes by inducing sustained oscillations in cell Ca^{2+} . *Nature*, 316:541–542, 1985.
- [41] J C Dallon and H G Othmer. A discrete cell model with adaptive signalling for aggregation of Dictyostelium discoideum. *Philosophical Transactions, Royal Society, London (Series B)*, 352:391–417, 1997.
- [42] P D'Andrea and F Vittur. Gap junctions mediate intercellular calcium signalling in cultured articular chondrocytes. *Cell Calcium*, 20:389–397, 1996.
- [43] P D'Andrea and F Vittur. Propagation of intercellular Ca^{2+} waves in mechanically stimulated articular chondrocytes. *FEBS Letters*, 400:58–64, 1997.
- [44] S Ponce Dawson, J Keizer, and J E Pearson. Fire-diffuse-fire model of dynamics of intracellular calcium waves. *Proceedings of the National Academy of Sciences, USA*, 96:6060–6063, 1999.
- [45] D DiFrancesco. Pacemaker mechanisms in cardiac tissue. *Annual Review of Physiology*, 55:455–472, 1993.
- [46] E Doedel. *Software for continuation and bifurcation problems in ordinary differential equations*. California Institute of Technology, 1986.

- [47] M Endo, M Tanaka, and Y Ogawa. Calcium induced release of calcium from the sarcoplasmic reticulum of skinned skeletal muscle fibres *Nature*, 228 34–36, 1970.
- [48] M Endo, M Tanaka, and Y Ogawa. Calcium-induced release of calcium from the sarcoplasmic reticulum of skinned skeletal muscle fibres *Nature*, 228 34–36, 1970.
- [49] G B Ermentrout. *Simulating, Analysing, and Animating Dynamical Systems A Guide to XPPAUT for Researchers and Students* SIAM, Philadelphia, 2002.
- [50] A Fabiato. Calcium-induced release of calcium from the cardiac sarcoplasmic reticulum *American Journal of Physiology*, 245 C1–C14, 1983.
- [51] M Falcke. Buffers and oscillations in intracellular Ca^{2+} dynamics *Biophysical Journal*, 84 28–41, 2003.
- [52] M Falcke. On the role of stochastic channel behavior in intracellular Ca^{2+} dynamics *Biophysical Journal*, 84 42–56, 2003.
- [53] M Falcke, L Tsimring, and H Levine. Stochastic spreading of intracellular Ca^{2+} release. *Physical Review E*, 62 2636–2643, 2000.
- [54] C P Fall, E S Marland, J M Wagner, and J J Tyson. *Computational Cell Biology* Springer-Verlag, 2002.
- [55] C Fewtrell. Ca^{2+} oscillations in non-excitable cells *Annual Review of Physiology*, 55 427–454, 1993.
- [56] R FitzHugh. Impulses and physiological states in models of nerve membrane *Biophysical Journal*, 1 445–466, 1961.
- [57] R A Fontanilla and R Nuccitelli. Characterization of the sperm-induced calcium wave in *Xenopus* eggs using confocal microscopy. *Biophysical Journal*, 75 2079–2087, 1998.

- [58] J Garcia-Ojalvo and L Schimansky-Geier Excitable structures in stochastic bistable media *Journal of Statistical Physics*, 101 473–481, 2000
- [59] C Giaume and L Venance Intercellular calcium signalling and gap junctional communication in astrocytes *Glia*, 24 50–64, 1998
- [60] J C Gilkey, L F Jaffe, E B Ridgway, and G T Reynolds A free calcium wave traverses the activating egg of the medaka, *Oryzias latipes* *Journal of Cell Biology*, 76 448–466, 1978
- [61] P Glendinning and C Sparrow T-point a codimension two heteroclinic bifurcation *Journal of Statistical Physics*, 43 479–488, 1986
- [62] A Goldbeter *Biochemical Oscillations and Cellular Rhythms the Molecular Bases of Periodic and Chaotic Behaviour* Cambridge University Press, 1996
- [63] A Goldbeter, G Dupont, and M J Berridge Minimal model for signal-induced Ca^{2+} oscillations and for their frequency encoding through protein phosphorylation *Proceedings of the National Academy of Sciences, USA*, 87 1461–14651, 1990
- [64] A M Gomez, HH Valdivia, H Cheng, M R Lederer, L F Santana, M B Cannel, S A McCune, R A Altschuld, and W J Lederer Defective excitation-contraction coupling in experimental cardiac hypertrophy and heart failure *Science*, 276 800–806, 1997
- [65] T Haberichter, M Marhl, and R Heinrich. Birhythmicity, trirhythmicity and chaos in bursting calcium oscillations *Biophysical Chemistry*, 90 17–30, 2001
- [66] T Hofer. Model of intercellular calcium oscillations in hepatocytes synchronization of heterogeneous cells *Biophysical Journal*, 77 1244–1256, 1999

- [67] T Hofer, A Politi, and R Heinrich Intercellular Ca^{2+} wave propagation through gap-junctional Ca^{2+} diffusion: a theoretical study *Biophysical Journal*, 80 75–87, 2001
- [68] J Huser, L A Blatter, and S L Lipsius Intracellular Ca^{2+} release contributes to automaticity in cat atrial pacemaker cells. *Journal of Physiology*, 524 415–422, 2000
- [69] H Hempel, L Schimansky-Geier, and J Garcia-Ojalvo Noise-sustained pulsating patterns and global oscillations in subexcitable media *Physical Review Letters*, 82 3713–3716, 1999
- [70] H Hinrichsen. Non-equilibrium critical phenomena and phase transitions into absorbing states *Advances in Physics*, 49 815–958, 2000
- [71] A L Hodgkin and A F Huxley A quantitative description of membrane current and its application to conduction and excitation in nerve *Journal of Physiology*, 117 500–544, 1952
- [72] R W Holl, M O Thorner, G L Mandell, J A Sullivan, Y N Sinha, and D A Leong Spontaneous oscillations of intracellular calcium and growth hormone secretion *Journal of Biological Chemistry*, 263 9682–9685, 1988
- [73] B Hu and C Zhou Phase sunchronization in coupled nonidentical excitable systems and array-enhanced coherence resonance *Physical Review E*, 61 R1001–R1004, 2000
- [74] M Ino Dynamic regulation of intracellular calcium signals through calcium release channels *Molecular and Cellular Biochemistry*, 190 185–190, 1999
- [75] L T Izu, W G Wier, and C W Balke Evolution of cardiac waves from stochastic calcium sparks *Biophysical Journal*, 80 103–120, 2001

- [76] R Jacob Calcium oscillations in electrically non-excitable cells *Biochimica & Biophysica Acta*, 1052 427–438, 1990
- [77] L F Jaffe. Sources of calcium in egg activation A review and hypothesis *Developmental Biology*, 99 265–276, 1983
- [78] L F Jaffe The path of calcium in cytosolic calcium oscillations A unifying hypothesis. *Proceedings of the National Academy of Sciences, USA*, 88 9883–9887, 1991
- [79] L F Jaffe Classes and mechanisms of calcium waves *Cell Calcium*, 14 736–745, 1993.
- [80] M S Jafri and J Keizer On the roles of Ca^{2+} diffusion, Ca^{2+} buffers and the endoplasmic reticulum in IP_3 -induced Ca^{2+} waves. *Biophysical Journal*, 69 2139–2153, 1995
- [81] I Jensen Low-density series expansions for directed percolation: I A new efficient algorithm with applications to the square lattice *Journal of Physics A*, 32 5233–5249, 1999
- [82] K T Jones Ca^{2+} oscillations in the activation of the egg and development of the embryo in mammals *The International Journal of Developmental Biology*, 42 1–10, 1998
- [83] P Jung and G Mayer-Kress Noise controlled spiral growth in excitable media *Chaos*, 8 458–462, 1995.
- [84] P Jung and G Mayer-Kress Spatiotemporal stochastic resonance in excitable media *Physical Review Letters*, 74 2130–2133, 1995
- [85] J Keener and J Sneyd *Mathematical Physiology* Springer-Verlag, 1998
- [86] J Keizer and G W De Young Simplification of a realistic model of IP_3 -induced Ca^{2+} oscillations *Journal of Theoretical Biology*, 166 431–442, 1994

- [87] J E Keizer and G D Smith Spark-to-wave transition saltatory transmission of calcium waves in cardiac myocytes *Biophysical Chemistry*, 72 87–100, 1998
- [88] J E Keizer, G D Smith, S Ponce Dawson, and J Pearson Saltatory propagation of Ca^{2+} waves by Ca^{2+} sparks *Biophysical Journal*, 75 595–600, 1998
- [89] K Kuba and S Takeshita Simulation of intracellular Ca^{2+} oscillations in a sympathetic neurone *Journal of Theoretical Biology*, 93 1009–1031, 1981
- [90] U Kummer, L F Olsen, C J Dixon, A K Green, E Bornberg-Bauer, and G Baier. Switching from simple to complex oscillations in calcium signaling *Biophysical Journal*, 79 1188–1195, 2000
- [91] R Kupferman, P P Mitra, P C Hohenberg, and S S-H Wang Analytical calculation of intracellular calcium wave characteristics *Biophysical Journal*, 72 2430–2444, 1997
- [92] J Lechleiter and D Clapham Molecular mechanisms of intracellular calcium excitability in *X. laevis* oocytes *Cell*, 69 283–294, 1992
- [93] J Lechleiter, S Girard, D Clapham, and E Peralta. Subcellular patterns of calcium release determined by G protein-specific residues of muscarinic receptors *Nature*, 350 505–508, 1991
- [94] J Lechleiter, S Girard, E Peralta, and D Clapham Spiral calcium wave propagation and annihilation in *Xenopus laevis* oocytes *Science*, 252:123–126, 1991
- [95] G Lemon Fire-diffuse-fire calcium waves in confined intracellular spaces *Bulletin of Mathematical Biology*, to appear, 2003
- [96] Y-X Li and J Rinzel Equations for InsP_3 receptor-mediated $[\text{Ca}^{2+}]$ oscillations derived from a detailed kinetic model a Hodgkin-Huxley like formalism. *Journal of Theoretical Biology*, 166 461–473, 1994

- [97] P Lipp, M Laine, K M Burrell, J M Berridge, and M D Bootman Elementary Ca^{2+} signals underly cardiac arrhythmia caused by endothelin. *Pflugers Archiv European Journal of Physiology*, 437 R151, 1999
- [98] P Lipp and E Niggli Microscopic spiral waves reveal positive feedback in sub-cellular calcium signaling *Biophysical Journal*, 65 2272–2276, 1993
- [99] J Lytton, M Westlin, S E Burk, G E Shull, and D H MacLennan Functional comparisons between isoforms of the sarcoplasmic or endoplasmic reticulum family of calcium pumps *Journal of Biological Chemistry*, 267 14483–14489, 1992
- [100] L Mackenzie, M D Bootman, M J Berridge, and P Lipp Predetermined recruitment of calcium release sites underlies excitation-contraction coupling in rat atrial myocytes *Journal of Physiology*, 530 417–429, 2001.
- [101] L Mackenzie, M D Bootman, M Laine, M J Berridge, J Thuring, A Holmes, W Li, and P Lipp The role of inositol 1,4,5-trisphosphate receptors in Ca^{2+} signalling and the generation of arrhythmias in rat atrial myocytes *Journal of Physiology*, 541 395–409, 2002
- [102] D N MacLennan, W J Rice, and N M Green The mechanism of Ca^{2+} transport by sarco(endo)plasmic reticulum Ca^{2+} -ATPases *Journal of Biological Chemistry*, 272 28815–28818, 1997
- [103] K Maginu Geometrical characteristics associated with stability and bifurcations of periodic travelling waves in reaction-diffusion equations *SIAM Journal of Applied Mathematics*, 45 750–774, 1985
- [104] D Mak and J Foskett Effects of divalent cations on single-channel conduction properties of Xenopus IP_3 receptor *American Journal of Physiology*, 275 C179–C188, 1998

- [105] D Mak, S McBride, V Raghuram, Y Yue, S Joseph, and J Foskett Single-channel properties in endoplasmic reticulum membrane of recombinant type 3 inositol trisphosphate receptor. *Journal of General Physiology*, 115 241–255, 2000
- [106] A Malgaroli, R Fesce, and J Meldolesi Spontaneous $[Ca^{2+}]_i$ fluctuations in rat chromaffin cells do not require inositol 1,4,5-trisphosphate elevations but are generated by a caffeine- and ryanodine-sensitive intracellular Ca^{2+} store *Journal of Biological Chemistry*, 265 3005–3008, 1990
- [107] J S Marchant and I Parker Role of elementary Ca^{2+} puffs in generating repetitive Ca^{2+} oscillations *The EMBO Journal*, 20 65–76, 2001
- [108] M Marhl, T Haberichter, M Brumen, and R Heinrich Complex calcium oscillations and the role of mitochondria and cytosolic proteins *Biosystems*, 57.75–86, 2000
- [109] M Marhl, S Schuster, and M Brumen Mitochondria as an important factor in the maintenance of constant amplitudes of cytosolic calcium oscillations *Biophysical Chemistry*, 71 125–132, 1998
- [110] J Marro and R Dickman *Nonequilibrium Phase Transitions in Lattice Models* Cambridge University Press, 1999
- [111] M R McAinsh, A A R Webb, J E Taylor, and A M Hetherington Stimulus-induced oscillations in guard-cell cytosolic free calcium *Plant Cell*, 7 1207–1219, 1995
- [112] T Meyer and L Stryer Calcium spiking *Annual Review of Biophysics and Biophysical Chemistry*, 20 153–174, 1991
- [113] R N Miller and J Rinzel The dependence of impulse propagation speed on firing frequency, dispersion, for the Hodgkin-Huxley model *Biophysical Journal*, 34 227–259, 1981

- [114] H Mogami, A V Tepikin, and O H Petersen Termination of cytosolic Ca^{2+} signals Ca^{2+} reuptake into intracellular stores is regulated by the free Ca^{2+} concentration in the store lumen *The EMBO Journal*, 17 435–442, 1998
- [115] K Morita, K Koketsu, and K Kuba Oscillation of $[\text{Ca}^{2+}]_i$ -linked K^+ conductance in bullfrog sympathetic ganglion cell is sensitive to intracellular anions *Nature*, 283 204–205, 1980
- [116] J Nagumo, S Arimoto, and S Yoshizawa An active pulse transmission line simulation nerve axon *Proceedings IRE*, 50.2061–2070, 1962.
- [117] E Neher and G J Augustine Calcium gradients and buffers in bovine chromaffin cells *Journal of Physiology*, 450 273–301, 1992
- [118] M T Nelson, H Cheng, M Rubart, L F Santana, A D Bonev, H J Knot, and W J Lederer Relaxation of arterial smooth muscle by calcium sparks *Science*, 270 633–640, 1995
- [119] M C Nowycky and M J Pinter Time courses of calcium and calcium-bound buffers following calcium influx in a model cell *Biophysical Journal*, 64 77–91, 1993
- [120] R Nuccitelli, D L Yim, and T Smart The sperm- induced Ca^{2+} wave following fertilization of the *Xenopus* eggs requires the production of $\text{Ins}(1,4,5)\text{P}_3$ *Developmental Biology*, 158 200–212, 1993
- [121] Y V Osipchuk, M Wakui, D I Yule, D V Gallacher, and O H Petersen Cytoplasmic Ca^{2+} oscillations evoked by receptor stimulation, G-protein activation, internal application of inositol trisphosphate or Ca^{2+} Simultaneous microfluorimetry and Ca^{2+} dependent Cl^- current recording in single pancreatic acinar cells *The EMBO Journal*, 9 697–704, 1990

- [122] I Parker, J Choi, and Y Yao Elementary events of InsP_3 -induced Ca^{2+} liberation in *Xenopus* oocytes: hot spots, puffs and blips *Cell calcium*, 20 105–121, 1996.
- [123] I Parker and I Ivorra Inhibition by Ca^{2+} of inositol trisphosphate-mediated Ca^{2+} liberation: a possible mechanism for oscillatory release of Ca^{2+} *Proceedings of the National Academy of Sciences, USA*, 87 260–264, 1990
- [124] I Parker and Y Yao Regenerative release of calcium from functionally discrete subcellular stores by inositol trisphosphate *Proceedings of the Royal Society of London (Series B)*, 246 269–274, 1991
- [125] S Patel, L D Robb-Gaspers, K A Stellato, M Shon, and A P Thomas Coordination of calcium signalling by endothelial-derived nitric oxide in the intact liver *Nature Cell Biology*, 1 467–471, 1999.
- [126] J E Pearson and S Ponce Dawson Crisis on skid row *Physica A*, 257 141–148, 1998
- [127] J E Pearson, S Ponce Dawson, J Keizer, and G Smith Crisis on skid row http://www-xdiv.lanl.gov/XCM/pearson/skid_row_relay.ps, 1998
- [128] O H Petersen and M Wakui Oscillating intracellular Ca^{2+} signals evoked by activation of receptors linked to inositol lipid hydrolysis. Mechanism of generation *Journal of Membrane Biology*, 118 93–105, 1990
- [129] P E Rapp and M J Berridge Oscillations in calcium-cyclic AMP control loops form the basis of pacemaker activity and other high frequency *Journal of Theoretical Biology*, 66 497–525, 1977
- [130] P E Rapp and M J Berridge The control of transepithelial potential oscillations in the salivary gland of *Calliphora erythrocephala* *Journal of Experimental Biology*, 93 119–132, 1981

- [131] T J Rink and R Jacob Calcium oscillations in non-excitabile cells *Trends in Neurosciences*, 12:43–46, 1989
- [132] J Rinzel and K Maginu *Non-equilibrium Dynamics in Chemical Systems*, chapter Kinematic analysis of wave pattern formation in excitable media, pages 107–113 Springer-Verlag, 1984
- [133] L D Robb-Gaspers and A P Thomas Coordination of Ca^{2+} signaling by intercellular propagation of Ca^{2+} waves in the intact liver *Journal of Biological Chemistry*, 270 8102–8107, 1995.
- [134] H Llewelyn Roderick, M J Berridge, and M Bootman *Understanding Calcium Dynamics Experiments and Theory*, eds M Falcke, D Malchow, chapter The endoplasmic reticulum a central player in cell signalling and protein synthesis, pages 17–35 Springer-Verlag, 2003
- [135] M M Romeo and C K R T Jones The stability of traveling calcium pulses in a pancreatic acinar cell *Physica D*, 177 242–258, 2003
- [136] T A Rooney and A P Thomas Intracellular calcium waves generated by $\text{Ins}(1,4,5)\text{P}_3$ -dependent mechanisms *Cell Calcium*, 14 674–690, 1993
- [137] J C Sáez, J A Connor, D C Spray, and M V L Bennett Mechanisms of calcium oscillations and waves a quantitative analysis *Proceedings of the National Academy of Sciences, USA*, 86 2708–2712, 1989
- [138] F Sala and A Hernández-Cruz Calcium diffusion modeling in a spherical neuron relevance of buffering properties. *Biophysical Journal*, 57:313–324, 1990
- [139] M J Sanderson Intercellular calcium waves mediated by inositol trisphosphate *CIBA Foundation Symposium*, 188 175–189, 1995

- [140] M J Sanderson, A C Charles, S Boitano, and E R Dirksen Mechanisms and function of intercellular calcium signaling *Molecular and Cellular Endocrinology*, 98 173–187, 1994
- [141] M J Sanderson, A C Charles, and E R Dirksen. Mechanical stimulation and intercellular communication increases intercellular Ca^{2+} in epithelial cells *Cell Regulation*, 1 585–596, 1990
- [142] I Schulz, E Krause, A Gonz  les, A Gobel, L Sternfeld, and A Schmid Agonist-stimulated pathways of calcium signaling in pancreatic acinar cells *Biological Chemistry*, 380 903–908, 1999.
- [143] S Schuster, M Marhl, and T Hofer Modelling of simple and complex calcium oscillations From single-cell responses to intercellular signalling *European Journal of Biochemistry*, 269 1333–1355, 2002
- [144] P Shen and R Larter Chaos in intracellular Ca^{2+} oscillations in a new model for non-excitable cells *Cell Calcium*, 17 225–232, 1995
- [145] J W Shuai and P Jung Optimal intracellular calcium signalling *Physical Review Letters*, 88 068102, 2002
- [146] J W Shuai and P Jung Stochastic properties of Ca^{2+} release of inositol 1,4,5-trisphosphate receptor clusters *Biophysical Journal*, 83 87–97, 2002
- [147] J W Shuai and P Jung Selection of intracellular calcium patterns in a model with clustered Ca^{2+} release channels *Physical Review E*, 67 031905, 2003
- [148] B M Slepchenko, J C Schaff, and Y S Choi Numerical approach to fast reactions in reaction-diffusion systems application to buffered calcium waves in bistable models. *Journal of Computational Physics*, 162 186–218, 2000

- [149] J Sneyd *An Introduction to Mathematical Modeling in Physiology, Cell Biology, and Immunology*, chapter Calcium excitability, pages 83–118 American Mathematical Society, 2002
- [150] J Sneyd, T R Brian, B Wetton, A C Charles, and M J Sanderson Intercellular calcium waves mediated by diffusion of inositol trisphosphate a two-dimensional model *American Journal of Physiology (Cell Physiology)*, 268 C1537–C1545, 1995
- [151] J Sneyd, A C Charles, and M J Sanderson A model for the propagation of intercellular calcium waves *American Journal of Physiology (Cell Physiology)*, 266 C293–C302, 1994
- [152] J Sneyd, P Dale, and A Duffy Traveling waves in buffered systems applications to calcium waves *SIAM Journal of Applied Mathematics*, 58 1178–1192, 1998
- [153] J Sneyd, J Keizer, and M J Sanderson Mechanisms of calcium oscillations and waves: a quantitative analysis *FASEB Journal*, 9 1463–1472, 1995.
- [154] J Sneyd, A LeBeau, and D Yule Traveling waves of calcium in pancreatic acinar cells model construction and bifurcation analysis *Physica D*, 145 158–179, 2000
- [155] J Sneyd and K Tsaneva-Atanasova *Understanding Calcium Dynamics Experiments and Theory*, eds M Falcke, D Malchow, chapter Modeling calcium waves, pages 179–199. Springer-Verlag, 2003
- [156] J Sneyd, K Tsaneva-Atanasova, J I E Bruce, S Straub, D R Giovannucci, and D I Yule A model of calcium waves in pancreatic and parotid acinar cells *Biophysical Journal*, 85 1–14, 2003
- [157] B Soria and F Martin Cytosolic calcium oscillations and insulin release in pancreatic islets of Langerhans *Diabetes & Metabolism (Paris)*, 24 37–40, 1998

- [158] D Stauffer and A Aharony *Introduction to Percolation Theory* Taylor & Francis, London, 1992.
- [159] X-P Sun, N Callamaras, J Marchant, and I Parker A continuum of InsP_3 -mediated elementary Ca^{2+} signaling events in *Xenopus* oocytes *Journal of Physiology (London)*, 509 67–80, 1998
- [160] T Takamatsu and W G Wier Calcium waves in mammalian heart Quantification of origin, magnitude, waveform, and velocity *FASEB Journal*, 4 1519–1525, 1990
- [161] Y Tang, J L Stephenson, and H G Othmer Simplification and analysis of models of calcium dynamics based on IP_3 -sensitive calcium channel kinetics *Biophysical Journal*, 70 246–263, 1996
- [162] A P Thomas, D C Renard, and T A Rooney Spatial and temporal organization of calcium signalling in hepatocytes *Cell Calcium*, 12 111–126, 1991.
- [163] D Thomas, P Lipp, M Berridge, and M Bootman Hormone-stimulated elementary Ca^{2+} signals are not stereotypic, but reflect activation of different size channel clusters and variable recruitment of channels within a cluster *Journal of Biophysical Chemistry*, 273 27130–27136, 1998.
- [164] Y Timofeeva and S Coombes A stochastic fire-diffuse-fire model of calcium release *FORMA*, 18 53–58, 2003
- [165] Y Timofeeva and S Coombes. Wave bifurcation and propagation failure in a model of Ca^{2+} release. *Journal of Mathematical Biology*, 47 249–269, 2003
- [166] L N Trefethen *Spectral Methods in MATLAB* SIAM, 2000
- [167] R W Tsein and R Y Tsein Calcium channels, stores, and oscillations *Annual Review Cell Biology*, 6 715–760, 1990

- [168] Y Tsunoda Oscillatory Ca^{2+} signalling and its cellular function *New Biologist*, 3 3–17, 1991
- [169] J Wagner and J Keizer Effects of rapid buffers on Ca^{2+} diffusion and Ca^{2+} oscillations *Biophysical Journal*, 67 447–456, 1994
- [170] J A C Weideman and S C Reddy A MATLAB differentiation matrix suite *ACM Transactions on Mathematical Software*, 26 465–519, 2000
- [171] M Wilkins and J Sneyd Intercellular spiral waves of calcium. *Journal of Theoretical Biology*, 191.299–308, 1998
- [172] N M Woods, K S R Cuthbertson, and P H Cobbold Repetitive transient rises in cytoplasmic free calcium in hormone-stimulated hepatocytes *Nature*, 319 600–602, 1986
- [173] N M Woods, K S R Cuthbertson, and P H Cobbold. Agonist-induced oscillations in cytoplasmic free calcium concentration in single rat hepatocytes *Cell Calcium*, 8 79–100, 1987
- [174] Y Yao, J Choi, and I Parker. Quantal puffs of intracellular Ca^{2+} evoked by inositol trisphosphate in *Xenopus* oocytes *Journal of Physiology (London)*, 482 533–553, 1995.
- [175] G W De Young and J Keizer A single pool IP_3 -receptor based model for agonist-stimulated Ca^{2+} oscillations *Proceedings of the National Academy of Sciences, USA*, 89 9895–9899, 1992
- [176] D T Yue Quenching the spark in the heart *Science*, 276 755–, 1997
- [177] D I Yule, E Stuenkel, and J A Williams Intercellular calcium waves in rat-pancreatic acini: Mechanism of transmission *American Journal of Physiology (Cell Physiology)*, 271 C1285–C1294, 1996

-
- [178] C Zhou, J Kurths, and B Hu Array-enhanced coherence resonance nontrivial effects of heterogeneity and spatial independence of noise *Physical Review Letters*, 87.098101, 2001
- [179] B Zimmermann and B Walz The mechanism mediating regenerative intercellular Ca^{2+} waves in the blowfly salivary gland *The EMBO Journal*, 18 3222–3231, 1999.

